Adaptive Image Acquisition with Consideration of Camera Optics

by

Tao Ma

A dissertation submitted to the Graduate Faculty of
Auburn University
in partial fulfillment of the
requirements for the Degree of
Doctor of Philosophy

Auburn, Alabama
May 7, 2012

Keywords: defocus, anti-aliasing, demosaicking, multispectral imaging

Approved by

Stanley J. Reeves, Chair, Professor of Electrical and Computer Engineering
Thomas S. Denney Jr., Professor of Electrical and Computer Engineering
Jitendra K. Tugnait, Professor of Electrical and Computer Engineering
Tin-Yau Tam, Professor of Mathematics and Statistics

Abstract

This dissertation addresses two common problems in image acquisition. We first introduce an adaptive image acquisition methodology by replacing the traditional birefringent filter with slight out-of-focus blur generated by the camera lens. The optimal defocus setting is automatically adapted to the power spectrum of the scene. A criterion to estimate reconstruction errors without the baseband knowledge of the scene is developed in this work. An optimal Wiener filter then recovers the captured scene and yields sharper images with reduced aliasing. The numerical and visual results for gray-scale images show that our method is superior to current acquisition methods.

The extension of the defocusing method to color image acquisition involves an extra demosaicking step. By designing a multichannel Wiener filter on the luminance and chrominance domain, we simplified the reconstruction of this problem. The error criterion defined for color acquisition is also improved on searching the optimal defocusing settings for the input scene. The acquired color filter array (CFA) image with the optimal amount of blur is reconstructed by a joint deblurring and demosaicking method. The simulation results show the defocusing acquisition achieves better image quality with fewer aliasing artifacts than the traditional acquisition method with or without an anti-aliasing filter.

An optimization of the spectral sensitivities of the Bayer CFA pattern is the other area we propose to address. Due to the nature of the optical sensor used in cameras, a CFA pattern is placed over the sensor to distinguish light spectra with different wavelengths. A multichannel Wiener filter is selected to determine the optimal sensitivity function for each color channel. We further optimize the green sensitivities for different noise levels. Simulation results show that the CFA with optimal spectral sensitivity functions delivers images with smaller color difference and better visual quality than the CFA with fixed sensitivities.

Acknowledgments

I would like to thank my advisor Dr. Stanley Reeves for his guidance and encouragement over the years. Dr. Reeves supported me throughout my research with his patience and knowledge while allowing me to work in my own way. This dissertation would not have been possible without him.

Dr. Thomas Denney, Dr. Jitendra Tugnait and Dr. Tin-Yau Tam, who served on my defense committee, provided invaluable comments and suggestions on this research. The mathematical foundation of this research was built on the knowledge of stochastic signal analysis and matrix theory which I acquired from their classes. I also thank Dr. Brian Thurow for serving as the outside reader of my dissertation.

I would like to thank all the staff in the Electrical and Computer Engineering Department for their kindness and help that leave me with a wonderful memory of research experience at Auburn University. I also would like to thank all the previous and present group members, especially Manu, Weidong, Wenting, Wei Zha, Chun, Wei Feng and Bharath. It was a great pleasure to work with all of you.

I thank my wonderful wife, Bo, for her unconditional love and inspiration through all the difficulties in my graduate studies. She always had confidence in me during my Ph.D. research, and served as a great non-technical consultant and reader of this dissertation. I also would like to thank my parents and my sister for their encouragement and support in every step of my life.

Table of Contents

List of Figures

List of Tables

Chapter 1

Introduction

1.1 Statement of the Problem

The emergence of digital cameras has changed the ways we acquire, reproduce, and transmit images. Film is being replaced by optical sensors, such as Charge-Coupled Device (CCD) or Complementary Metal Oxide Semiconductor (CMOS) sensors. Instead of using chemical solutions to develop films, digital cameras apply signal processing methods to transform the electric charges recorded by the optical sensors into images. A typical digital camera pipeline is shown in Fig. 1.1 which includes the traditional optical components used in film cameras, such as a lens, anti-aliasing filter (AA), infrared blocking filter (IR), aperture and focus control unit. The signal processing steps involve preprocessing, white balance, demosaicking, color transform, post-processing and compression steps [1].

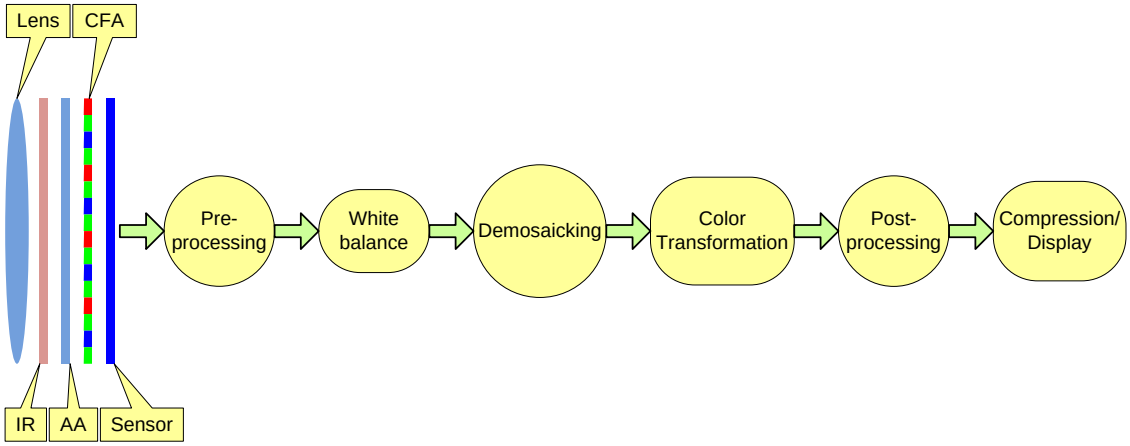

Figure 1.1: The typical processing pipeline of digital cameras.

Because of the complexity of camera design, scientists and engineers often separate these subsystem from each other and optimize their performance individually. Although some design parameters can be fine-tuned after finishing each design and combining them

together, the entire camera pipeline cannot deliver the best image quality this way. It is unquestionable that mutually designing two or more subsystems increases the freedom but involves more difficulty in the process. However, the improvement in the end-to-end performance makes this procedure an attractive design methodology in current research. An introduction on each subsystem of the camera pipeline is provided in this section before we discuss the joint design methodology.

The optical part of digital cameras has a similar structure as film cameras do. Light reflected by the object surfaces passes through the camera lens and aperture which controls the amount of the incoming light. The optical sensor inside the camera records the intensity of light at each spatial location by counting the number of photons and transforming to electrical charges. Since optical sensors respond to infrared light but not the human eye, an IR blocking filter is placed between the aperture and the sensor to block infrared light. An optical AA filter can be found in front of the sensor in mid- to high-level cameras to limit the bandwidth of the scene.

To sense the visible spectrum, digital cameras have to acquire at least three different energies of light with different wavelengths (normally red, green and blue bands). The cameras using three sensors generally offer excellent image quality, but they are much more expensive. Instead of using the three-sensor technique, most consumer cameras use a single sensor chip with a CFA layered over it [1]. Consequently, each sensor cell is only sensitive to the red, green or blue (RGB) channel, and the other two primary colors are missing at each cell. This kind of configuration needs an extra processing step to recover the missing colors in the camera pipeline, which is called demosaicking.

The output of the camera sensor after the analog-to-digital converter becomes a two-dimensional raw image or raw data. In order to transform a raw image to a color image, digital cameras have to perform a series of processes then stores the image in its memory or display the image on its screen. The first step is the preprocessing step. In this step, "hot" pixels, which are defective photosites of the optical sensor, are corrected. Their intensity

value are replaced by an estimated value from their neighboring pixels. Another problem addressed in this step is dark current noise compensation. Dark current is a small current caused by the thermal movement of electrons inside the sensor. A simple technique to compensate the dark current noise is to subtract a mean dark-current image from the raw image according to the exposure time.

White balance is another important step for a digital camera to generate color images which faithfully represent the continuous scenes. Our eyes can easily identify a "white" point from a scene regardless of the illumination. However, digital cameras have no ability to find such a point without a reference. Since different light sources have different spectral responses, the reflected spectra by objects in the scene are different. For example, a piece of white paper appears yellowish under tungsten lighting while the "true" color of the paper shows up under natural sunlight. A solution to deal with the white balance problem is to scale the color channels of a raw image by the ratios of their mean values. This technique is based on the assumption that each color channel in a well balanced image has the same mean. More advanced techniques on automatically performing white balance in camera have been proposed in [2, 3, 4]. However, the photographer must still customize the white balance for scenes under complex lighting conditions.

After the preprocessing and white balance steps, demosaicking aims to reconstruct the full-resolution RGB image from a mosaicked CFA image. Instead of reconstructing the red, green, and blue color channels separately, most demosaicking approaches mutually recover them. Simple demosaicking algorithms linearly interpolate CFA images with the help of edge information extracted from mosaicked data. This kind of technique is more suitable for the real-time process inside cameras because it requires less computation. To further improve the performance of demosaicking, recent algorithms combine traditional techniques with nonlinear techniques which can exploit the inter- and intra-channel correlation more fully than linear techniques. Conversely, a fuller understanding of demosaicking helps to design

more efficient CFA patterns. Designing CFA patterns with various spatial patterns and improved spectral sensitivity functions has also attracted research interest recently [5, 6, 7].

Color transformation projects the full-color image from the RGB color space of a camera to the CIEXYZ color space through a set of matching functions. The camera RGB color space is a device-dependent space. Without a color correction after acquisition, the images obtained by different cameras appear slightly different from each other. The standard CIEXYZ color space matches the way that the human visual system (HVS) perceives color scenes. After the images are transformed to the CIEXYZ space, they can be mapped to the rendered color space for display and storage purpose. The sRGB color space is the most commonly used RGB color space in digital cameras and has become a cross-platform standard for monitors and printers [8]. The number of bits used to represent a single pixel value is reduced from 12 bits to 8 bits during the transformation from CIEXYZ space to rendered sRGB space. This reduction relieves the computational burden in the following post-processing and compression steps.

Post-processing in cameras deals with the artifacts introduced in the previous steps, such as demosaicking. Demoaicking algorithms tend to create zipper effects and false-color errors along the edges. To correct these errors, images can be treated using spatial operations on the chrominance channels after a transform from sRGB space to luminance/chrominance space. Since the HVS is sensitive to the fine structure and edges in the image, a sharpening process also can be found in most cameras. A typical sharpening algorithm calculates the gradient of horizontal and vertical directions of the image. A weighted sum of these two gradients is then added to the original image to improve the sharpness of the image. It is worth noting that any high-frequency errors, such as noise, are amplified by the sharpening process.

Image compression is the last step of a typical camera pipeline before the captured images can be stored in camera memories. Because the main energy of natural images is concentrated in the low-spatial-frequency areas, a lossy compression can discard part of the

high-frequency information of the image without a significant quality drop. Based on the discrete cosine transform (DCT), JPEG is the most popular compression algorithm used in cameras. JPEG compression is performed in the luminance/chrominance space to further improve the efficiency. Images are divided into 8×8 small patches and the algorithm is applied on them to simplify the hardware implementation. JPEG2000 was built on the wavelet transform, which provides the same image quality with a higher compression rate than JPEG standard [9]. Although JPEG2000 is much more complicated than JPEG, camera manufacturers are starting to put this technique into cameras as hardware improves.

1.2 Scope of the Dissertation

From the discussion in the previous section, one can see that the performance of the camera system could be improved if multiple subsystems in the pipeline are designed jointly. A number of research efforts have taken this approach in the past few years. Zhang *et al.* proposed a joint demosaicking-denoising scheme via a linear minimum mean square-error estimation [10]. The optical side of camera design can also be improved by incorporating the image processing techniques used in the pipeline. Robinson and Stork presented a design methodology for the camera lens by optimizing with a Wiener filter the final output image of the camera rather than the optical image of the lens [11]. Similar design techniques were introduced for CFA pattern design to improve the demosaicking results in the reconstruction step [5, 12, 13, 14, 15]. We follow the joint design concept in this dissertation and advance the capability of the camera system.

The primary contribution of this dissertation is the introduction of image reconstruction techniques to help the acquisition of the camera. The unique sampling process in single-sensor cameras raises the problem of image demosaicking. The distortion caused by the spatial anti-aliasing filter is another concern in the reconstruction step. The designs of anti-aliasing filter and CFA pattern benefits from image demosaicking or deblurring techniques.

The strategies to incorporate the acquisition and reconstruction are discussed in detail in this dissertation.

Chapter 2 provides an overview of the anti-aliasing filter and CFA pattern used in single-sensor cameras. Deblurring and demosaicking are two image processing techniques related to these two optical filters. Two types of blur forms and the Bayer CFA pattern are discussed in detail. Common deblurring and demosaicking algorithms are introduced in this chapter. Some background knowledge on trichromacy and color matching functions assists us to build a foundation on color imaging. A few color spaces are also presented in the last section of Chapter 2.

An adaptive acquisition approach by auto-defocusing for grayscale image is presented in Chapter 3. The commonly used birefringent filter is replaced by the out-of-focus blur generated by the camera lens. We formulated a Wiener filter with consideration of the aliasing component to recover the baseband image. An initial acquisition is required to estimate the power spectra of the baseband image and the aliasing component. An error criterion based on the Wiener filter helps the camera to control the lens and generate the optimal amount of blur. The corresponding Wiener filter then restores the final acquired image and delivers images with fewer aliasing artifacts.

Chapter 4 is an extension of the acquisition method introduced in Chapter 3 to single-sensor cameras. To include the unique demosaicking process of such a camera, a multichannel Wiener filter is designed to evaluate the entire reconstruction error. Since the red, green and blue channels of a color image are highly correlated, a Wiener filter is formulated in the luminance and chrominance domain rather than the RGB domain. This formulation simplifies the design and implementation of the multichannel Wiener filter. A new error criterion for color image acquisition is presented in this chapter to estimate the optimal defocus setting. In the last section of this chapter, a joint demosaicking and deblurring method is introduced to restore the captured CFA image.

An optimization of the spectral sensitivities of the Bayer CFA pattern is presented in Chapter 5. We introduce a multispectral imaging model and formulate a model-based Wiener filter with both spatial and spectral correlations. Inspired by the hardware improvement in digital tunable filters, we optimize the green channel sensitivity for various noise levels after deriving the sensitivity functions for the red and blue channels. Since the CIEXYZ color space represents the human visual system, the reconstructed images are compared with the images acquired by the CIECYZ standard matching functions in the CIELAB color space.

Chapter 6 summarizes the contributions of this dissertation. Conclusions are drawn for each design method. A number of practical issues related to the camera design are discussed. Future work about joint design methodology is also covered in this chapter.

Chapter 2

Background

A number of fundamentals about optical filters and related image processing methods are provided in this chapter. Two types of optical filters in cameras are introduced in the first section. The analysis of these filters lays the foundation for the corresponding image processing problems. Common image deblurring techniques used to compensate the distortion and CFA image demosaicking methods are described after that. Finally, the concept of the spectral sensitivity function of a camera and a number of color spaces are presented in the last section of this chapter.

2.1 Two Optical Filters

Three kinds of optical filters can be found in normal digital cameras. They are an infrared filter, and anti-aliasing filter and a color filter array. The infrared filter blocks infrared light which cannot be perceived by the human visual system but can be detected by optical sensors. Since this spectral filter normally has no effect on the subsequent camera pipeline, only the other two optical sensors are considered in this section. The anti-aliasing filter is located between the lens and the sensor to bandlimit the spatial frequency of the scene, while the color filter array makes it possible to acquire color images with single-sensor cameras.

2.1.1 Anti-aliasing Filter

Continuous scenes must be sampled spatially at each pixel location of an optical sensor when digital cameras acquire images. If the scene contains frequencies higher than the Nyquist baseband of the optical sensor, this sampling produces aliasing artifacts in the

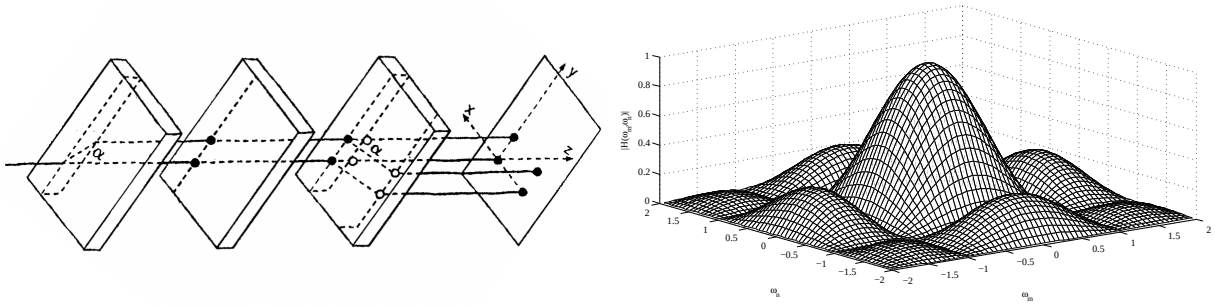

(a) Birefringent filter [17] (b) Frequency response

Figure 2.1: A birefringent filter and its frequency response.

spatial domain during the reconstruction process. Such artifacts are often called Moiré patterns. Most digital cameras apply an optical anti-aliasing filter, which has a lowpass frequency response, on top of the sensor to limit these artifacts.

One commonly used anti-aliasing filter is the four-spot birefringent filter [16]. By carefully designing the thickness of the crystal plate, the input light beam can be separated into four beams and then detected by four neighboring photosites of the sensor. However, the frequency response of this filter is not an ideal lowpass filter but a two-dimensional sinc function. Fig. 2.1.1 shows a typical birefringent filter with its frequency response. The wide transition band and the large sidelobes in the stopband of this filter make it sub-optimal. The distortion in the baseband signal introduces blur, which makes the images less appealing. Although a follow-up image enhancement step can reduce the baseband distortion, it is impossible to remove the existing aliasing artifacts without some information from the original scene. Furthermore, the thickness of the birefringent crystal is fixed by the size of the sensor cells [17], which makes it difficult to design a compact camera.

Much work in optical engineering has been devoted to optimizing the optical transfer function of the birefringent filter [18, 19, 20]. To reduce the design burden in optical design, we consider an alternative acquisition approach without using the birefringent filter. Because of the lowpass characteristics of out-of-focus blur, one can replace the traditional anti-aliasing filter with slight out-of-focus blur generated by the camera lens. A blurred image is captured during the image acquisition with the optimal focus setting found by the camera. A Wiener

filter corresponding to the optimal focus setting then recovers the captured image. Our method seeks to balance the baseband distortion and noise amplification with the error due to aliasing artifacts during the acquisition.

2.1.2 Color Filter Array

The design of a color filter array is based on the way that the HVS perceives colors [21]. Three types of cone cells exist in our retina to sense short, medium, or long wavelength light and discern color (Fig. 2.2(a)). In addition, the HVS has another kind of cell called rods. Rod cells are better for low-light vision but can only sense the intensity of light. Based on the fact that human eyes are more sensitive to the green spectrum, Bayer designed a CFA pattern in 1976 that has become the most commonly used CFA pattern today. In the Bayer CFA, half of the sensor cells measure the green channel and one quarter of the sensor cells measure red and blue channels (Fig. 2.2(b)). Obviously, the Bayer CFA simplifies the human retina mosaic by using a periodic 2×2 pattern rather than a random structure.

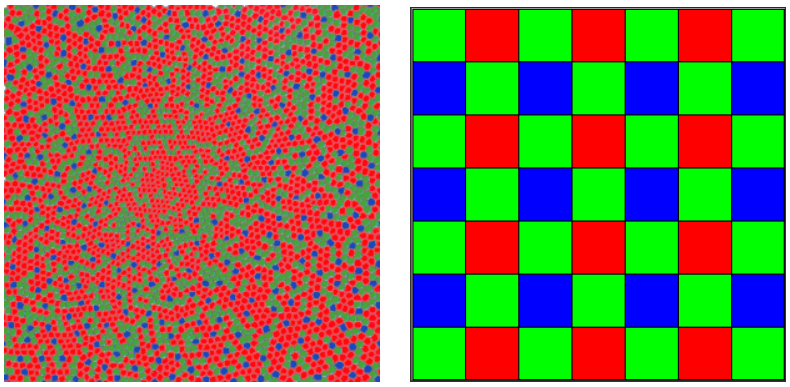

(a) Human eye mosaic pattern (b) Bayer CFA pattern

Figure 2.2: The mosaic patterns in human eyes and the Bayer CFA.

Other types of CFA patters are available for camera design. One group of them is called pure-color CFA patterns. Like the Bayer CFA pattern, pure-color CFA patterns are only constructed with red, green and blue. Their size varies from 2×2 to 8×8. In order to detect more light energy, some patterns include transparent (white) cells that are sensitive

to all colors of light. These patterns are usually called RGBW patterns. RGBW patterns normally provide higher signal-to-noise ratio than ordinary ones, but need special treatment in the following demosaicking steps. Fig. 2.3 (a)–(d) shows four well-studied pure-color CFA patterns, which are Bayer [22], Yamanaka [23] Lukac [24] and Kodak panchromatic [25].

Inspired by the amplitude modulation concept, Hirakawa and Wolfe [6] proposed a spatio-spectral CFA design methodology to reduce the risk of aliasing among color channels. Fig. 2.3 (e)–(h) shows four CFA patterns designed by their method. It should be noted that these patterns are polychromatic. In other word, their spectral sensitivity function have been changed from the traditional RGB spectral frequencies to other frequencies. However, a huge advantage of these patterns is that they simplify the demosaicking problem by changing the most difficult part into a relatively easy hardware problem. The CFA images captured by these patterns can be recovered by a set of simple finite impulse response (FIR) filters which can be easily implemented into digital cameras [26].

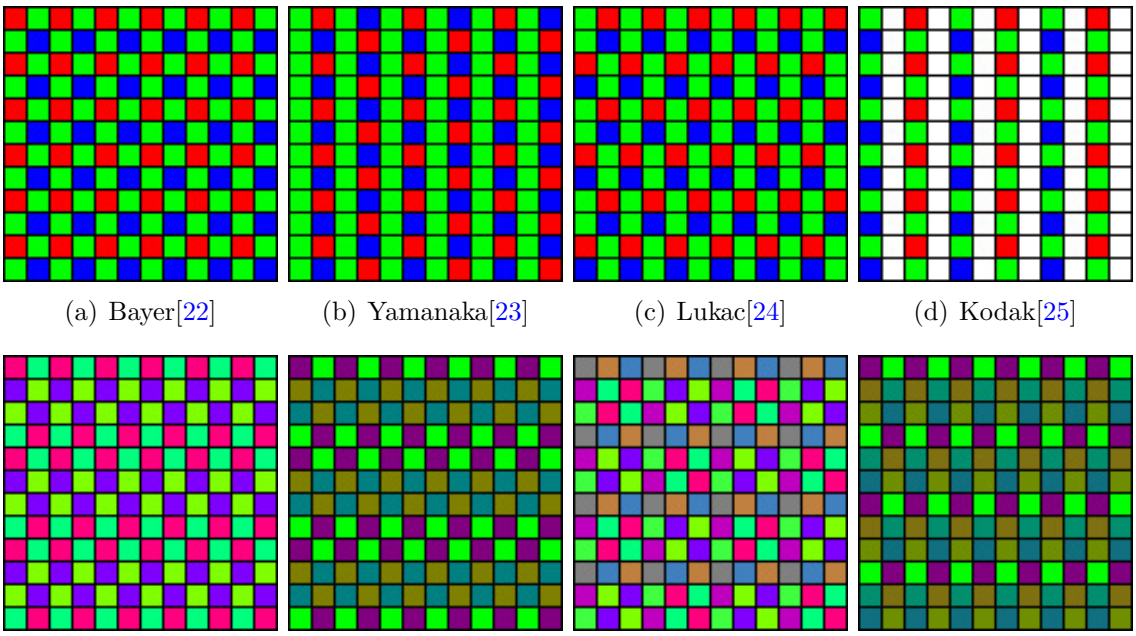

(a) Bayer[22] (b) Yamanaka[23] (c) Lukac[24] (d) Kodak[25]

(e) Pattern A (f) Pattern B (g) Pattern C (h) Pattern D

Figure 2.3: Examples of existing pure-color CFA patterns and new patterns designed by Hirakawa [6].

2.2 Image Deblurring

Two well-known blur forms in digital camera design are out-of-focus blur and the sensor-size effect. Out-of-focus blur is caused by inaccurate lens focus during image acquisition. This type of blur is often called disk blur or circular blur because of its point spread function (PSF), which is given by the following equation:

$$h(x, y; R) = \begin{cases} \frac{1}{\pi R^2}, & \text{if } \sqrt{x^2 + y^2} \leq R, \\ 0, & \text{elsewhere.} \end{cases} \tag{2.1}$$

Another type of blur is introduced by the non-ideal optical sensor since the continuous scene is not sampled by a two-dimensional impulse array. An averaging filter or a Gaussian filter can be used to model the sensor-size effect, such as:

$$h(x, y; \sigma) = \frac{1}{2\pi\sigma^2} e^{-\frac{x^2+y^2}{2\sigma^2}} \tag{2.2}$$

Due to the size difference of sensor cells from camera to camera and the technology used in manufacturing, a more accurate model of this effect has to be determined by an actual test on each specific camera.

Image deblurring algorithms have been well studied since 1960s. Normally, knowledge of the degradation form is required or is estimated by blur identification techniques [27, 28, 29, 30, 31, 32]. A commonly used image formation model for this problem is given by

$$y = Hf + u \tag{2.3}$$

where the vector y is the blurred image and matrix H is the PSF of the blur. The vectors f and u are the original image and the additive noise. The appearance of noise in the image formation equation makes the deblurring an ill-posed problem. A simple inverse filter tends

to amplify the noise at the frequency locations where the response of the blur is small. Wiener filtering or regularized inverse filtering generally are more effective with low complexity.

Recently, restoration methods using multiple image processing techniques have been proposed to provide results that are superior to traditional methods. Katkovnik *et al.* presented a novel nonparametric regression method by applying a local polynomial approximation of the image and the paradigm of intersection confidence intervals [33]. Chen *et al.* proposed a two-step algorithm which restores the degraded image with a simple Wiener filter followed by a modified bilateral filter [34, 35]. Joint deblurring and demosaicking CFA images has also attracted some research interest. Menon and Calvagno designed a regularization approach to adaptively recover the full-color image from the blurred CFA image [36]. Two basic deblurring techniques are discussed in the two following sections.

2.2.1 Frequency-Domain methods

The image formation model defined in Eq. (2.3) indicates that matrix H is a circulant matrix with circulant blocks. The frequency-domain methods takes the advantage that a Fourier transform diagonalize such matrices which reduces the computational cost dramatically. A general restoration algorithm can be described as

$$\hat{F}(\omega_m, \omega_n) = \frac{H^*(\omega_m, \omega_n)}{|H(\omega_m, \omega_n)|^2 + \lambda |L(\omega_m, \omega_n)|^2} Y(\omega_m, \omega_n) \tag{2.4}$$

where $H(\omega_m, \omega_n)$ is the frequency response of the blur. The terms $\hat{F}(\omega_m, \omega_n)$ and $Y(\omega_m, \omega_n)$ represent the discrete Fourier transform (DFT) coefficients of the reconstructed and observed images. The term $L(\omega_m, \omega_n)$ normally is a highpass filter to encourage a smooth solution while λ controls the degree of smoothness.

Wiener filtering is a special case of Eq. (2.4) where the term $\lambda |L(\omega_m, \omega_n)|^2$ is replaced by the ratio of noise spectrum $S_u(\omega_m, \omega_n)$ to the power spectrum of the original image

$S_f(\omega_m, \omega_n)$, such as

$$W(\omega_m, \omega_n) = \frac{H^*(\omega_m, \omega_n)}{|H(\omega_m, \omega_n)|^2 + \frac{S_u(\omega_m, \omega_n)}{S_f(\omega_m, \omega_n)}}. \tag{2.5}$$

Since white Gaussian noise normally is assumed in this problem, the noise spectrum is a constant. Modeling the power spectrum $S_f(\omega_m, \omega_n)$ from the degraded image becomes a critical step for Wiener filtering.

2.2.2 Iterative Methods

Iterative methods update the restored image according to the solution of previous steps. A general algorithm is given by:

$$\hat{f}_{k+1} = \hat{f}_k + \alpha_k r_k, \tag{2.6}$$

where $\hat{f}_{k+1}$ and $\hat{f}_k$ are the restored results at $k+1$ and k steps. The solution is refined by the correction vector r_k and speed of convergence is controlled by the scalar α_k. The implementations of iterative methods can be chosen from many optimization algorithms, such as the steepest descent or the conjugate gradient methods. A joint deblurring and demosaicking method using the steepest descent algorithm is introduced in Chapter 4.

While iterative methods generally provide superior image quality than other methods, the computational cost is a major drawback. The real-time processing inside the camera cannot afford the time and power demands of iterative methods. As a result, these methods are more useful as off-camera techniques. In fact, a single- or multi-step sharpening process can be found in cameras to enhance the output image. Since image enhancement is beyond the scope of this dissertation, sharpening is not described here.

2.3 Color Filter Array Demosaicking

The CFA samples a natural scene during the image acquisition procedure, which yields an infinite periodic spectrum in the frequency domain. Since natural images generally are not bandlimited, it is impossible to reconstruct the original image from the CFA data perfectly.

The demosaicking process takes the CFA image as an input and recovers the full-color image as shown in Fig. 2.3. An intuitive solution of the problem is to interpolate each color channel independently with traditional image processing techniques. However, this approach is sub-optimal since the inter-channel dependencies have been completely ignored. Advanced demosaicking algorithms normally utilize the information gained from other channels to assist the current channel interpolation.

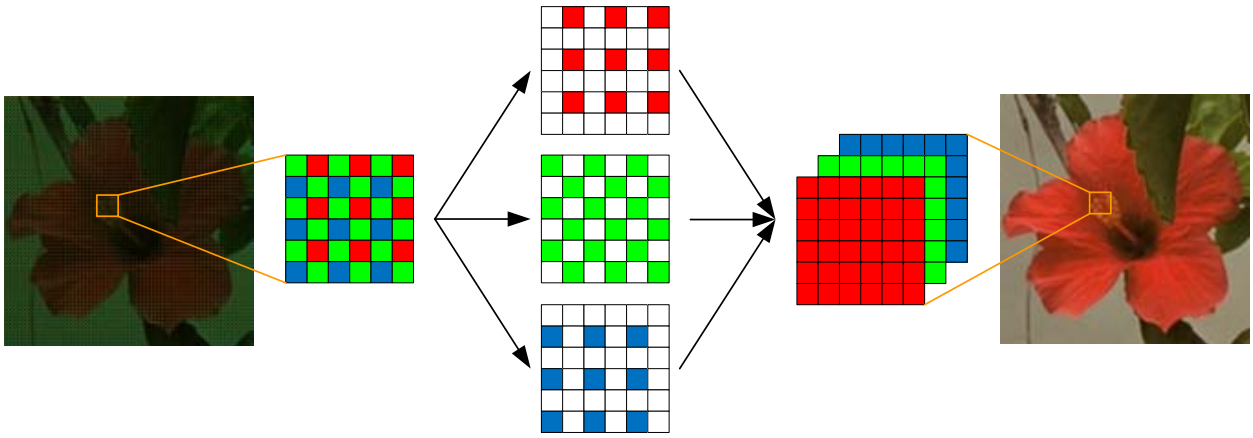

Figure 2.4: The process of color image demosaicking.

2.3.1 Spatial-Domain Demosaicking

The first group of demosaicking algorithms is the spatial-domain method. Most spatial-domain demosaicking approaches sequentially process the CFA image. This strategy first interpolates the green channel, then recovers red/blue channels subsequently using the information from the reconstructed green channel. The reason for this strategy is that the sampling rate of the green channel is two times higher than the red/blue channels. Consequently, the green channel normally contains more high-frequency information than the other two. The overall performance of sequential approaches is mostly dependent on the first step due to the error propagation from the first step to the second step [37]. As a result, a large amount of research effort has concentrated on how to enhance the quality of the green channel.

Figure 2.5: A 7×7 window of Bayer CFA.

Like the gray-scale image interpolation case, edge-directed estimation is the most commonly used technique in the demosaicking process. The interpolation direction is usually determined by the first-order or second-order derivatives. The calculation of derivatives can be performed in either a subsampled channel or the CFA image. Referring to Fig. 2.5, let $\Delta H = |G_{33} + G_{35}|$ and $\Delta V = |G_{24} - G_{44}|$, then a simple edge-directed estimation for the missing green sample G_{34} is:

$$G_{34} = \begin{cases} (G_{33} + G_{35})/2, & \text{if } \Delta H < \Delta V \\ (G_{24} + G_{44})/2, & \text{if } \Delta H > \Delta V \\ (G_{24} + G_{44} + G_{33} + G_{35})/4, & \text{otherwise} \end{cases} \tag{2.7}$$

Rather than using only two interpolation directions (horizontal or vertical), some methods use four directions [38] or even twelve directions [39] to acquire a more accurate estimate of the green channel. The Primary-Consistent-Soft-Decision (PCSD) framework [40] proposed by Wu and Zhang combines the directional estimates by testing interpolation hypotheses via an optimal statistical technique. Instead of selecting two sets of estimates, they achieved better results by fusing two directional Linear Minimum Mean Square-Error Estimation (LMMSE) estimates [41].

To recover the red and blue channels, a number of demosaicking algorithms assume that the ratio of green and red/blue is a constant in a local region of the CFA image. The first demosaicking algorithm built on this assumption was proposed by Cok in 1987 [42]. In this method, the missing red/blue pixels are calculated using four available neighboring red/blue pixels. For example, assuming all green samples have been recovered in Fig. 2.5, the red pixel R_{43} and the blue pixel B_{34} can be estimated as follows:

$$\begin{aligned} R_{43} &= G_{43} \times \frac{1}{4}\left(\frac{R_{32}}{G_{32}} + \frac{R_{34}}{G_{34}} + \frac{R_{52}}{G_{52}} + \frac{R_{54}}{G_{54}}\right) \\ B_{34} &= G_{34} \times \frac{1}{4}\left(\frac{B_{23}}{G_{23}} + \frac{R_{25}}{G_{25}} + \frac{R_{43}}{G_{43}} + \frac{R_{45}}{G_{45}}\right) \end{aligned} \tag{2.8}$$

In [38], Kimmel further improved Cok's method by using a weighted sum to estimate both the missing green and red/blue samples.

Another set of demosaicking methods estimates the color differences between the green channel and the red/blue channel. In the algorithm developed by Laroche and Prescott, the missing red/blue value is the sum of the color differences and the corresponding green pixel [43]. Referring to Fig. 2.5, the red pixels R_{33}, R_{42} and R_{43} are reconstructed by:

$$\begin{aligned} R_{33} =& \frac{1}{2} \times [(R_{32} - G_{32}) + (R_{34} - G_{34})] + G_{33} \\ R_{42} =& \frac{1}{2} \times [(R_{32} - G_{32}) + (R_{52} - G_{52})] + G_{42} \\ R_{43} =& \frac{1}{4} \times [(R_{32} - G_{32}) + (R_{34} - G_{34}) + (R_{52} - G_{52}) + (R_{54} - G_{54})] + G_{43} \end{aligned} \tag{2.9}$$

An improved method can be found in [44], where the second derivatives of green samples are used to estimate the red/blue channel. In [45], the variances of the color differences of a number of directions are taken into account to remove artifacts from green samples. Su optimized the color differences interpolation using a low-complexity iterative algorithm [46].

Novel demosaicking methods normally integrate the first three techniques with other signal processing or statistical tools. In [47], Buades *et al.* designed a demosaicking algorithm with an image denoising tool called non-local means filtering [48]. Hirakawa and Parks

applied the local homogeneity as an indicator other than edge information to select final values from horizontally and vertically interpolated estimates [49]. Gunturk *et al.* formulated an alternating-projections scheme based on the assumption that edges occur simultaneously in different color channels [50]. Ferradans *et al.* estimated image edges with a level-set-based geometric method [51]. Mairal *et al.* presented an image restoration algorithm by assuming that natural images have a sparse decomposition over a redundant dictionary in [52].

2.3.2 Frequency-Domain Techniques

Traditional digital signal processing (DSP) tools, such as FIR filters or wavelets, can be extended to the image demosaicking problem. Fig. 2.6 shows a typical spectrum of a CFA image sampled by the Bayer pattern. It is composed of one luminance component (L) and two chrominance components (C_1 and C_2). Because of the sampling pattern of the Bayer CFA, C_1 is modulated to the location (π, π) while C_2 is modulated to $(0, \pi)$ and $(\pi, 0)$. After obtaining the luminance and chrominance components, one can recover the desired full-color image by a simple linear transformation.

Frequency-domain demosaicking methods normally suffer from false color artifacts or zipper effect due to the spectrum overlaps among L, C_1 and C_2 components. Glotzbach *et al.* made the first effort to cancel such overlaps by combining the results from different type of filters [53]. Alleysson *et al.* proposed a linear frequency-domain techniques where the luminance component was recovered by a 5×5 lowpass filter [54]. In their later work [55], a well-designed 11×11 filter replaced the previous one, and the frequency response of this filter is shown in Fig. 2.7(a).

Another adaptive frequency-domain method was presented by Lian *et al.* [56]. The luminance component at available green pixels is first reconstructed by a simple 5×5 lowpass filter (shown in Fig. 2.7(b)), then refined iteratively. An adaptive filter is also used in each iteration to compensate the loss of high-frequency signals caused by the initial bilinear interpolation. For example, referring Fig. 2.5, a 3×3 filter to estimate the luminance at R_{34}

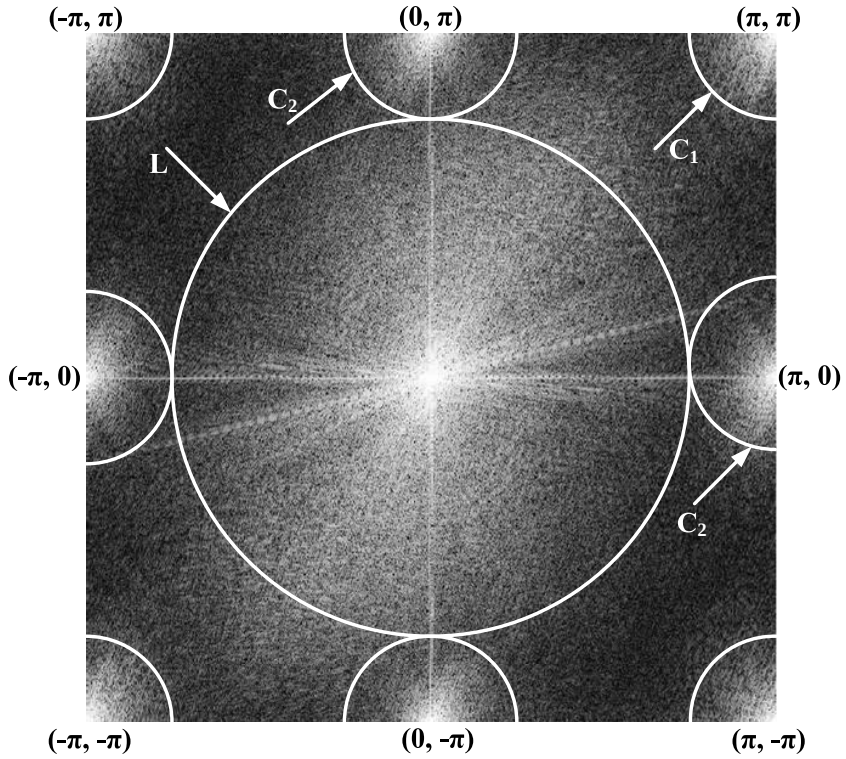

Figure 2.6: Spatial-frequency representation of a CFA image captured by the Bayer pattern.

is defined as follows:

$$\begin{bmatrix} 0 & w_1 & 0 \\ w_4 & 0 & w_2 \\ 0 & w_3 & 0 \end{bmatrix} \tag{2.10}$$

where the filter coefficients w_i are constructed using the following equations between red channel and luminance channel:

$$\begin{aligned} \frac{1}{w_1} &= 1 + |R_{34} - R_{36}| + |L_{35} - L_{33}| \\ \frac{1}{w_2} &= 1 + |R_{34} - R_{14}| + |L_{44} - L_{24}| \\ \frac{1}{w_3} &= 1 + |R_{34} - R_{32}| + |L_{35} - L_{33}| \\ \frac{1}{w_4} &= 1 + |R_{34} - R_{54}| + |L_{44} - L_{24}| \end{aligned} \tag{2.11}$$

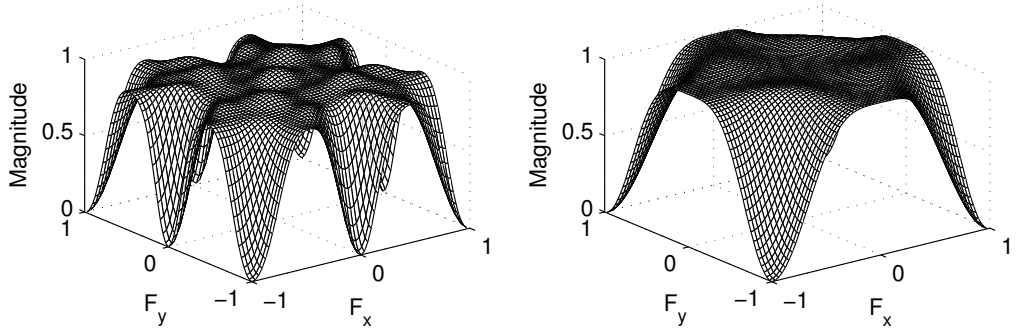

(a) Alleysson's filter[55] (b) Lian's filter[56]

Figure 2.7: The frequency responses of the lowpass filters designed by Alleysson and Lian.

The estimated full-resolution luminance is then applied as a reference to interpolate sub-sampled red, green and blue images.

Recently, a method proposed by Dubois [57] focused on compensating the frequency response of linear filters by adaptively filtering the luminance component or chrominance components. In a local range of a CFA image, the high-frequency signal of luminance only overlaps with one of the spectrum copies of chrominance C_2 (either centered at $(\pi, 0)$ or $(0, \pi)$). In his work, C_1 and two sets of C_2 components were estimated by three 21×21 high-pass filters. The luminance component was recovered by subtracting the estimated chrominance components from the CFA image. The order of the filters was further reduced to 11×11 using a least-squares design and achieved comparable results [58].

2.4 Color Fundamentals

Color is a perception of the human eye. We sense the light spectrum reflected by an object, process this information with our neural system and finally form the color sensation. Based on this fact, color is related to the light spectrum of the radiation and the reflectance of the object. There are two types of photoreceptors in the human eye—rod cells and cone cells. The monochromatic rod cell is mainly responsible for low-light conditions. Cone cells are for color vision and can be categorized into three groups according to their sensitivity

peaks in the spectral-frequency domain. This section introduces the concepts of trichromacy and color matching functions. Perceptually uniform color spaces are also discussed.

2.4.1 Trichromacy and Color Matching Functions

Trichromacy is a scheme to represent colors using three independent color primaries. Grassmann stated that a color can be defined in a three-dimensional linear space [59]. In fact, a color defined by three values (r, g, b) can be computed with linear functions of the form

$$\begin{aligned} r &= \int_0^\infty r_0(\lambda) I(\lambda) d\lambda \\ g &= \int_0^\infty g_0(\lambda) I(\lambda) d\lambda \\ b &= \int_0^\infty b_0(\lambda) I(\lambda) d\lambda \end{aligned} \tag{2.12}$$

where $I(\lambda)$ describes the power distribution of the incident radiation. The functions $r_0(\lambda)$, $g_0(\lambda)$ and $b_0(\lambda)$ are known as color matching functions, and they form a particular color space. Since the visible range of the human eye is between 360 nm and 830 nm, most color spaces are defined in this range by reducing the infinite integrals in Eq. (2.12) to finite ones.

A pure color with the tristimulus values, r_p, g_p and b_p at wavelength λ_p, can be acquired with a line spectrum

$$I(\lambda) = \delta(\lambda - \lambda_p) \tag{2.13}$$

Based on the experimental results of Wright [60] and Guild [61], and the relationships in Eq. (2.12) and (2.13), the Commission Internationale de l'Eclairage (CIE) defined a set of standard color matching functions. Fig. 2.8(a) shows the values of the CIERGB matching functions. These functions show the amounts of primaries, which are the three pure colors at 700 nm, 546.1 nm and 435 nm, required to match the monochromatic test primary. To eliminate the negative values in the CIERGB matching functions, a set of equivalent matching function was defined by CIE. These functions are known as CIEXYZ color matching

functions and are depicted in Fig. 2.8(b). The transform between CIEXYZ and CIERGB is given by

$$\begin{bmatrix} X \\ Y \\ Z \end{bmatrix} = \frac{1}{0.17697} \begin{bmatrix} 0.49 & 0.31 & 0.20 \\ 0.17697 & 0.81240 & 0.01063 \\ 0.00 & 0.01 & 0.99 \end{bmatrix} \begin{bmatrix} R \\ G \\ B \end{bmatrix} \tag{2.14}$$

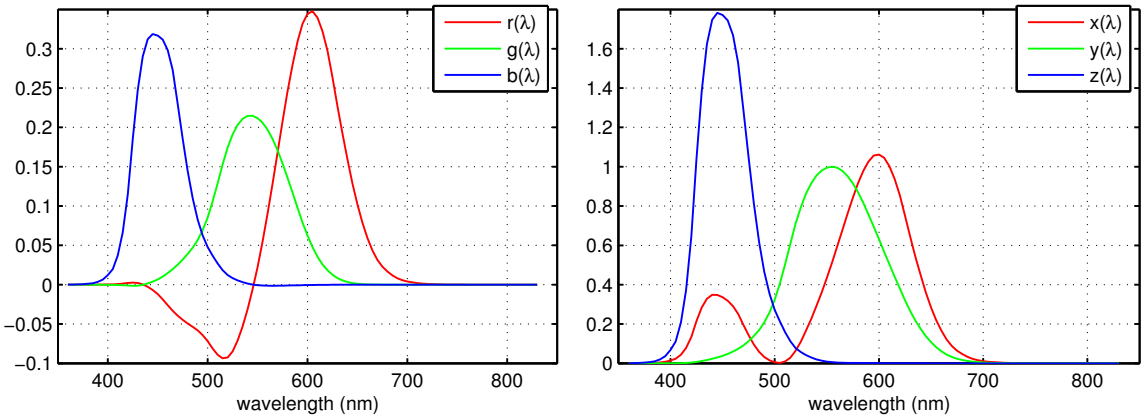

(a) CIERGB color matching functions (b) CIEXYZ color matching functions

Figure 2.8: The two sets of CIE1931 standard color matching functions.

A number of RGB color spaces are defined based on the CIEXYZ color space. The standard RGB (sRGB) color space is the one commonly used in digital cameras [8]. The linear transform from XYZ space to sRGB space is defined by

$$\begin{bmatrix} R_s \\ G_s \\ B_s \end{bmatrix} = \begin{bmatrix} 3.2406 & -1.5372 & -0.4986 \\ -0.9689 & 1.8758 & 0.0415 \\ 0.0557 & -0.2040 & 1.0570 \end{bmatrix} \begin{bmatrix} X \\ Y \\ Z \end{bmatrix} \tag{2.15}$$

Adobe RGB color space is another space which was designed for color printers. Recently, RGB color spaces with wide gamut were developed to improve the color reproduction on displays, such as ProPhoto RGB color space and Adobe Wide Gamut RGB. Since their definitions are beyond the scope of this dissertation, they are not discussed here.

Another important concept in color imaging is the illuminant, since different illuminants change the tristimulus values. The color temperature of the illuminant affects the white balance process of cameras. CIE defined a series of illuminants to simulate the lighting conditions of the real world. The most commonly used one is the D65 illuminant, which corresponds to sunlight under a clear sky. The spectrum distribution of D65 is in Fig. 2.9 and its color temperature is about 6504 K. Other iluminants, such as D50, D55, D75 and incandescent bulbs, are available for various purposes.

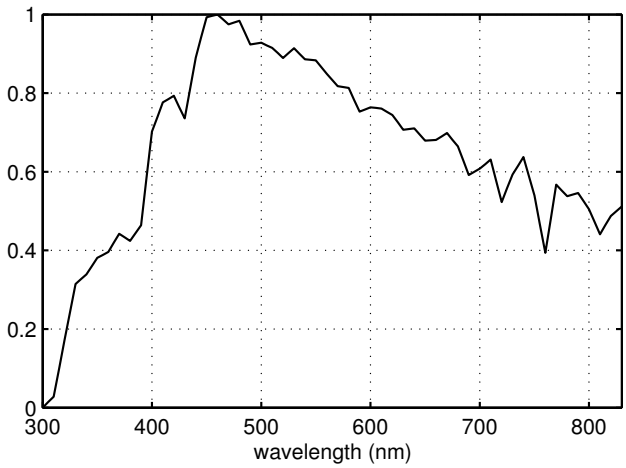

Figure 2.9: The spectrum power distribution of illuminant D65.

2.4.2 Uniform Color Space

A fixed color difference in the CIEXYZ space is not perceptually uniform over the whole space, which makes it impossible to accurately compare two colors in this space. CIE defined two color spaces, CIELUV and CIELAB, to solve this problem. CIELUV space is designed for color television, while CIELAB space is often used in digital cameras. Both spaces are constructed by a nonlinear transform from CIEXYZ color space. The transform from XYZ

to LAB is given by

$$\begin{aligned} L^* &= 116 f(\frac{Y}{Y_n}) - 16 \\ a^* &= 500 \left[f(\frac{X}{X_n}) - f(\frac{Y}{Y_n}) \right] \\ b^* &= 200 \left[f(\frac{Y}{Y_n}) - f(\frac{Z}{Z_n}) \right] \end{aligned} \tag{2.16}$$

where X_n, Y_n and Z_n are the D65 white point point values in the CIEXYZ color space. The function $f(x)$ is defined as follows,

$$f(x) = \begin{cases} 7.787x + \frac{16}{116}, & 0 \leq x \leq 0.008856, \\ x^{\frac{1}{3}}, & 0.008856 \leq x \leq 1. \end{cases} \tag{2.17}$$

The perceptual difference between two colors in CIELAB space can be computed by the Euclidean distance between them.

To incorporate the spatial information in the observed image, the S-CIELAB color space was proposed by Zhang and Wandell as a spatial extension to the CIELAB color space [62]. An input image is first transformed to another domain which is defined by the luminance, red-green and blue-yellow channels. This linear transformation is defined by

$$\begin{bmatrix} O_1 \\ O_2 \\ O_3 \end{bmatrix} = \begin{bmatrix} 0.279 & 0.72 & -0.107 \\ -0.449 & 0.29 & -0.077 \\ 0.086 & -0.59 & 0.501 \end{bmatrix} \begin{bmatrix} X \\ Y \\ Z \end{bmatrix} \tag{2.18}$$

Each color channel is then filtered by a 2D Gaussian kernel whose bandwidth is derived by a series of experiments to simulate the lowpass characteristic of the HVS. The results of this process are transformed to CIELAB space by an inverse transform of Eq. (2.16). Since the spatial response of the HVS is included in S-CIELAB space, the color difference calculated in this space is more perceptually uniform than the one computed in the CIELAB space.

Chapter 3

Grayscale Image Defocusing Acquisition

3.1 Introduction

A digital camera acquires images by spatially sampling continuous scenes at each pixel location of an optical sensor. This sampling produces aliasing artifacts in the spatial domain during the reconstruction process, where Moiré patterns and other artifacts can be observed. Most digital cameras apply an optical anti-aliasing (AA) filter on top of the sensor using a birefringent crystal to limit these artifacts. Such a filter has a lowpass characteristic and reduces the energy of the input scene at frequencies higher than the Nyquist baseband of the optical sensors.

Lyot first introduced the theory of using birefringent crystal plates and polarizers to build spectral optical filters in 1933 [63], but his work is not available anymore. Evans revisited this idea in 1949 [16]. Instead of using birefringent crystals to construct a spectrum filter, Sato et al. invented a spatial-frequency filter using two double refraction plates and a quarter-wave plate [64], as shown in Fig. 3.1. The first refraction plate A horizontally separates the light beam into two beams that are linearly polarized. These two beams are then transformed to circularly polarized beams by the quarter-wave retarder B. The second refraction plate C splits the two beams again vertically into four beams. By carefully designing the thickness of the refraction plates, the four light beams can be detected by four neighboring photosites of the sensor. This commonly used anti-aliasing filter is often called the four-spot birefringent filter.

The thickness of the four-spot filter is determined by the crystal birefringence, the pitch of the sensor, and the angle α between the crystal optical axis and the plate surface normal. Normally, the two refraction plates are cut to make α equal to 45°, which ensures

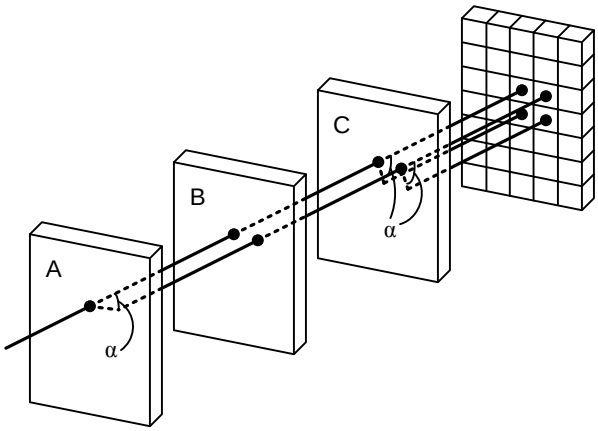

Figure 3.1: A light path of the four-spot birefringent filter.

the maximum separation among four light beams. To reduce the thickness of the four-spot filter, Kessler et al. introduced another design to construct this optical lowpass filter [17].

It is obvious that the point spread function (PSF) of the four-spot filter is a two-dimensional rectangular function with the width the same as the pixel pitch. The frequency response of this filter is not an ideal lowpass filter but a two-dimensional sinc function, as illustrated in Fig. 3.2(a). Although the four-spot filter has the ability to attenuate the high-frequency energy, the wide transition band and the large sidelobes in the stopband of this filter make it sub-optimal. The distortion in the baseband signal results in blurry images and makes them less appealing. Although a follow-up image-enhancement step can reduce the baseband distortion, this step may also enhance aliasing energy in the baseband. It is impossible to remove the existing aliasing artifacts without some information from the original scene.

We consider an alternative acquisition approach without using the birefringent filter in this dissertation, building on preliminary work reported in [65]. Because of the lowpass characteristics of out-of-focus blur, one can replace the traditional anti-aliasing filter with slight out-of-focus blur generated by the camera lens. A blurred image is captured during the image acquisition with the optimal defocus setting found by the camera. A Wiener filter corresponding to the optimal defocus setting then recovers the captured image. In

previous work we have shown that this approach balances the baseband distortion and noise amplification error and the error due to aliasing artifacts during the acquisition. One equivalent anti-aliasing filter designed by our approach is shown in Fig. 3.2(b). It has a narrower transition band, and the responses in the baseband and stopband are close to ideal.

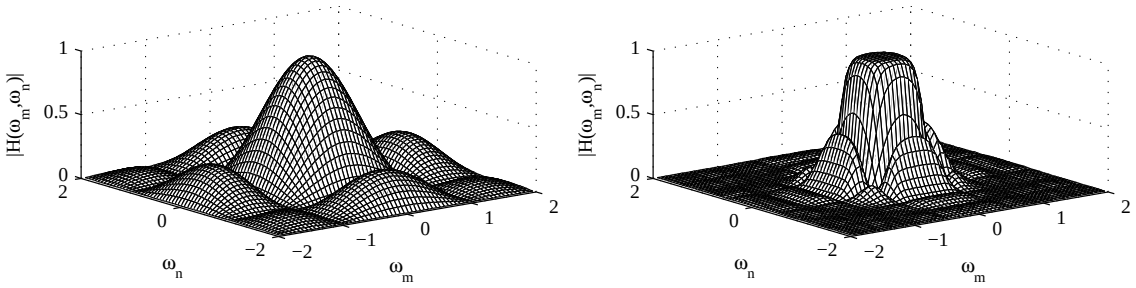

(a) Four-spot birefringent filter (b) Proposed Wiener approach

Figure 3.2: Comparison of the frequency responses of different anti-aliasing filters. The horizontal and vertical frequencies have been normalized by the sampling frequency.

This chapter is organized as follows. The normal imaging model and the proposed defocus acquisition approach are presented in Sec. 3.2. The optimal reconstruction Wiener filter for the defocused image is defined in Sec. 3.3. The criterion to adaptively identify the optimal defocus setting is presented in Sec. 3.4. We summarize our proposed acquisition approach in Sec. 3.5. Simulation results are reported in Sec. 3.6. Finally, we discuss the practical issues and our future work and draw some conclusions in Sec. 3.7.

3.2 Problem Formulation

As described in the previous section, the sub-optimal response of the birefringent anti-aliasing filter results in blurry images with artifacts that cannot be removed by the post-processing step of digital cameras. Much effort has been invested in the past thirty years to optimize the design of the birefringent filter. However, the complexity of the optical design and the limitation of the birefringent materials slow down the pace of innovation on the optical research side. We begin with the definition of the normal imaging model followed by our proposed defocusing acquisition.

3.2.1 Normal Imaging Model

In the frequency domain, let $F(\Omega_x, \Omega_y)$ be the spectrum of a continuous scene as viewed by the camera. If a lowpass anti-aliasing filter $H(\Omega_x, \Omega_y)$ is applied before the camera sensor, the representation of the sampled signal $F_d(\Omega_x, \Omega_y)$ is as follows [66]:

$$F_d(\Omega_x, \Omega_y) = \frac{1}{\Delta_x \Delta_y} \sum_{k=-\infty}^{\infty} \sum_{l=-\infty}^{\infty} H\left(\Omega_x - \frac{2\pi}{\Delta_x}k, \Omega_y - \frac{2\pi}{\Delta_y}l\right) F\left(\Omega_x - \frac{2\pi}{\Delta_x}k, \Omega_y - \frac{2\pi}{\Delta_y}l\right) \tag{3.1}$$

where Δ_x and Δ_y are sampling intervals in the horizontal and vertical directions. Let F_b be the baseband signal of the scene. Then $F_b = F$ for $|\Omega_x| < \frac{2\pi}{\Delta_x}$ and $|\Omega_y| < \frac{2\pi}{\Delta_y}$, and zero otherwise, and denote this support as I. In other words, F_b contains frequency content with frequencies smaller than the Nyquist rate. In the following context, we assume $\Delta_x = \Delta_y = 1$ for simplicity. It is possible to recover the baseband signal F_b without distortion and aliasing using an ideal lowpass filter even if the continuous scene F is not bandlimited. For the non-ideal case, such as using a four-spot birefringent filter H_a, perfect recovery of F_b is not generally possible.

In the spatial domain, if we take the sensor-size effect h_s into account, the corresponding baseband PSF of the equivalent anti-aliasing filter h is a convolution of h_s and the four-spot filter h_a. The normal imaging model can be represented by the following equation:

$$y[m, n] = h[m, n] * f_b[m, n] + f_a[m, n; h] + u[m, n] \tag{3.2}$$

where $y[m, n]$ $(0 \leq m \leq M-1, 0 \leq n \leq N-1)$ is the sampled image captured by the camera, $f_b[m, n]$ is a baseband image without any aliasing, $f_a[m, n; h]$ is the aliasing component filtered by the stopband response of the blur, and u is additive noise. Here, "$*$" represents a two-dimensional convolution.

In practical imaging devices equipped with CMOS sensors, the noise $u[m, n]$ can be modeled as a mixture of independent Gaussian noise and signal-dependent noise [67], expressed

as the following equation:

$$u[m,n] = \left(k_0 + k_1 \left(h[m,n] * f_b[m,n] + f_a[m,n;h]\right)\right) \eta[m,n] \tag{3.3}$$

where k_0 and k_1 are constants and $\eta[m,n]$ follows a standard normal distribution. In most image reconstruction research work, the noise is modeled as independent Gaussian noise that is the special case $k_1 = 0$ of Eq. (3.3). Rather than choosing the same independent model, we use the signal-dependent model in the acquisition side to describe the real-world application more accurately. But we assume signal-independent noise in the formulation of the reconstruction filter and the searching criterion in Sec. 3.3 and 3.4 for simplification.

The reconstructed image $\hat{f}_b[m,n]$ will be estimated from the acquired image $y[m,n]$. It is evident that this is an ill-posed problem because of the aliasing artifact and the appearance of noise. One can choose a popular deconvolution approach such as regularization or Wiener filtering to recover the baseband image $f_b[m,n]$. However, since the knowledge of the continuous scene is absent, it is impossible to identify the aliasing in the captured image $y[m,n]$ by any reconstruction method.

3.2.2 Defocusing Acquisition

The diversity of real-world scenes and the appearance of noise mean that a fixed birefringent anti-aliasing filter may not be the best choice for every scene. For example, a small amount of blur is enough to reduce the artifacts caused by aliasing for a scene with large flat regions or plain backgrounds. On the contrary, a scene with a large amount of high-frequency energy, such as patterns, needs to be blurred further. Because of the lowpass characteristic of out-of-focus blur, a practical method is to automatically defocus a camera lens with the desired blur level to bandlimit the spectrum F instead of using a fixed birefringent filter. The normal imaging model defined in Eq. (3.2) becomes the defocusing imaging model as

follows:

$$y[m,n] = h_o[m,n] * h_s[m,n] * f_b[m,n] + f_a[m,n;h_o,h_s] + u[m,n] \tag{3.4}$$

where $h_o[m,n]$ is the baseband PSF of the out-of-focus blur. The frequency representation of this imaging model can be expressed as follows,

$$Y(\omega_m,\omega_n) = H(\omega_m,\omega_n)F_b(\omega_m,\omega_n) + F_a(\omega_m,\omega_n;H) + U(\omega_m,\omega_n). \tag{3.5}$$

To solve an image reconstruction problem, we normally seek to recover an estimate $\hat{F}_b$ to minimize the reconstruction error:

$$\epsilon^2 = E\left\{\|F_b - \hat{F}_b\|^2\right\} \tag{3.6}$$

However, consistently better results can be obtained if we adapt the amount of the out-of-focus blur generated by the camera lens according to the scene and noise level. According to the imaging model defined in Eq. (3.4), the amount of out-of-focus blur needed for a particular scene is determined by the energy level of frequencies higher than the Nyquist rate of the camera f_a. Although the camera cannot capture f_a, a method to estimate it using a captured image is presented in Sec. 3.3. For example, if the energy of f_a of an input scene is zero, there is no need to add out-of-focus blur during the acquisition. That is, $h_o[m,n] = 1$. When a scene contains a large amount of high-frequency energy, such as texture patterns, the energy level of f_a is large. In this case, a large amount of blur is required to suppress the artifacts caused by f_a. Non-ideal anti-aliasing filters trade off baseband distortion with aliasing. A similar tradeoff is made in determining the degree of defocus.

The adaptive defocusing acquisition is followed by a reconstruction process. By adjusting the defocus, we seek the optimal tradeoff between baseband distortion and aliasing *after*

the reconstruction step is applied. In addition, we must take into account noise amplification error that is introduced in the reconstruction step. The equivalent anti-aliasing filter in our proposed approach is the combination of the out-of-focus blur and the reconstruction filter. Since statistical information about the original scene is required by the subsequent reconstruction step, we capture and then estimate statistical information about the input scene during the acquisition and pass it to the reconstruction. By using this information, the proposed approach generally achieves better estimated images, with less aliasing and sharper edges.

3.3 Optimal Wiener Filter

To obtain the baseband estimate $\hat{F}_b$, a digital filter W is designed to minimize the reconstruction error ϵ^2. The recovered baseband image is then estimated by:

$$\hat{F}_b = WY \tag{3.7}$$

To simplify the development of the filter in the reconstruction error expression, we assume that the noise U and the aliasing signal F_a are uncorrelated with the baseband signal F_b. We found in a wide variety of experiments that this assumption had little impact on the estimated defocus setting. Furthermore, for defining the Wiener filter we assume that the noise is stationary. As a result, W becomes a Wiener filter (linear minimum mean-square error) with the following form [68]:

$$W = \frac{H^*}{|H|^2 + \frac{\sigma_u^2 + S_{f_a}}{S_{f_b}}}, \tag{3.8}$$

where S_{f_b} is the power spectrum of the baseband signal, S_{f_a} is the power spectrum of the aliasing component and σ_u^2 is the noise variance. Here, the "$*$" superscript is a conjugate operation. We treat the aliasing signal as a part of the noise in the Wiener filter, which will

smooth out the aliasing artifacts in the captured images. Our goal is to find the optimal defocus setting with frequency response H_{opt} and the corresponding Wiener filter W_{opt} that minimizes the reconstructed error ϵ^2 for each specific continuous scene with a certain noise level.

Normally, the standard deviation of the additive noise is known or can be readily estimated from the captured image. However, we have no information about the baseband signal F_b and the aliasing signal F_a. The Wiener filter that we defined depends on statistics of these components to balance the aliasing suppression and noise amplification. To estimate the unknown power spectra S_{f_b} and S_{f_a}, an image Y_0 is initially captured with a large amount of out-of-focus blur H_0. We then assume that the aliasing component F_a is sufficiently suppressed in this image so that it can be ignored. The initial image can be described as follows:

$$Y_0 \approx H_0 F_b + U \tag{3.9}$$

Therefore, one can approximate the expected power spectrum of the initial image by:

$$S_{y_0} \approx E\left\{\left|H_0 F_b + U\right|^2\right\} \tag{3.10}$$

Applying the uncorrelated assumption between the baseband image and the noise, the above equation can be rewritten as follows:

$$\begin{aligned} S_{y_0} &\approx E\left\{\left|H_0 F_b\right|^2\right\} + \sigma_u^2 \\ &= \left|H_0\right|^2 S_{f_{b0}} + \sigma_u^2 \end{aligned} \tag{3.11}$$

The expected power spectrum of the initial baseband image $S_{f_{b0}}$ can be derived by solving the above equation:

$$S_{f_{b0}} \approx \frac{S_{y_0} - \sigma_u^2}{\left|H_0\right|^2} \tag{3.12}$$

Using the periodogram estimate $\hat{S}_{y_0} = |Y_0|^2$, we obtain:

$$\hat{S}_{f_{b0}} = \frac{|Y_0|^2 - \sigma_u^2}{|H_0|^2} \tag{3.13}$$

Because the autocorrelation functions and the power spectral density form a Fourier transform duality pair, we can estimate the power spectra of the baseband image and aliasing component from the autocorrelation function of the continuous scene. The generic autocorrelation function we chose is a general decaying-exponential model as follows [69]:

$$\Phi_f(x, y) = \beta e^{-\sqrt{ax^2+by^2+cxy}} + \bar{f}^2 \tag{3.14}$$

where β is a scale factor and $\bar{f}$ is the mean of the continuous scene f. The parameters a, b and c obey the conditions $a > 0$, $b > 0$ and $|c| \leq \sqrt{ab}$. To generate the two power spectra using this generic model, we first obtain the observed autocorrelation function of the baseband signal by taking an inverse Fourier transform of the estimated power spectrum of the baseband image:

$$\Phi_b[m, n] = \mathcal{F}^{-1}\{\hat{S}_{f_{b0}}(\omega_m, \omega_n)\} \tag{3.15}$$

Assume that there exists a positive integer R which satisfies $\Omega_{f_{max}} < \min\{R\frac{\pi}{\Delta_x}, R\frac{\pi}{\Delta_y}\}$, where $\Omega_{f_{max}}$ is the highest frequency content in the continuous scene. In other words, if the sampling frequency of the camera is increased by a factor of R, no aliasing is introduced by the sampling. Let Φ_{f_R} be the autocorrelation function of the observed image with the higher sampling rate. We fit the observed autocorrelation function Φ_b at the spatial location $[m, n]$ to the location $[mR, nR]$ of the autocorrelation function Φ_{f_R}.

To simplify the fitting process, we only select data inside a spatial support Ψ from the autocorrelation function to fit the model. The spatial region Ψ is limited to $[-q, q] \times [-q, q]$. The parameters a, b and c can be estimated using a closed-form solution [70]. If the condition $|c| \leq \sqrt{ab}$ cannot be satisfied during the fitting process, we set parameter $a = b$ and $c = 0$.

The anisotropic model in Eq. (3.14) then degenerates to an isotropic model as follows:

$$\Phi_f(x,y) = \beta e^{-a\sqrt{x^2+y^2}} + \bar{f}^2 \tag{3.16}$$

The power spectrum of the continuous scene $S_{f_R}(\omega_m, \omega_n)$ can be acquired by taking a Fourier transform of $\Phi_{f_R}[m,n]$. We estimate the power spectra of the baseband signal f_b and the aliasing component f_a according to the ratio of the sampling rate R. More precisely, the estimated power spectrum of the baseband signal $S_{f_b}(\omega_m, \omega_n) = S_{f_R}(\omega_m, \omega_n)$ for $|\omega_m| < \frac{\pi}{R}$ and $|\omega_n| < \frac{\pi}{R}$, while the estimated power spectrum of the aliasing signal S_{f_a} is the remaining part of S_{f_R} multiplied by the squared frequency response of the out-of-focus blur, then overlapped together according to the ratio R.

3.4 Optimal Defocusing

As discussed in Sec. 3.2.2, the out-of-focus blur that minimizes the reconstruction error $\epsilon^2 = E\left\{\|F_b - \hat{F}_b\|^2\right\}$ is taken to be the optimal defocus setting H_{opt}. The Wiener filter corresponding to H_{opt} is the optimal reconstruction Wiener filter W_{opt}. Since the Wiener filter balances the noise amplification and deblurring in the reconstruction step, the additive noise plays a crucial role in determining the optimal defocus settings. More specifically, the Wiener filter tends to choose a smaller amount of blur for a scene with a high noise level to achieve the minimum reconstruction error.

Fig. 3.3 shows the true reconstruction error ϵ^2 defined in Eq. (3.6) vs. PSF radius of one test scene at different noise levels. The blur radii corresponding to the minimum point of the reconstruction error is the optimal defocusing. It is evident that an optimal PSF (generally non-zero) radius exists and decreases with an increase of the noise variance. In our simulation, the optimal PSF radius is around 1.5 pixels for most test scenes when the noise energy is small ($k_0 = 1$). When the additive noise level is high, such as $k_0 \geq 8$, the

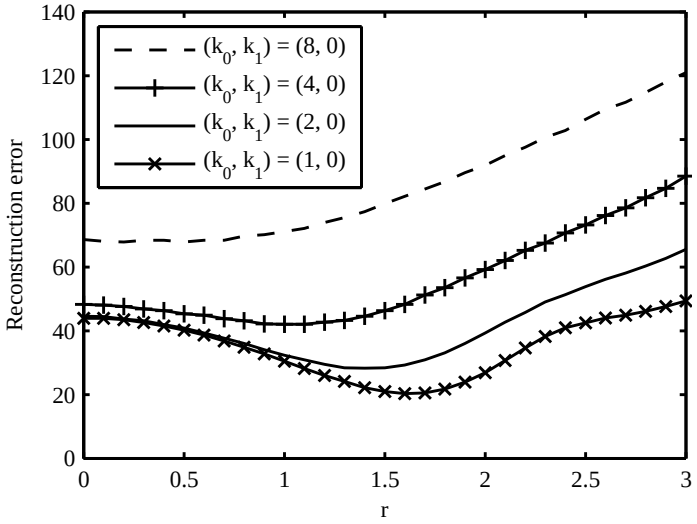

Figure 3.3: Blur radius vs. reconstruction error ϵ^2 defined in Eq. (3.6) of the *Barbara* scene at different noise levels. The additive noise parameters are $(k_0, k_1) = (8, 0)$, $(4, 0)$, $(2, 0)$ and $(1, 0)$. The corresponding blur radius of the minimum reconstruction error (optimal defocusing) increases with a decrease of noise level.

noise amplification error dominates in the Wiener reconstruction. As a result, the optimal PSF radius is reduced to zero for all the test scenes at that noise level.

Searching the optimal defocus setting using the true reconstruction error curves shown in Fig. 3.3 requires little effort from the camera. However, since the baseband signal F_b is unknown, calculating the reconstruction error directly is impossible. Furthermore, it is impractical for a digital camera to capture a set of images with different focus settings for the same scene while tracking the reconstruction error. An alternative approach to approximate the reconstruction error ϵ is preferred.

We propose a criterion to monitor the true ϵ^2 using an approximation $\hat{\epsilon}^2$. Consider a captured image Y with out-of-focus blur H. The expected power spectrum of the estimated baseband image $\hat{F}_b$ can be represented by:

$$S_{\hat{f}_b} = E\left\{|\hat{F}_b|^2\right\} = E\left\{|WY|^2\right\} \approx |WY|^2 \tag{3.17}$$

Using the imaging model formulated in Eq. (3.5) in the equation above and assuming that the aliasing component and noise are uncorrelated with the baseband signal, we can express $S_{\hat{f}_b}$ as

$$\begin{aligned} S_{\hat{f}_b} &= E\left\{|W(HF_b + F_a + U)|^2\right\} \\ &\approx E\left\{|WHF_b|^2\right\} + E\left\{|WF_a|^2\right\} + E\left\{|WU|^2\right\} \\ &= |WH|^2 S_{f_b} + E\left\{|WF_a|^2\right\} + E\left\{|WU|^2\right\} \end{aligned} \tag{3.18}$$

Combining Eq. (3.17) with Eq. (3.18) and rearranging the result, we have:

$$E\left\{|WF_a|^2\right\} + E\left\{|WU|^2\right\} \approx |WY|^2 - |WH|^2 S_{f_b} \tag{3.19}$$

Using the imaging model defined in Sec. 3.2.2, the true reconstruction error ϵ^2 can be expressed as follows:

$$\begin{aligned} \epsilon^2 &= E\left\{\|F_b - \hat{F}_b\|^2\right\} \\ &= E\left\{\|(1 - WH)F_b - WF_a - WU\|^2\right\} \end{aligned} \tag{3.20}$$

We must approximate the true reconstruction error ϵ^2 with computable quantities. Applying Eq. (3.19) and again assuming the baseband signal F_b is uncorrelated with the aliasing signal F_a and noise U, one can approximate the above equation as follows:

$$\begin{aligned} \epsilon^2 &\approx E\left\{\|(1 - WH)F_b\|^2\right\} + E\left\{\|WF_a\|^2\right\} + E\left\{\|WU\|^2\right\} \\ &\approx \sum_{\omega_m \in I} \sum_{\omega_n \in I} \left[|1 - WH|^2 S_{f_b} + |WY|^2 - |WH|^2 S_{f_b}\right] \\ &= \sum_{\omega_m \in I} \sum_{\omega_n \in I} \left[\left(|1 - WH|^2 - |WH|^2\right) S_{f_b} + |WY|^2\right] \\ &= \sum_{\omega_m \in I} \sum_{\omega_n \in I} \left[\left(1 - 2\Re\{WH\}\right) S_{f_b} + |WY|^2\right], \end{aligned} \tag{3.21}$$

where $\Re\{\cdot\}$ denotes the real part of a complex number. Approximating both S_{f_b} and $|WY|^2$ with the estimated power spectrum $\hat{S}_{f_{b0}}$ of the initial image derived in Eq. (3.13), we have

the estimate reconstruction error $\hat{\epsilon}^2$:

$$\hat{\epsilon}^2 \approx \sum_{\omega_m \in I} \sum_{\omega_n \in I} \Big[(2 - 2\Re\{WH\})\, \hat{S}_{f_{b0}} \Big]. \tag{3.22}$$

The out-of-focus blur $\hat{H}_{opt}$ and the corresponding Wiener filter $\hat{W}_{opt}$ which result in the minimum $\hat{\epsilon}^2$ value are considered to be the optimal defocus setting. An adaptive acquisition can be accomplished by capturing the scene using the out-of-focus blur $\hat{H}_{opt}$ and recovering it by $\hat{W}_{opt}$. The curves in Fig. 3.4 depict the true and estimated reconstruction errors vs. the PSF radius for two test scenes. It is evident that our criterion tracks the true optimal defocus setting as expected.

This criterion is automatically adapted to the power spectrum of the scene, which is estimated via the initially captured image. Without mechanically moving the actual lens, a digital camera can evaluate the reconstruction error for a specific scene using a look-up table which defines the PSF of the lens as a function of radius. Because only the initial image y_0 needs to be captured to find the optimal defocus setting, this criterion is appealing for real-time applications.

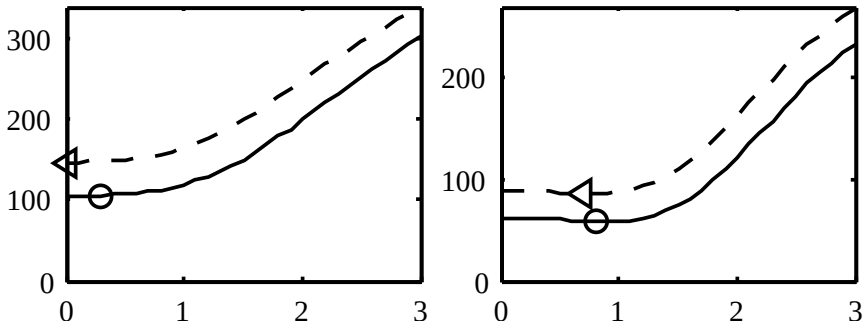

(a) Scene No. 5, $(k_0 = 8, k_1 = 0.1)$

(b) Scene No. 5, $(k_0 = 4, k_1 = 0.1)$

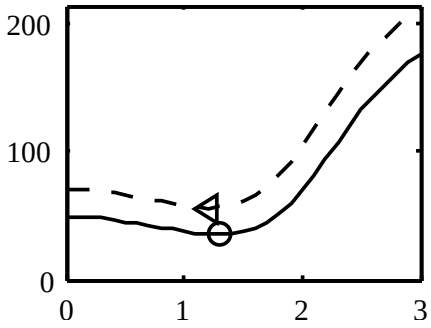

(c) Scene No. 5, $(k_0 = 2, k_1 = 0.1)$

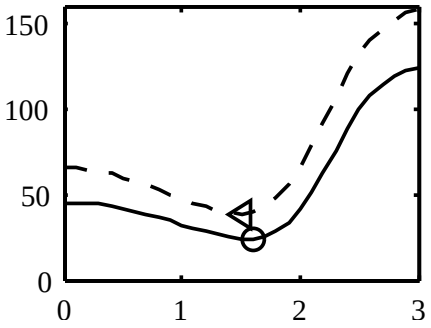

(d) Scene No. 5, $(k_0 = 1, k_1 = 0.1)$

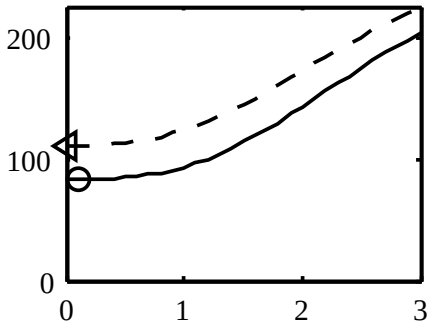

(e) Scene No. 51, $(k_0 = 8, k_1 = 0.1)$

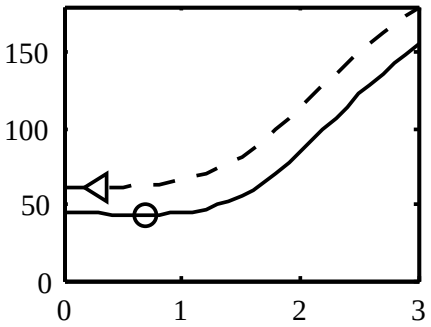

(f) Scene No. 51, $(k_0 = 4, k_1 = 0.1)$

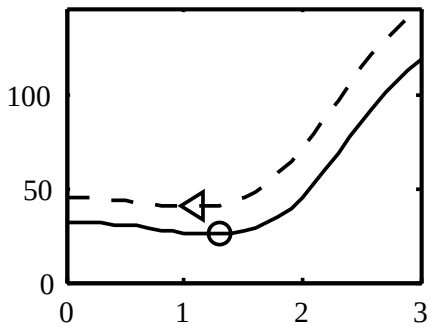

(g) Scene No. 51, $(k_0 = 2, k_1 = 0.1)$

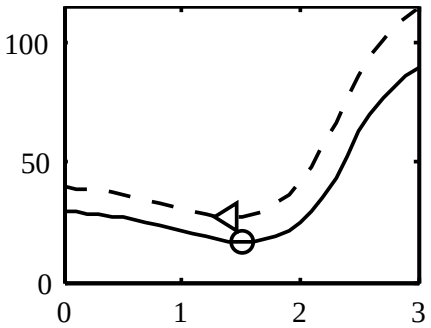

(h) Scene No. 51, $(k_0 = 1, k_1 = 0.1)$

Figure 3.4: Comparison of the true (—) and estimated (– –) reconstruction errors ϵ^2 (vertical axis) vs. the PSF radius r (horizontal axis) for different noise levels. The true and estimated optimal blur radii were labeled by "$\circ$" and "$\triangleleft$".

3.5 Summary

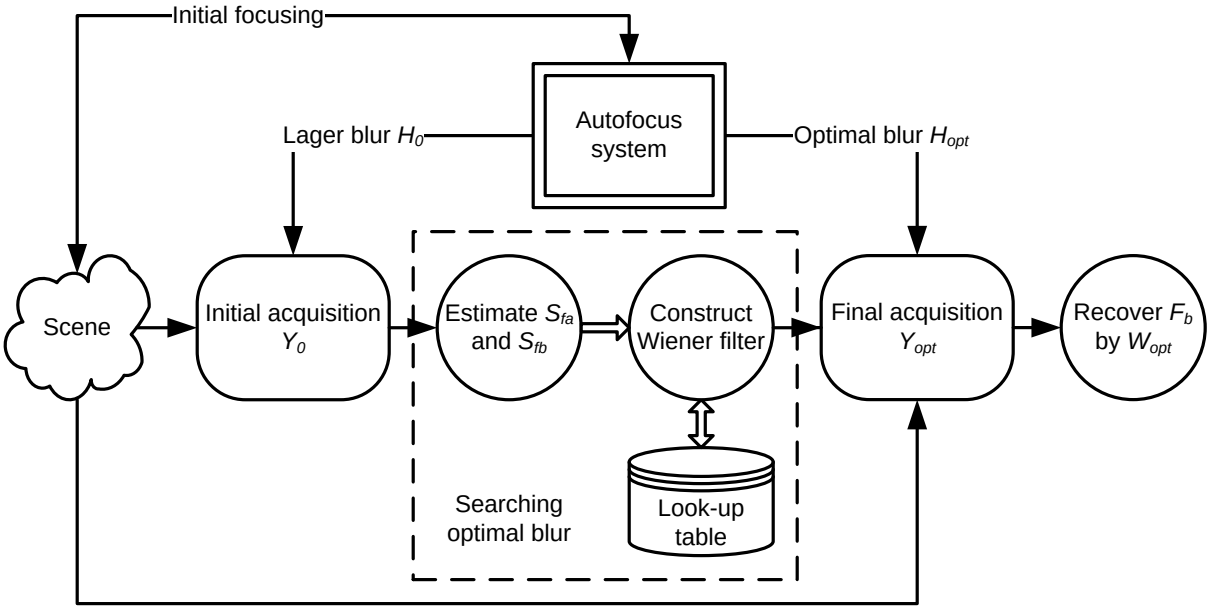

Figure 3.5: The flowchart of adaptive auto-defocusing approach.

We summarize our adaptive acquisition approach in this section. A flowchart of our proposed method is shown in Fig. 3.5. In particular, the algorithm can be described by the following steps.

1. **Initial focusing.** Search the optimal focus setting for a continuous scene by the autofocus system of the camera. The same focusing process can be found in digital cameras equipped with an autofocus lens.

2. **Initial acquisition.** Move the lens to the out-of-focus position and generate the initial blur H_0. Capture the initial image Y_0 with this defocus setting.

3. **Searching optimal defocusing.** Perform the following sub-steps after the initial acquisition.

   (a) *Estimate S_{f_a} and S_{f_b}.* Compute the observed baseband power spectrum $\hat{S}_{f_{b0}}$ using Eq. (3.12). Fit the estimated autocorrelation function to a decaying-exponential

model with a higher sampling frequency. Derive the power spectra S_{f_a} and S_{f_b} from the Fourier transform of the autocorrelation of the continuous scene.

(b) *Construct Wiener filter.* For the different defocus settings defined in the look-up table of the camera, construct Wiener filters using Eq. (3.8). Search for the minimum of estimated reconstruction error using the criterion in Eq. (3.22). The corresponding PSF H_{opt} is the optimal defocus setting.

4. **Final acquisition.** Move the lens again to generate the optimal out-of-focus blur H_{opt}, and capture the final image Y_{opt}.

5. **Reconstruction.** Recover the final image Y_{opt} with the Wiener filter W_{opt} corresponding to the optimal PSF H_{opt}.

3.6 Simulation and Results

In this section, we present some experimental results to verify the defocusing acquisition and evaluate the performance of the criterion we proposed in Sec. 3.4. We chose 100 grayscale images and considered them as continuous scenes. In particular, our image library contains the following four databases. Images No. 1–24 are the twenty-four test images from the Kodak PhotoCD set [71]. Images No. 25–54 are the thirty original test images from the content-based strategies of image quality (CSIQ) database [72]. Images No. 55–64 are from the image and video-communication (IVC) database for subjective quality assessment [73]. The remaining thirty-six images were taken by a Nikon D90 digital single-lens reflex (DSLR) camera. These color images were converted to grayscale images and cropped to size 512×512. The intensity values of these natural images are between 0 and 255. Each image was subsampled by a factor of R in both directions to model the sampling processing.

Each resulting image acquired by the proposed approach was evaluated by comparing it to the baseband image. In addition to reporting mean square error (MSE), we report the performance of our proposed approach with the structural similarity (SSIM) index value [74].

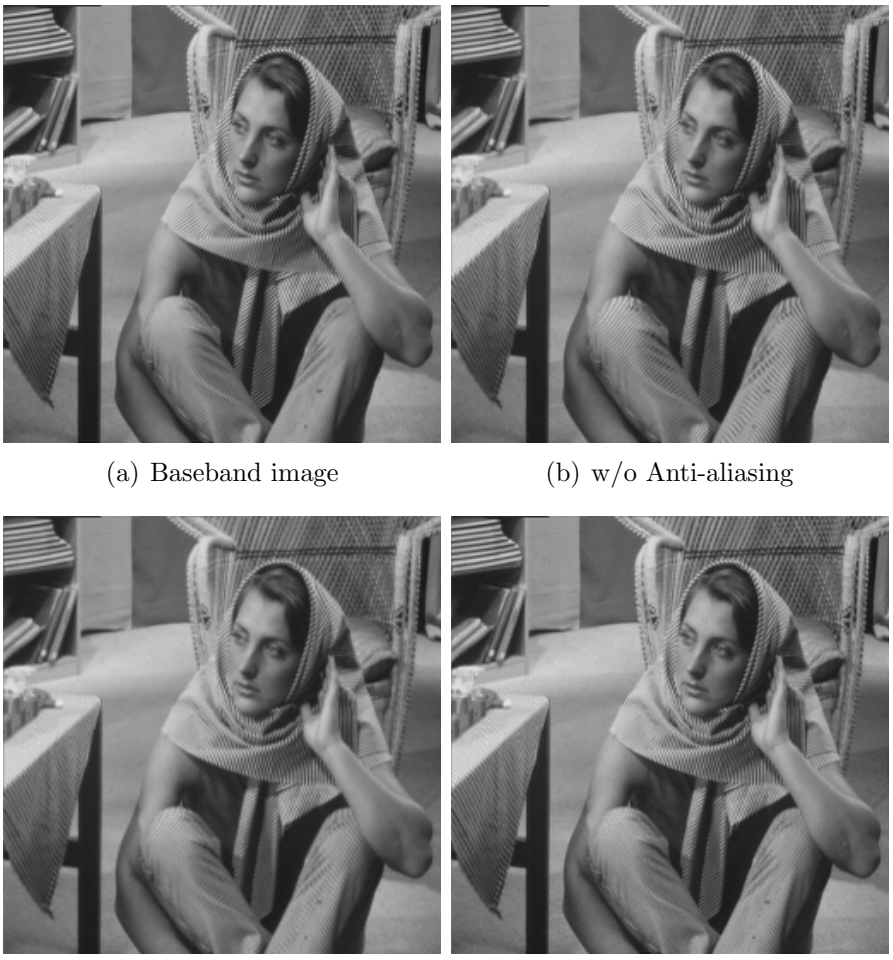

(a) Baseband image (b) w/o Anti-aliasing

(c) w/ Anti-aliasing (d) Defocusing acquisition

Figure 3.6: Cropped *Barbara* images acquired by three different methods. The additive noise parameters are $(k_0, k_1) = (1, 0.1)$ and the downsampling rate $R = 2$.

The structural-similarity-based image quality assessment depends on the image structure, which more accurately represents the human visual system. Since traditional measures of image quality, such as MSE, do not always correspond well to subjective quality, SSIM can be used as a complementary approach to evaluate the image quality. The source code of SSIM assessment used was downloaded from the authors' website.

We conducted simulation experiments as follows. The downsampling rate R was set to 2 and 4. A 2×2 averaging filter was added in the process as the sensor-size effect for the $R = 2$ case. A 4×4 averaging filter was chosen for the same purpose in the other case. The same filter as the sensor-size effect was used to simulate the four-spot birefringent

filter in different downsampling cases. The baseband image for each scene was calculated using an ideal lowpass filter. Since the PSF of out-of-focus blur is close to circular [75], we implemented defocusing using a circular blur with different radii r. The spatial region Ψ defined in Sec. 3.3 was set to $[-4, 4] \times [-4, 4]$ to match the autocorrelation model. The initial image y_0 was acquired using blur with $r = 1.5$ pixels. The blur radius at the minimum point of $\hat{\epsilon}^2$ is the estimated optimal blur radius $\hat{r}_{opt}$.

Both the cropped *Barbara* images and a portion of No. 8 test image shown in Fig. 3.6 and 3.7 depict various acquisition methods. The input images were downsampled by 2 and corrupted by signal-dependent noise with parameters $(k_0, k_1) = (2, 0.1)$. Visual results are noticeably improved compared to the image acquired without any anti-aliasing filter, especially in regions with high-frequency patterns, such as the pants in the *Barbara* image. In Fig. 3.7(d), the diagonal Moiré patterns on the window shutters were completely removed by our approach. Although the aliasing artifacts in the image acquired by the four-spot birefringent filter have been greatly reduced, the edges are blurrier than the image acquired by the proposed method. Fig. 3.8 shows that similar performance also can be achieved when using a higher downsampling rate, such as $R = 4$.

Table 3.1 reports the performance of different acquisition approaches for different noise levels with $k_0 \in \{1, 2, 4, 8\}$ and $k_1 \in \{0, 0.2\}$. The average MSE over 100 test scenes shows that the proposed acquisition method outperforms traditional methods (with or without an anti-aliasing filter) at different noise levels. Images acquired without an anti-aliasing filter have lower MSE values than images acquired with an anti-aliasing filter. The reason is that the distortion produced by the anti-aliasing filter is increased more than the aliasing artifact is reduced in terms of MSE.

The average SSIM index values of different acquisition approaches over 100 test scenes are shown in Table 3.2. We chose the same noise levels used in Table 3.1. The SSIM index value is designed to be in the range from 0 to 1. The larger SSIM index value indicates two images are more similar to each other. In this test, we compare the result images acquired by

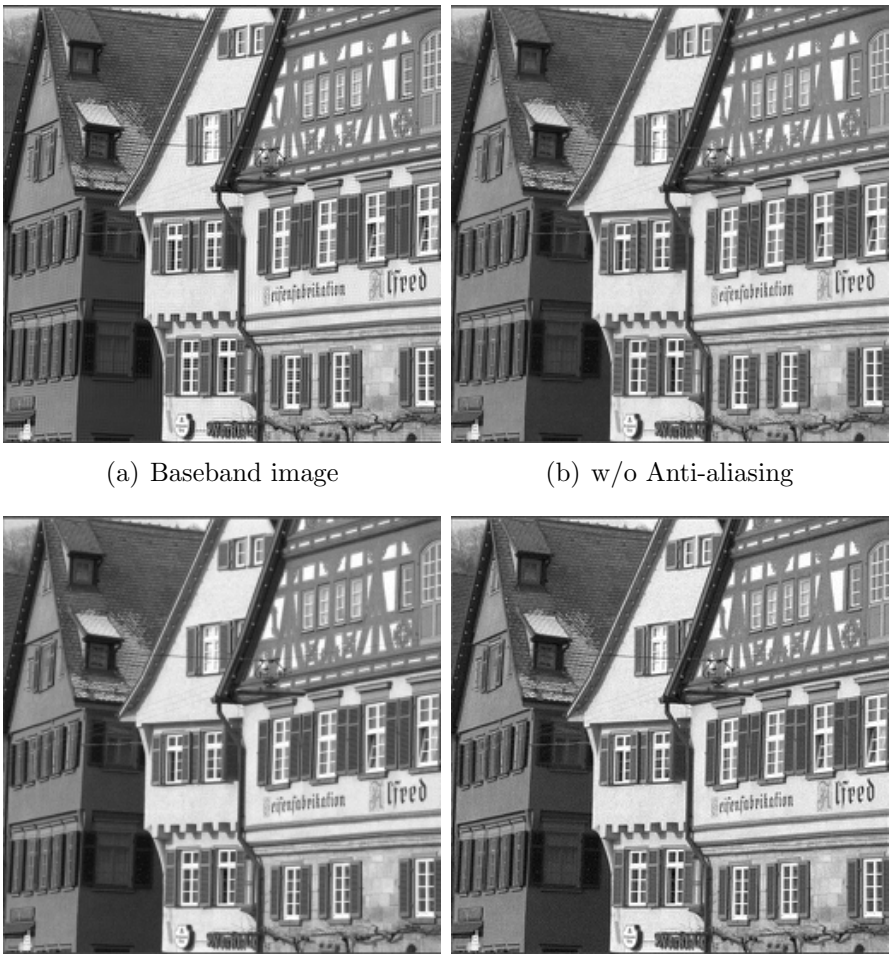

(a) Baseband image (b) w/o Anti-aliasing

(c) w/ Anti-aliasing (d) Defocusing acquisition

Figure 3.7: Portion of No. 8 images captured by by three different methods. The additive noise parameters are $(k_0, k_1) = (2, 0.1)$ and the downsampling rate $R = 2$.

different approaches with the true baseband image. The average SSIM index values confirm that a better performance can be achieved using our proposed acquisition method.

To verify the accuracy of the criterion derived in Sec. 3.4, we compared the optimal radius $\hat{r}_{opt}$ estimated using this criterion with the true r_{opt} for different scenes and noise levels. The mean absolute difference $|r_{opt} - \hat{r}_{opt}|$ in Table 3.3 for the downsampling-by-2 experiment is less than 0.35 pixels and the corresponding MSE loss Δ_{MSE} is less than 1.7, which demonstrate that the algorithm we have proposed is robust with respect to various noise levels. When a higher downsampling rate is used ($R = 4$), the differences $|r_{opt} - \hat{r}_{opt}|$

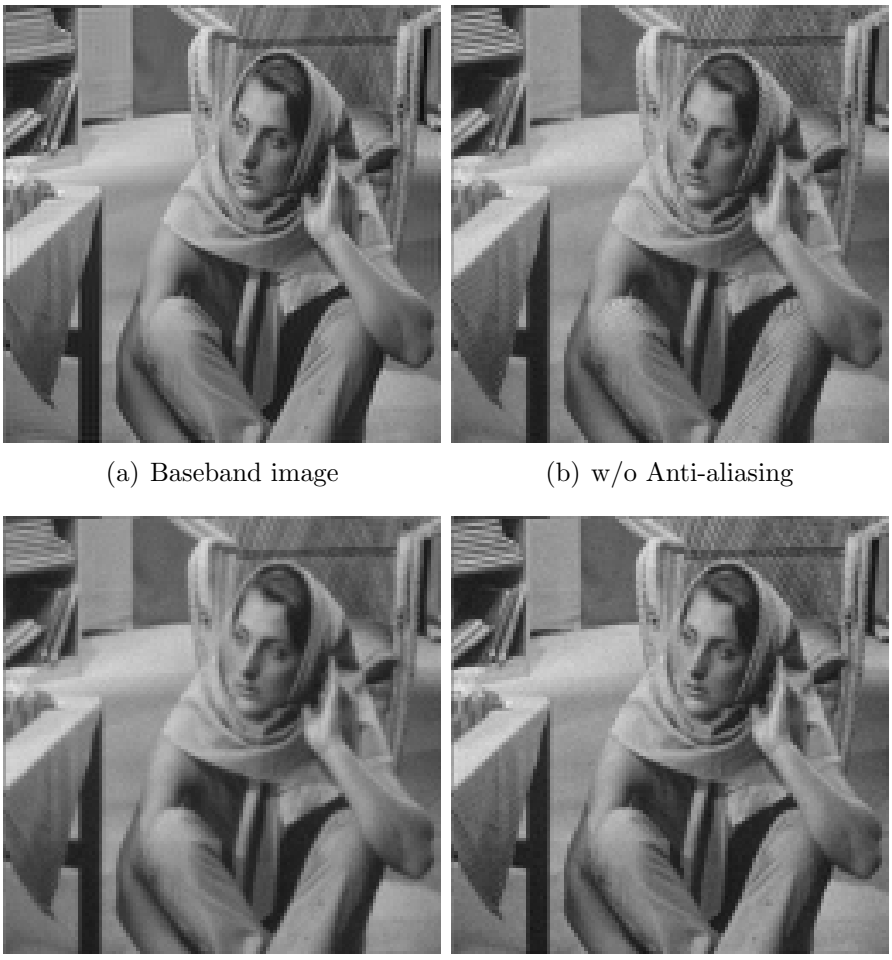

(a) Baseband image (b) w/o Anti-aliasing

(c) w/ Anti-aliasing (d) Defocusing acquisition

Figure 3.8: The comparison of captured *Barbara* image with downsampling rate $R = 4$ by three different methods. The additive noise parameters are $(k_0, k_1) = (2, 0.1)$.

increase for lower noise levels, when $k_0 = 2$ and 1. But the MSE losses are still small compared to the MSE improvement in Table 3.1.

The performance of our criterion drops for a few test scenes. Fig. 3.9 shows the true and estimate reconstruction error plots for one (No. 8 test scene) of these counterexamples. The estimated optimal blur radius $\hat{r}_{opt}$ is 0.3 pixels using our criterion, but the true value r_{opt} is 0.8 pixels for this test scene. However, the MSE loss caused by the mis-estimate is less than 1 and our method still results in a better MSE value than the traditional methods (proposed: 12.4, w/o AA: 13.5, w/ AA: 12.7). The marginal improvement of our method is due to less high-frequency content in this scene compared to others. The cropped result

Table 3.1: Image acquisition methods compared using average MSE over 100 test scenes with different noise levels. The downsampling rate are $R = 2, 4$ and the additive noise settings are $(k_0, k_1) = (8, 0)$, $(8, 0.2)$, $(4, 0)$, $(4, 0.2)$, $(2, 0)$, $(2, 0.2)$, $(1, 0)$, $(1, 0.2)$.

Rate	(k_0, k_1)	w/o AA	w/ AA	Proposed
$R = 2$	$(8, 0)$	89.1	89.2	**68.8**
	$(8, 0.2)$	90.5	90.7	**69.5**
	$(4, 0)$	41.1	41.2	**36.7**
	$(4, 0.2)$	41.8	41.9	**37.3**
	$(2, 0)$	29.1	29.2	**21.2**
	$(2, 0.2)$	29.4	29.6	**21.9**
	$(1, 0)$	26.1	26.2	**13.2**
	$(1, 0.2)$	26.3	26.4	**14.1**
$R = 4$	$(8, 0)$	96.6	100.6	**80.1**
	$(8, 0.2)$	98.0	102.1	**81.1**
	$(4, 0)$	48.5	52.6	**43.0**
	$(4, 0.2)$	49.3	53.3	**43.7**
	$(2, 0)$	36.5	40.6	**26.0**
	$(2, 0.2)$	36.9	41.0	**26.9**
	$(1, 0)$	33.5	37.6	**16.2**
	$(1, 0.2)$	33.7	37.7	**17.1**

images of No. 3 test scene acquired by different methods are shown in Fig. 3.10. The visual inspection of these images confirms the conclusion drawn from the numerical analysis.

3.7 Conclusion and Discussion

In this chapter, an adaptive image acquisition approach has been introduced. A new imaging model of defocusing acquisition has been defined that considers both aliasing and noise. A criterion to estimate the optimal defocus setting for a specific scene was derived. The model-based Wiener filter is used to minimize the end-to-end reconstruction error during the acquisition. Both the Wiener filter and the criterion are adapted to the power spectrum of the input scene. Numerical and visual results show that the proposed approach outperforms traditional acquisition methods with or without a fixed anti-aliasing filter. The proposed approach is robust with respect to various noise levels, and it is practical in some cases to replace the commonly used four-spot birefringent filter with this method.

Table 3.2: Image acquisition methods compared using average SSIM index value over 100 test scenes with different noise levels. The downsampling rate are $R = 2, 4$ and the additive noise settings are $(k_0, k_1) = (8, 0)$, $(8, 0.2)$, $(4, 0)$, $(4, 0.2)$, $(2, 0)$, $(2, 0.2)$, $(1, 0)$, $(1, 0.2)$.

Rate	(k_0, k_1)	w/o AA	w/ AA	Proposed
$R = 2$	$(8, 0)$	0.7599	0.7649	**0.8426**
	$(8, 0.2)$	0.7567	0.7519	**0.8412**
	$(4, 0)$	0.8940	0.8927	**0.9120**
	$(4, 0.2)$	0.8911	0.8895	**0.9103**
	$(2, 0)$	0.9467	0.9467	**0.9489**
	$(2, 0.2)$	0.9447	0.9446	**0.9470**
	$(1, 0)$	0.9620	0.9624	**0.9677**
	$(1, 0.2)$	0.9609	0.9613	**0.9658**
$R = 4$	$(8, 0)$	0.7968	0.7891	**0.8496**
	$(8, 0.2)$	0.7946	0.7867	**0.8483**
	$(4, 0)$	0.9062	0.9018	**0.9156**
	$(4, 0.2)$	0.9037	0.8996	**0.9138**
	$(2, 0)$	0.9468	0.9441	**0.9517**
	$(2, 0.2)$	0.9453	0.9426	**0.9498**
	$(1, 0)$	0.9585	0.9562	**0.9688**
	$(1, 0.2)$	0.9577	0.9553	**0.9671**

In comparison with the traditional birefringent filter, images captured by our proposed approach have fewer artifacts. Furthermore, our approach is adaptive to input scenes and minimizes the reconstruction error to achieve better image quality, while the birefringent filter is fixed for every scene. By replacing the birefringent filter with our approach, digital cameras will be lighter and cost less. The downside of our approach is the longer acquisition time caused by the searching of the optimal defocus setting and the final lens movement, though this should be only a small addition to the overhead required for autofocusing. For the color imaging case, chromatic aberration of the lens affects the choice of the optimal defocus setting. Also, single-sensor cameras use Bayer color filter arrays to acquire color images. The extra demosaicking process increases the complexity of our proposed approach.

Table 3.3: Evaluations of the criteria in Sec. 3.4 over 100 test scenes with different downsampling rate $R = 2$, 4 and noise levels $(k_0, k_1) = (8, 0)$, $(8, 0.2)$, $(4, 0)$, $(4, 0.2)$, $(2, 0)$, $(2, 0.2)$, $(1, 0)$, $(1, 0.2)$. The unit of mean absolute difference $|r_{opt} - \hat{r}_{opt}|$ is pixels.

Rate	(k_0, k_1)	$\lvert r_{opt} - \hat{r}_{opt} \rvert$	Δ_{MSE}
$R = 2$	$(8, 0)$	0.12	0.26
	$(8, 0.2)$	0.10	0.20
	$(4, 0)$	0.36	1.07
	$(4, 0.2)$	0.34	0.99
	$(2, 0)$	0.22	0.75
	$(2, 0.2)$	0.23	0.80
	$(1, 0)$	0.11	0.32
	$(1, 0.2)$	0.14	0.48
$R = 4$	$(8, 0)$	0.01	0.05
	$(8, 0.2)$	0.01	0.05
	$(4, 0)$	0.21	1.42
	$(4, 0.2)$	0.20	1.34
	$(2, 0)$	0.32	1.86
	$(2, 0.2)$	0.33	1.95
	$(1, 0)$	0.20	0.97
	$(1, 0.2)$	0.21	1.06

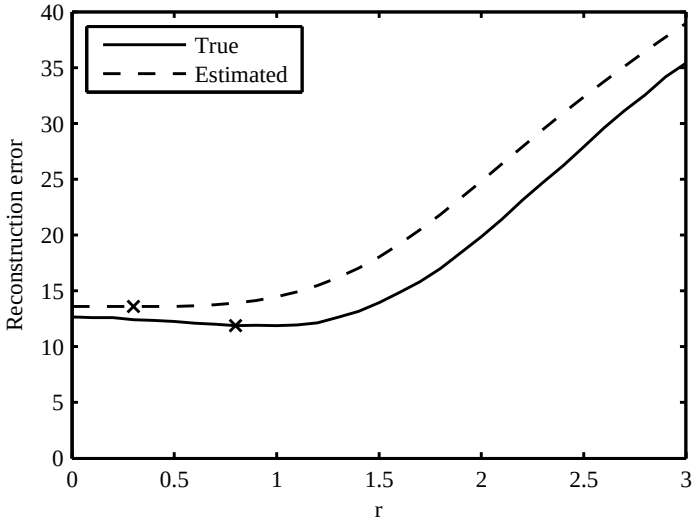

Figure 3.9: Comparison of the true and estimated reconstruction error of No. 3 test scene.

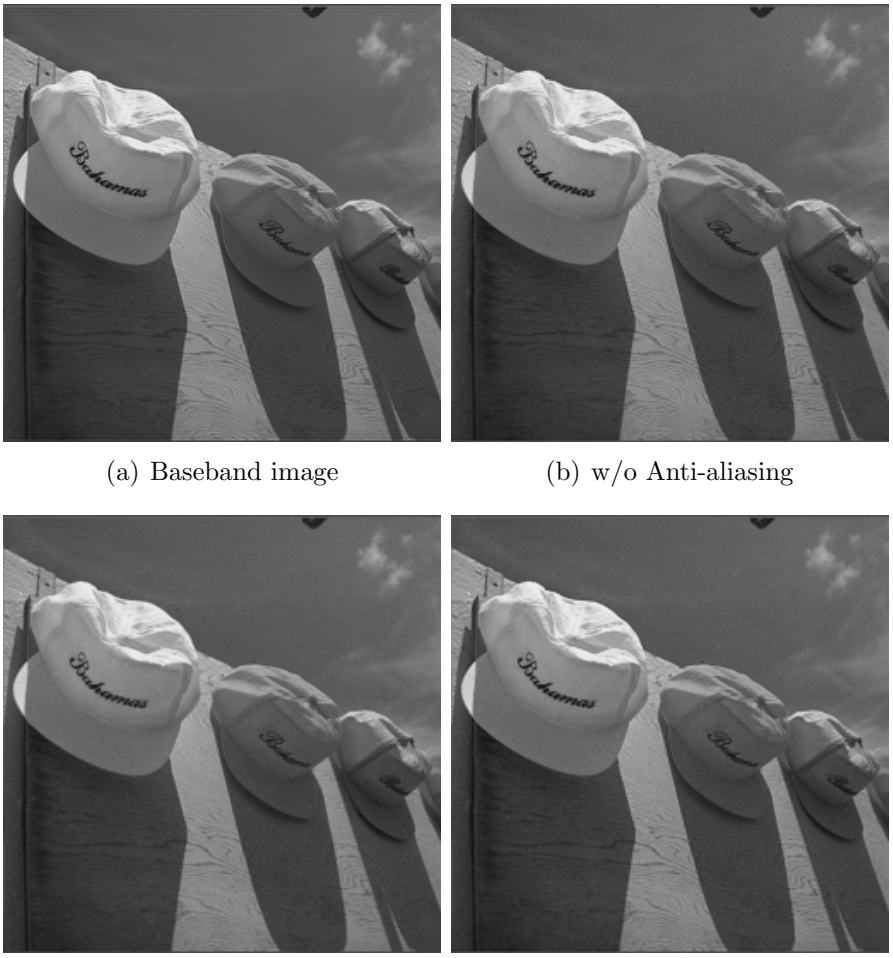

(a) Baseband image (b) w/o Anti-aliasing

(c) w/ Anti-aliasing (d) Defocusing acquisition

Figure 3.10: Comparison of captured No. 3 image with downsampling rate $R = 2$ by three different methods. The additive noise parameters are $(k_0, k_1) = (2, 0)$.

Chapter 4

Color Image Defocusing Acquisition

An extension of the defocusing acquisition from grayscale imaging to color imaging is presented in this chapter for more practical applications. Color cameras acquire at least three channels at different wavelengths to reproduce a color scene. Each channel could be treated as a grayscale image. The extension of the color defocusing acquisition for multi-sensor cameras, whose sensors are dedicated to each light spectrum, is straightforward. One solution is to choose one color plane, such as the green, and find the optimal focus setting for the other two color planes. Because most digital cameras sample a multi-spectrum of light with a single sensor and a color filter, we must consider the extra demosaicking process during the acquisition. As a result, the single-channel Wiener filter we defined in Chapter 3 is extended to a multichannel reconstruction filter. In this section, for simplicity we only investigate the defocusing acquisition for cameras equipped with the most commonly used CFA pattern — the Bayer pattern.

As described in Chapter 2, Bayer CFA sampling generates spectrum copies in the frequency domain. A multichannel Wiener filter in the RGB domain is difficult to implement because the sampling rate of green is two times higher than the sampling rate of red or blue. The high cross-correlation among channels makes the multichannel Wiener filter not diagonalizable by a Fourier transform. A color imaging model in the RGB domain with a multichannel Wiener filter is presented this chapter first. After analyzing the drawbacks of this model, we designed another imaging model with a simplified Wiener filter in the luminance/chrominance domain. An error criterion is formulated to enable the camera find the optimal defocusing setting according to the scene.

4.1 Problem Formulation in RGB Domain

Most color imaging models for demosaicking are defined in the RGB domain. The color defocusing acquisition involves out-of-focus blur in the imaging step. On the reconstruction side, a joint deblurring and demosaicking is required to accomplish the degraded CFA restoration. We first formulated this problem in the RGB domain and designed a Wiener filter with a fast implementation method. However, the spectral correlation depends significantly on the input scene, which makes it difficult to build an adaptive algorithm on this model. Although this model deals with this particular problem unsuccessfully, it could be a solution for other non-adaptive applications. We present it in this section for this purpose.

4.1.1 RGB Color Imaging Model

Consider a camera with an $m_0 \times n_0$ sensor array that samples three color channels at each pixel location according to the Bayer pattern and denote $N = m_0 \times n_0$. Let vectors f_r, f_g and $f_b \in \mathbb{R}^{N\times 1}$ be the baseband images of the red, green and blue channels, and the corresponding aliasing components are described by the vectors f_{ar}, f_{ag} and $f_{ab} \in \mathbb{R}^{N\times 1}$. The four mosaicked color images y_r, y_{g_1}, y_{g_2} and $y_b \in \mathbb{R}^{N/4\times 1}$ shown in Fig. 4.1 can be represented by the following equations:

$$\begin{aligned} y_r &= D_r H_r f_r + D_r H_{ar} f_{ar} + u_r \\ y_{g_1} &= D_{g_1} H_g f_g + D_{g_1} H_{ag} f_{ag} + u_{g_1} \\ y_{g_2} &= D_{g_2} H_g f_g + D_{g_2} H_{ag} f_{ag} + u_{g_2} \\ y_b &= D_b H_b f_b + D_b H_{ab} f_{ab} + u_b \end{aligned} \tag{4.1}$$

The terms D_r, D_{g_1}, D_{g_2} and $D_b \in \mathbb{R}^{N/4\times N}$ are row-deficient identity matrices with missing rows corresponding to missing color samples removed by the color filter array. H_r, H_g and $H_b \in \mathbb{R}^{N\times N}$ are circulant matrices that describe the baseband response of the out-of-focus blur in different color planes, assuming periodic boundaries of the image. Similarly, the

corresponding stopband responses of the out-of-focus blur are represented by the matrices H_{ar}, H_{ag} and $H_{ab} \in \mathbb{R}^{N\times N}$. The vectors u_r, u_{g_1}, u_{g_2} and $u_b \in \mathbb{R}^{N/4\times 1}$ represent the additive noise in distinct channels.

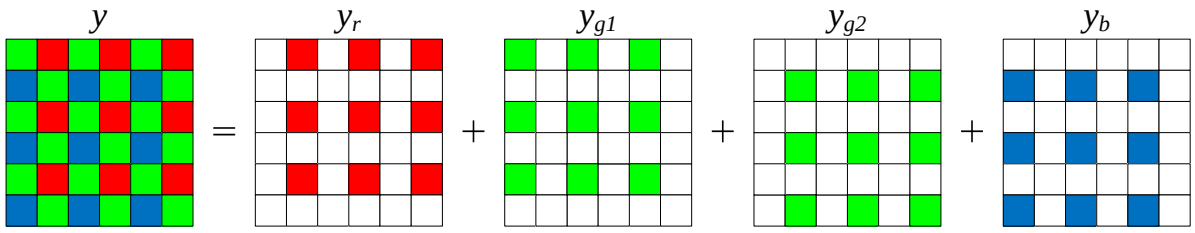

Figure 4.1: Bayer CFA and four subsampled images.

One can describe the above imaging model as a single linear equation as follows:

$$y = DHf + DH_a f_a + u, \tag{4.2}$$

where the acquired CFA image $y \in \mathbb{R}^{N\times 1}$ and the additive noise $u \in \mathbb{R}^{N\times 1}$ are of the forms $y = [y_r^T, y_{g_1}^T, y_{g_2}^T, y_b^T]^T$ and $u = [u_r^T, u_{g_1}^T, u_{g_2}^T, u_b^T]^T$. The baseband image f and passband image $f_a \in \mathbb{R}^{4N\times 1}$ have the forms $f = [f_r^T, f_g^T, f_g^T, f_b^T]^T$ and $f_a = [f_{ar}^T, f_{ag}^T, f_{ag}^T, f_{ab}^T]^T$. The block diagonal matrices D, H and H_a have the forms: $D = \mathrm{diag}(D_r, D_{g_1}, D_{g_2}, D_b)$, $H = \mathrm{diag}(H_r, H_g, H_g, H_b)$ and $H_a = \mathrm{diag}(H_{ar}, H_{ag}, H_{ag}, H_{ab})$. To simplify the problem, we assume that the responses of the out-of-focus blur generated by the camera lens is identical in different color channels. Consequently, the baseband responses of the blur are the same; that is, $H_r = H_g = H_b$. Similarly, we have $H_{ar} = H_{ag} = H_{ab}$ for the stopband responses of the blur. The extension to the case of different responses is straightforward.

In the normal image reconstruction problem, the goal is to recover the baseband image f from the noisy CFA image y. However, we intend to seek the optimal out-of-focus blur with responses H and H_a that automatically adapts to the input scene during the acquisition. The reconstruction filter corresponding to the optimal blur achieves the optimal acquisition by means of linearly minimizing the reconstruction errors.

4.1.2 Multichannel Wiener Filter in RGB Domain

The estimate of the baseband color image $\hat{f}$ is recovered by a multichannel Wiener filter W, where $\hat{f} = Wy$. The multichannel Wiener filter W (linear minimum mean-square error) is given by the following form:

$$W = E\left\{fy^T\right\} E\left\{yy^T\right\}^{-1}. \tag{4.3}$$

Assuming the wide-sense stationarity of the signal and noise and applying Eq. (4.2), one can rewrite the above equation as follows:

$$\begin{aligned} W = &\left(R_f H^T D^T + R_{ff_a} H_a^T D^T + R_{fu}\right)\left(DHR_f H^T D^T + DHR_{ff_a} H_a^T D^T + DHR_{fu}\right. \\ &\left. + DH_a R_{f_a f} H^T D^T + DH_a R_{f_a} H_a^T D^T + DH_a R_{f_a u} + R_{uf} H^T D^T + R_{uf_a} H_a^T D^T + R_u\right)^{-1} \end{aligned} \tag{4.4}$$

Normally, the additive noise u and aliasing component f_a are small compared to the baseband signal f. We further assume that they are uncorrelated with each other; that is, $R_{ff_a} = R_{fu} = R_{f_a f} = R_{f_a u} = R_{uf} = R_{uf_a} = 0$. The simplified multichannel Wiener filter is described as follows:

$$W = R_f H^T D^T \left[DHR_f H^T D^T + DH_a R_{f_a} H_a^T D^T + R_u\right]^{-1} \tag{4.5}$$

The autocorrelation matrices R_f and $R_{f_a} \in \mathbb{R}^{4N \times 4N}$ have the same structure. Both of them contain the spatial and spectral correlation coefficients of the scene, which essentially describes a three-dimensional correlation (2D spatial correlation and 1D spectral correlation) in a two-dimensional matrix. A common model of matrix R_f is discussed here, while the model of R_{f_a} can be derived using the same method.

If we assume that the spatial and spectral correlation are separable, R_f can be described by a Kronecker product as follows:

$$R_f = r \otimes R \tag{4.6}$$

where $R \in \mathbb{R}^{N\times N}$ is the spatial autocorrelation matrix of each color plane. The spectral correlation matrix $r \in \mathbb{R}^{4\times 4}$ has the following form:

$$r = \begin{bmatrix} r_{rr} & r_{rg_1} & r_{rg_2} & r_{rb} \\ r_{g_1r} & r_{g_1g_1} & r_{g_1g_2} & r_{g_1b} \\ r_{g_2r} & r_{g_2g_1} & r_{g_2g_2} & r_{g_2b} \\ r_{br} & r_{bg_1} & r_{bg_2} & r_{bb} \end{bmatrix} \tag{4.7}$$

where the constant r_{ij}, $i, j \in \{r, g_1, g_2, b\}$ defines the spectral correlation between channel i and j. If we assume the signal is periodic in the spatial domain, R becomes a circulant matrix. We have $r_{rr} = r_{g_1g_1} = r_{g_2g_2} = r_{bb} = r_{g_1g_2} = r_{g_2g_1} = 1$. To simplify the spectral correlation, we use a constant α, $0 < \alpha < 1$, to model the dependence among the three channels. In particular, $r_{rg_1} = r_{rg_2} = r_{g_1r} = r_{g_1b} = r_{g_2r} = r_{g_2b} = r_{bg_1} = r_{bg_2} = \alpha$. Because red and blue channels are approximately twice as far apart in spectral wavelength, they are less correlated. We set $r_{r_b} = r_{b_r} = \alpha^2$. As a result, the spectral correlation matrix r is of the form:

$$r = \begin{bmatrix} 1 & \alpha & \alpha & \alpha^2 \\ \alpha & 1 & 1 & \alpha \\ \alpha & 1 & 1 & \alpha \\ \alpha^2 & \alpha & \alpha & 1 \end{bmatrix}. \tag{4.8}$$

By treating the two greens at different sampling locations as two color channels, the matrix r formulated in Eq. (4.8) becomes a singular matrix. An extra regularization step is required to deal with this problem in the Wiener reconstruction.

The spatial autocorrelation matrix R contains the coefficients of the autocorrelation function as in the grayscale case. We assume that the spatial autocorrelation follows the same decaying exponential function and use this model to construct it. The elements of the spatial correlation matrix R are defined by Eq. (3.14) as in Sec. 3.3. The parameters of the

generic model can be estimated from the subsampled green channel of the initially captured CFA image.

4.1.3 Fast Implementation of Multichannel Wiener Filter

The direct implementation of the multichannel Wiener filter defined in Eq. (4.5) requires an inversion of the $N \times N$ matrix $(DHR_fH^TD^T + DH_aR_{f_a}H_a^TD^T + R_u)$, which involves a huge amount of computational effort even for a small image. A possible diagonalization or sparse transformation of this matrix is desired. Because the Fourier transform diagonalizes the circulant block R, we can take advantage of the Fast Fourier Transform (FFT) algorithm and solve the linear equations in the spatial-frequency domain. Define two transformation matrices $\mathcal{F} \in \mathbb{R}^{N\times N}$ and $\bar{\mathcal{F}} \in \mathbb{R}^{4N\times 4N}$ with the forms $\mathcal{F} = \text{diag}(\mathcal{F}_s, \mathcal{F}_s, \mathcal{F}_s, \mathcal{F}_s)$ and $\bar{\mathcal{F}} = \text{diag}(\mathcal{F}_b, \mathcal{F}_b, \mathcal{F}_b, \mathcal{F}_b)$, where blocks $\mathcal{F}_s \in \mathbb{R}^{N/4\times N/4}$ and $\mathcal{F}_b \in \mathbb{R}^{N\times N}$ are 2D DFT matrices. The definition of the 2D DFT matrix is given in Appendix A. Since the DFT is unitary, we have $\mathcal{F}\mathcal{F}^H = I$ and $\bar{\mathcal{F}}\bar{\mathcal{F}}^H = I$, where the superscript H represents the Hermitian transpose operation. Applying matrix identities to Eq. (4.5), one can express the spatial-frequency domain representation of the multichannel Wiener filter as follows:

$$W = R_fH^TD^T\mathcal{F}^H\left[\mathcal{F}D\bar{\mathcal{F}}^H\bar{S}\bar{\mathcal{F}}D^T\mathcal{F}^H + \mathcal{F}D\bar{\mathcal{F}}^H\bar{S}_a\bar{\mathcal{F}}D^T\mathcal{F}^H + S_u\right]^{-1}\mathcal{F} \tag{4.9}$$

The matrices $\bar{S} = \bar{\mathcal{F}}HR_fH^T\bar{\mathcal{F}}^H$, $\bar{S}_a = \bar{\mathcal{F}}HR_{f_a}H^T\bar{\mathcal{F}}^H$ and $S_u = \mathcal{F}R_u\mathcal{F}^H$ are the filtered power spectra of the baseband image and aliasing component and the noise spectrum, respectively. It is worth noting that $\bar{S}$ and $\bar{S}_a$ are power spectrum only in the spatial-frequency domain. In the white Gaussian noise or small dependent-noise case, we can approximate the noise power spectrum with $S_u \approx N\sigma^2 I_N$, where σ is the standard deviation of the additive noise and I_N is the identity matrix. Because the matrices $\mathcal{F}D\bar{\mathcal{F}}^H\bar{S}\bar{\mathcal{F}}D^T\mathcal{F}^H$ and $\mathcal{F}D\bar{\mathcal{F}}^H\bar{S}_a\bar{\mathcal{F}}D^T\mathcal{F}^H$ have identical structure, we only present the fast implementation method for the first matrix here and the other can be treated the same way.

Similar to the autocorrelation matrix defined in Eq. (4.8), one can decouple the power spectrum matrix $\bar{S}$ to the spatial spectrum S and the spectral correlation matrix r with a Kronecker product:

$$\bar{S} = r \otimes S \tag{4.10}$$

where S is a diagonal matrix that captures the spatial power spectrum. Let $\bar{K}$ denote the matrix $\mathcal{F}D\bar{\mathcal{F}}^H\bar{S}\bar{\mathcal{F}}D^T\mathcal{F}^H$. We can again isolate the spectral autocorrelation matrix from $\bar{K}$:

$$\bar{K} = r \otimes K. \tag{4.11}$$

The matrix K describes the spectrum overlaps introduced by the Bayer CFA sampling and has the following structure:

$$K = \begin{bmatrix} K_{rr} & K_{rg_1} & K_{rg_2} & K_{rb} \\ K_{g_1r} & K_{g_1g_1} & K_{g_1g_2} & K_{g_1b} \\ K_{g_2r} & K_{g_2g_1} & K_{g_2g_2} & K_{g_2b} \\ K_{br} & K_{bg_1} & K_{bg_2} & K_{bb} \end{bmatrix} \tag{4.12}$$

where $K_{ij} = \mathcal{F}_S D_i \mathcal{F}_N^H S \mathcal{F}_N D_j^T \mathcal{F}_S^H$ $(i, j \in \{r, g_1, g_2, b\})$. The matrix K has a great deal of symmetry. Particularly, we have the following identities: $K_{rr} = K_{g_1g_1} = K_{g_2g_2} = K_{bb}$, $K_{rg_1} = K_{g_1r}^H$, $K_{rg_2} = K_{g_2r}^H$, $K_{rb} = K_{br}^H$, $K_{g_1g_2} = K_{g_2g_1}^H$, $K_{g_1b} = K_{bg_1}^H$, $K_{g_2b} = K_{bg_2}^H$, $K_{rg_1} = K_{g_2b}$, $K_{g_1r} = K_{bg_2}$, $K_{rg_2} = K_{g_1b}$, and $K_{g_2r} = K_{bg_1}$. As expected, each block K_{ij} of matrix K is a diagonal matrix. The details are presented in Appendix B.

We intend to explore the sparsity of matrix $\bar{K}$ to reduce the computational cost of the proposed multichannel Wiener filter. For an appropriately defined permutation matrix $P \in \mathbb{R}^{N\times N}$, one can transform the block matrix $\bar{K}$ with diagonal blocks to a block-diagonal matrix Q as follows:

$$Q = P\bar{K}P^{-1} = \text{diag}(Q_1, Q_1, \ldots, Q_{\frac{N}{4}}) \tag{4.13}$$

Each block Q_i ($i = 1, 2, \cdots, \frac{N}{4}$) is a 4×4 matrix. The matrix inversion of the matrix $\bar{K}$ can be implemented as,

$$\bar{K}^{-1} = P^{-1} Q^{-1} P \tag{4.14}$$

where $Q^{-1} = \text{diag}(Q_1^{-1}, Q_2^{-1}, \cdots, Q_{\frac{N}{4}}^{-1})$. As a result, we transform an $N \times N$ matrix inversion into $\frac{N}{4}$ 4×4 matrix inversions. The computational complexity is reduced from $O(N^3)$ to $O(N)$.

4.2 Problem Formulation in LC_1C_2 Domain

One major concern of formulating the color acquisition in the RGB domain is the accuracy of modeling the spectral correlations among channels. We presented a simple 4×4 matrix to capture such information in the previous section. The Wiener filter built on this model is significantly simplified using this procedure. But this RGB model cannot precisely represent the various spectral correlations of different scenes. A more complicated model could improve the reconstruction results but involves more computational effort. To avoid the dilemma in the RGB domain, we introduce a color imaging model in the LC_1C_2 domain which not only brings down the magnitude of cross-channel correlations but simplifies the implementation as well.

4.2.1 Frequency-Domain Representation of Bayer CFA Image

Let us consider an $m_0 \times n_0$ Bayer CFA image y and the $m_0 \times n_0 \times 3$ true image with three channels f_r, f_g and f_b. The CFA image y can be described as a sum of three subsampled images $\bar{f}_r$, $\bar{f}_g$ and $\bar{f}_b$ as shown in Fig. 4.2. If we denote (m, n) as pixel coordinates and set the origin at the upper-left corner of the images, the CFA image can be mathematically expressed as follows [57]:

$$y(m, n) = \bar{f}_r(m, n) + \bar{f}_g(m, n) + \bar{f}_b(m, n) \tag{4.15}$$

where the subsampled images $\bar{f}_r$, $\bar{f}_g$ and $\bar{f}_b$ are given by:

$$\begin{aligned}
\bar{f}_r(m,n) &= 0.25 f_r(m,n)(1+(-1)^m)(1-(-1)^n) \\
\bar{f}_g(m,n) &= 0.50 f_g(m,n)(1+(-1)^{m+n}) \\
\bar{f}_b(m,n) &= 0.25 f_b(m,n)(1-(-1)^m)(1+(-1)^n)
\end{aligned} \tag{4.16}$$

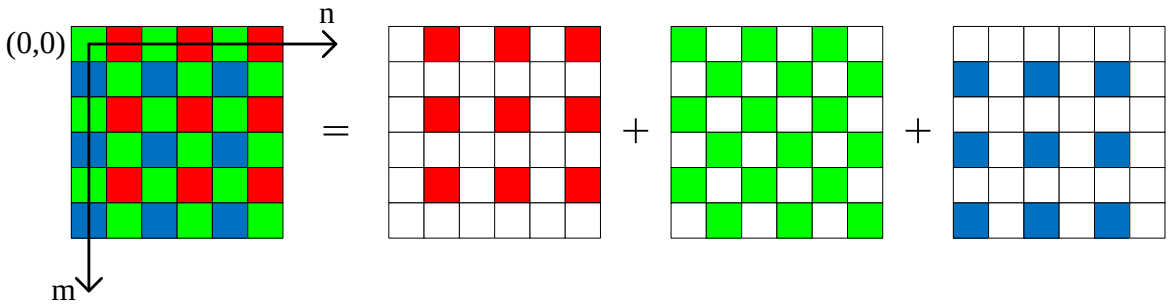

Figure 4.2: Bayer CFA and three subsampled images.

To acquire the frequency-domain representation of a CFA image, Eq. (4.15) can be further written as follows:

$$y(m,n) = f_L(m,n) + f_{C_1}(m,n)(-1)^{m+n} - f_{C_2}(m,n)(-1)^m + f_{C_2}(m,n)(-1)^n \tag{4.17}$$

where f_L is the luminance channel of the true color image. The terms f_{C_1} and f_{C_2} represent the two chrominance channels. In fact, L, C_1 and C_2 are three components of a new color space. The linear transform between RGB and LC_1C_2 is given by:

$$\begin{bmatrix} f_L \\ f_{C_1} \\ f_{C_2} \end{bmatrix} = \begin{bmatrix} 0.25 & 0.5 & 0.25 \\ -0.25 & 0.5 & -0.25 \\ -0.25 & 0 & 0.25 \end{bmatrix} \begin{bmatrix} f_r \\ f_g \\ f_b \end{bmatrix} \tag{4.18}$$

The Fourier transform of Eq. (4.17) leads to the frequency-domain expression of a CFA image

$$F(\omega_m, \omega_n) = F_L(\omega_m, \omega_n) + F_{C_1}(\omega_m - \pi, \omega_n - \pi) - F_{C_2}(\omega_m - \pi, \omega_n) + F_{C_2}(\omega_m, \omega_n - \pi) \quad (4.19)$$

According to Eq. (4.19), a Bayer CFA image can be expressed as a luminance component F_L, one modulated chrominance component of F_{C_1} at frequency (π, π) and two modulated chrominance components of F_{C_2} at frequencies $(\pi, 0)$ and $(0, \pi)$.

4.2.2 LC_1C_2 Color Imaging Model

The color imaging model with consideration of blur and noise can be acquired similarly as Eq. (4.17). Using matrix-vector notation, the acquisition model with aliasing components in the LC_1C_2 domain is given by:

$$y = AHf + AH_a f_a + u \quad (4.20)$$

where $y \in \mathbb{R}^{N\times 1}$ is the degraded CFA image and the term $u \in \mathbb{R}^{N\times 1}$ represents additive noise. The baseband image f and aliasing component $f_a \in \mathbb{R}^{4N\times 1}$ have the forms $f = [{f_L}^T, {f_{C_1}^{mn}}^T, {f_{C_2}^{m}}^T, {f_{C_2}^{n}}^T]^T$ and $f_a = [{f_{aL}}^T, {f_{aC_1}^{mn}}^T, {f_{aC_2}^{m}}^T, {f_{aC_2}^{n}}^T]^T$, where the vectors f_i^j and f_{ai}^j, $i \in \{L, C_1, C_2\}$, $j \in \{mn, m, n\}$ are the luminance and chrominance images described in Eq. (4.17). Particularly, we have the following relations for the baseband images:

$$\begin{aligned} f_L &: f_L(m,n) \\ f_{C_1}^{mn} &: f_{C_1}(m,n)(-1)^{m+n} \\ f_{C_2}^{m} &: -f_{C_2}(m,n)(-1)^{m} \\ f_{C_2}^{n} &: f_{C_2}(m,n)(-1)^{n} \end{aligned} \quad (4.21)$$

The aliasing components have similar relations. The block matrices A have the form $A = [I_N, I_N, I_N, I_N]$, where I_N is the identity matrix.

The matrices $H = \text{diag}(H, H^{mn}, H^m, H^n)$ and $H_a = \text{diag}(H_a, H_a^{mn}, H_a^m, H_a^n)$ are two block diagonal matrices which contain the baseband PSF and stopband PSF of the out-of-focus blur for all the channels. Each block represents the PSF of the blur for the corresponding channel. Since the chrominance channels are modulated, the blurs for the chrominance channels have the same kind of modulation. In particular, H^{mn} and H_a^{mn} are modulated to (π, π), H^m and H_a^m are modulated to $(\pi, 0)$, and H^m and H_a^m are modulated to $(0, \pi)$. Fig. 4.3. An imaging model in the frequency domain can be obtained by taking a Fourier transform of Eq. (4.20), which has the following form:

$$Y = \mathcal{A}\mathcal{H}F + \mathcal{A}\mathcal{H}_a F_a + U \tag{4.22}$$

where the terms $\mathcal{A}$, $\mathcal{H}$, $\mathcal{H}_a$, F, F_a and U are the corresponding Fourier transforms of terms in Eq. (4.20).

To simplify the imaging model, we assume that the PSF of the out-of-focus blur generated by the camera lens is identical in different color channels. Under this assumption, H, H^{mn}, H^m and H^n have the same responses except the center frequencies. The same relationship exists for the stopband responses of the blur. The simulation results in Chapter 3 show that the signal-dependent noise has little impact on the choice of focus setting. Rather than choosing a similar noise model here as in the grayscale case, a white Gaussian noise model is selected for the color acquisition.

4.2.3 Multichannel Wiener Filter in LC_1C_2 Domain

A similar procedure as we used in Sec. 4.1.2 is applied here to derive the multichannel Wiener filter in the LC_1C_2 domain. Assuming that the signal and noise are wide-sense stationary, and applying the imaging model Eq. (4.20) on the Wiener filter definition Eq. (4.3),

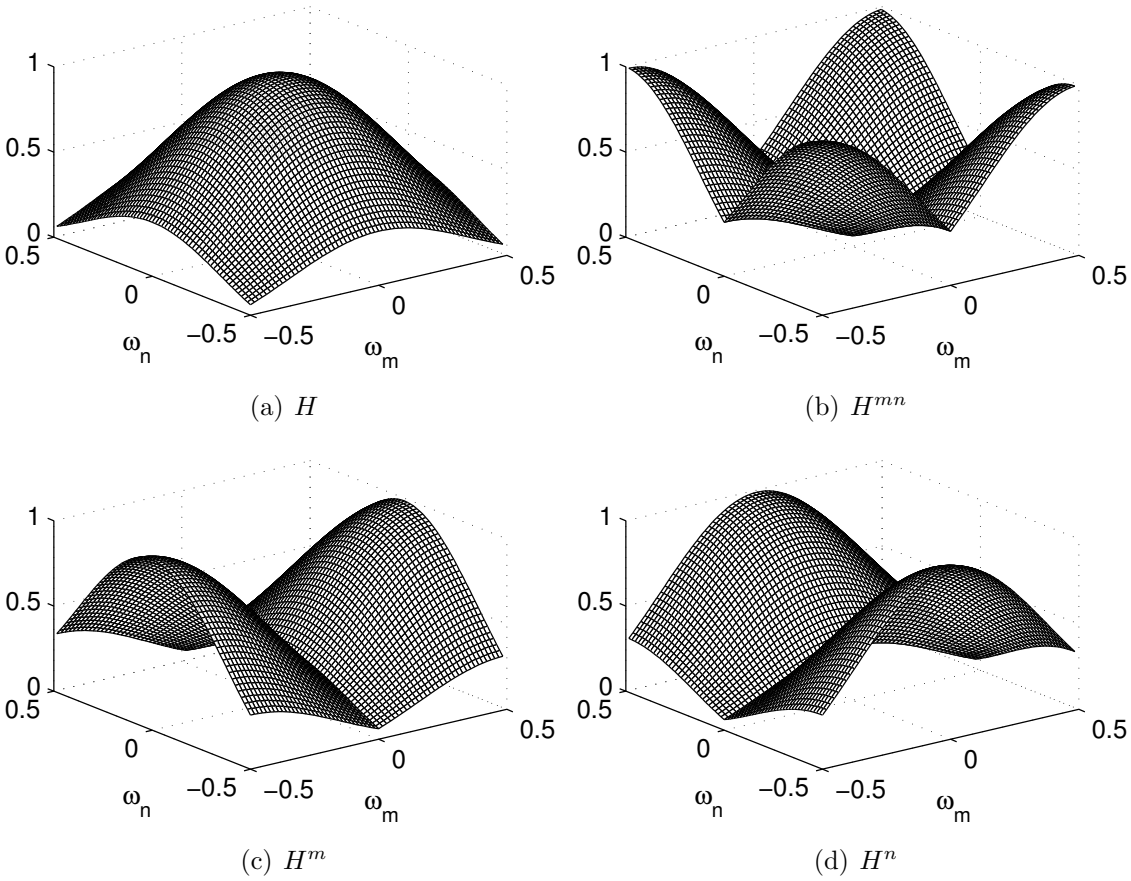

(a) H (b) H^{mn}

(c) H^{m} (d) H^{n}

Figure 4.3: Four baseband responses of out-of-focus blur at blur radius $r = 1.5$ pixels. The horizontal and vertical frequencies have been normalized by the sampling frequency.

the Wiener filter W in the modulated $\mathrm{LC_1C_2}$ domain is given by:

$$W = R_f H^T A^T \left(AHR_f H^T A^T + AH_a R_{f_a} H_a^T A^T + R_u \right)^{-1} \tag{4.23}$$

The cross-correlations among the baseband image f, aliasing component f_a and noise u are set to zero in Eq. (4.23) under the assumption that they are uncorrelated with each other; that is, $R_{ff_a} = R_{fu} = R_{f_af} = R_{f_au} = R_{uf} = R_{uf_a} = 0$.

Unlike the autocorrelation matrices in the Wiener filter formulated in RGB domain, R_f and $R_{f_a} \in \mathbb{R}^{4N \times 4N}$ here are diagonal matrices rather than block diagonal matrices. In the RGB formulation, since the color channels of scenes are highly correlated, the cross-correlation cannot be ignored. A 4×4 matrix is chosen to model the cross-correlation

in that case. However, the correlation among luminance and two chrominance channels is reduced because chrominance channels essentially are differences among RGB channels. In fact, by defining the Wiener filter on the luminance and modulated chrominance channels, the cross-correlations are reduced even further. This is true for both baseband images and aliasing components.

The cross-correlations among RGB, LC_1C_2 and modulated LC_1C_2 channels of a typical color image are depicted in Fig. 4.4. The mean values of RGB channels of the image were subtracted to ensure the cross-correlations are at the same level. The magnitude of cross-correlations in the LC_1C_2 domain is 20 times smaller than the values of cross-correlations in the RGB domain. If two chrominance channels C_1 and C_2 are modulated to (π, π) and $(\pi, 0)$ or $(0, \pi)$, on which the Wiener filter is modeled, the cross-channel correlations are reduced 4000 times. It is reasonable to assume these channels are uncorrelated with each other.

Since the prior information of the input scene is unknown, a similar strategy to the grayscale case must be chosen to estimate the autocorrelation matrix R_f and R_{f_a}. During the simulation, we found that the FFT algorithm generated edge artifacts when transforming autocorrelation functions to power spectra. This effect has a negative impact on the Wiener filter due to the modulation of C_1 and C_2 channels. Particularly, the edge artifacts with the high-frequency characteristic of the C_1 and C_2 channels are modulated to the low-frequency locations, which affects the power spectrum of the luminance component. To avoid this problem, rather than modeling the autocorrelation, we estimate the power spectra of L, C_1 and C_2 channels directly.

The frequency expression of the multichannel Wiener can be derived by taking a Fourier transform of Eq. (4.23):

$$\mathcal{W} = S_f \mathcal{H}^H \mathcal{A}^H \left(\mathcal{A}\mathcal{H} S_f \mathcal{H}^H \mathcal{A}^H + \mathcal{A}\mathcal{H}_a S_{f_a} \mathcal{H}_a^H \mathcal{A}^H + S_u \right)^{-1} \tag{4.24}$$

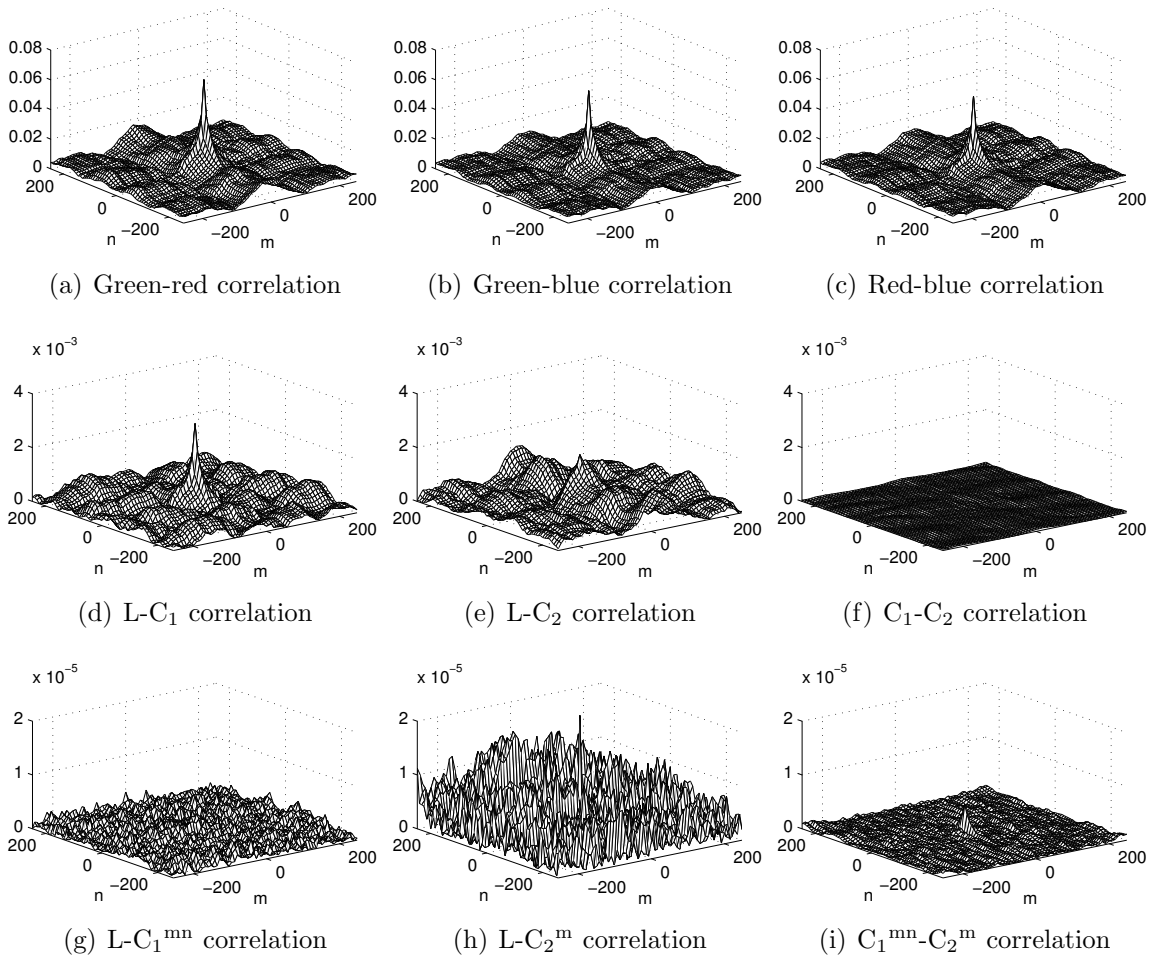

(a) Green-red correlation (b) Green-blue correlation (c) Red-blue correlation

(d) L-C_1 correlation (e) L-C_2 correlation (f) C_1-C_2 correlation

(g) L-$C_1{}^{mn}$ correlation (h) L-$C_2{}^{m}$ correlation (i) $C_1{}^{mn}$-$C_2{}^{m}$ correlation

Figure 4.4: The absolute magnitude of cross-channel correlations in RGB, LC_1C_2 and modulated LC_1C_2 domain for one color scene. Note the different vertical scales on each row of the figure.

The diagonal matrices S_f, S_{f_a} and S_u are power spectra of the baseband image, aliasing component and noise. Here, the "H" superscript represents the Hermitian transpose operation.

The unknown power spectrum S_f contains the baseband power spectrum S_{f_L} for the luminance channel and three baseband spectra $S_{f_{C_1}^{mn}}$, $S_{f_{C_2}^{m}}$ and $S_{f_{C_2}^{n}}$ for the modulated chrominance channels. The spectra of the aliasing components of corresponding channels are recorded in the matrix S_f. To estimate S_f and S_{f_a}, we use a similar method to the one in the grayscale case. A CFA image Y_0 is initially captured with a large amount of out-of-focus

blur $\mathcal{H}_0$ and described as follows:

$$Y_0 \approx \mathcal{A}\mathcal{H}_0 F + U \tag{4.25}$$

By assuming that the aliasing component F_a is sufficiently suppressed in this image, we ignore it in the above equation. In order to estimate the power spectra, the blurred initial full-color image has to be recovered first by a state-of-art demosaicking method, such as:

$$F_{H_0} = \mathcal{M} Y_0 \tag{4.26}$$

where the term $\mathcal{M}$ represents a demosaicking operation. The corresponding image $\bar{F}_{H_0}$ in the $\mathrm{LC_1C_2}$ domain can be obtained by transforming F_{H_0} using the relation defined in Eq. (4.18). Since $\mathcal{H}_0$ is a diagonal matrix, the expected power spectrum of the initial baseband image S_{f_0} can be derived by the inverse filtering method:

$$S_{f_0} \approx \frac{S_{f_{H_0}} - \sigma_u^2}{|\mathcal{H}_0|^2} \tag{4.27}$$

Using the periodogram estimate $\hat{S}_{f_{H_0}} = |\bar{F}_{H_0}|^2$, we obtain:

$$\hat{S}_{f_0} = \frac{|\bar{F}_{H_0}|^2 - \sigma_u^2}{|\mathcal{H}_0|^2} \tag{4.28}$$

An isotropic autocorrelation model is chosen here to formulate the power spectral model for images [76], which is given by:

$$R_f(\tau_x, \tau_y) = e^{-\alpha\sqrt{\tau_x^2 + \tau_y^2}} \tag{4.29}$$

where the parameter $\alpha > 0$ defines the decay rate. The autocorrelation function and the power spectral density form a Fourier transform pair. By taking a Fourier transform of

Eq. (4.29), we have the power spectral density model for images as follows:

$$S(\Omega_x, \Omega_y) = 2\pi c\alpha(\alpha^2 + \Omega_x^2 + \Omega_y^2)^{-3/2} \tag{4.30}$$

where c is a scale factor.

To estimate the power spectra of baseband image and aliasing components, we assume that there exists a positive integer R which satisfies $\Omega_{f_{max}} < \min\{R\frac{\pi}{\Delta_x}, R\frac{\pi}{\Delta_y}\}$, where $\Omega_{f_{max}}$ is the highest frequency content in the continuous scene. In other words, if the sampling frequency of the camera is increased by a factor of R, no aliasing is introduced by the sampling. The parameters c and α in Eq. (4.30) can be estimated by fitting the result of Eq. (4.28) in the generic power spectral density model. As the same time, we can change the sampling frequency to obtain the estimated power spectra $\bar{S}_{f_L}$, $\bar{S}_{f_{C_1}}$ and $\bar{S}_{f_{C_2}}$ of L, C_1 and C_2 channels. The spectra of baseband and aliasing components can be separated according to the ratio of sampling frequency R. The estimated spectra $\bar{S}_{f_{C_1}^{mn}}$, $\bar{S}_{f_{C_2}^{m}}$ and $\bar{S}_{f_{C_2}^{n}}$ can be acquired by applying the modulation defined in Eq.(4.21).

An estimated spectrum along with the actual spectrum of the luminance channel for one test scene is shown in Fig. 4.5 in log-magnitude. The statistics of the original scene were captured by the power spectral density model. Advanced power spectral density models could be used for a more accurate estimate. Since the topic is beyond the scope of this dissertation and this model performs adequately, other power spectral density models for images are not covered here.

4.3 Error Criterion

In Sec. 3.4, we derived an error criterion to enable the camera to find the optimal defocus setting for a particular scene. A similar criterion is introduced here for adaptive defocus color imaging. We start by analyzing of the true reconstruction error by Wiener filtering in the

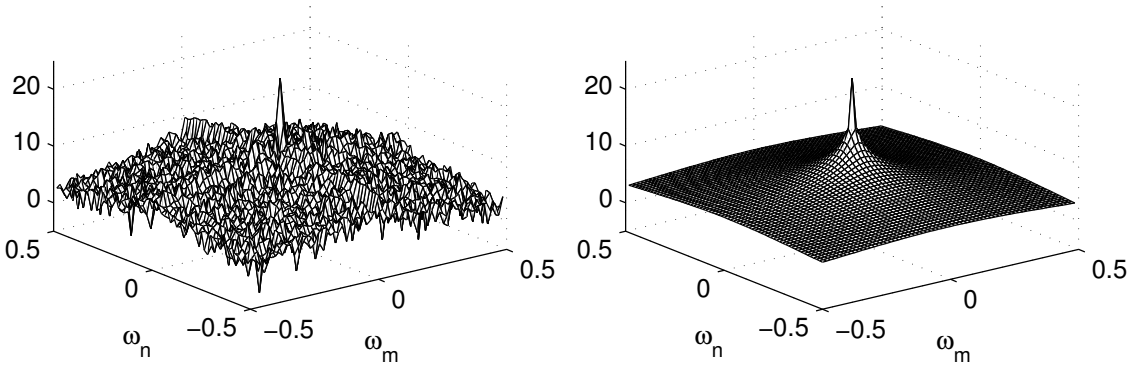

(a) True power spectral density (b) Estimated power spectral density

Figure 4.5: The true power spectral density and the estimated power spectral density of one test scene.

frequency domain, which is given by:

$$\epsilon^2 = E\{\|F - \hat{F}\|^2\} \tag{4.31}$$

where the vector $\hat{F}$ is the estimated baseband image by Wiener filtering: $\hat{F} = WY$. Applying the imaging model Eq. (4.22), one can describe the reconstruction error ϵ^2 further by:

$$\begin{aligned}
\epsilon^2 &= E\{\|F - \mathcal{W}\mathcal{A}\mathcal{H}F - \mathcal{W}\mathcal{A}\mathcal{H}_a F_a - \mathcal{W}U\|^2\} \\
&= E\{(F - \mathcal{W}\mathcal{A}\mathcal{H}F - \mathcal{W}\mathcal{A}\mathcal{H}_a F_a - \mathcal{W}U)(F - \mathcal{W}\mathcal{A}\mathcal{H}F - \mathcal{W}\mathcal{A}\mathcal{H}_a F_a - \mathcal{W}U)^H\} \\
&= \mathrm{tr}\left\{S_f - S_f\mathcal{H}^H\mathcal{A}^H\mathcal{W}^H - \mathcal{W}\mathcal{A}\mathcal{H}S_f \right. \\
&\quad \left. + \mathcal{W}[\mathcal{A}\mathcal{H}S_f\mathcal{H}^H\mathcal{A}^H + \mathcal{A}\mathcal{H}_a S_{f_a}\mathcal{H}_a^H\mathcal{A}^H + S_u]W^H\right\}
\end{aligned} \tag{4.32}$$

Assume that the estimated power spectrum matrices $\bar{S}_f$ and $\bar{S}_{f_a}$ in the Wiener filter are approximately equal to the true power spectra; that is, $\bar{S}_f \approx S_f$ and $\bar{S}_{f_a} \approx S_{f_a}$. Then the estimated reconstruction error can be simplified by applying the Wiener filter expression Eq. (4.24) in the above equation:

$$\begin{aligned}
\hat{\epsilon}^2 \approx& \mathrm{tr}\left\{S_f - S_f\mathcal{H}^H\mathcal{A}^H\mathcal{W}^H - \mathcal{W}\mathcal{A}\mathcal{H}S_f + S_f\mathcal{H}^H\mathcal{A}^H\mathcal{W}^H\right\} \\
=& \mathrm{tr}\left\{S_f - \mathcal{W}\mathcal{A}\mathcal{H}S_f\right\}
\end{aligned} \tag{4.33}$$

Originally, we chose the initially estimated power spectrum $\hat{S}_{f_0}$ defined in Eq. (4.28) to approximate the true power spectrum S_f, but the estimated reconstruction error were not accurate enough. The error criterion can be improved by changing $\hat{S}_{f_0}$ to the power spectrum $\bar{S}_f$ estimated by the generic model, which is given by:

$$\hat{\epsilon}^2 \approx \mathrm{tr}\left\{\bar{S}_f - \mathcal{W}\mathcal{A}\mathcal{H}\bar{S}_f\right\} \tag{4.34}$$

Fig. 4.6 depicts the true and estimated reconstruction errors vs. the PSF radius for two test scenes. It is evident that our criterion tracks the true optimal defocus setting as expected.

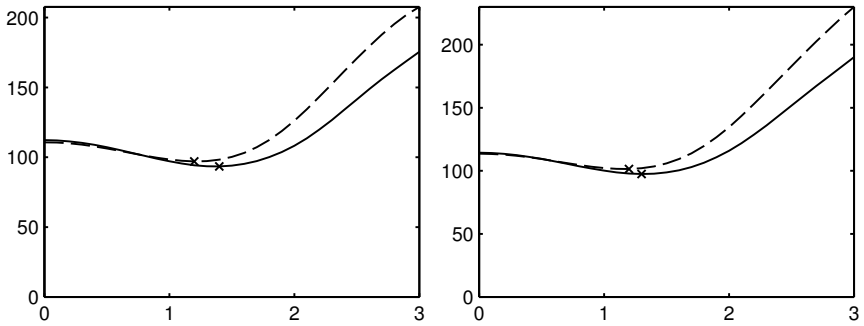

(a) Scene No. 8, $\sigma = 1$

(b) Scene No. 8, $\sigma = 2$

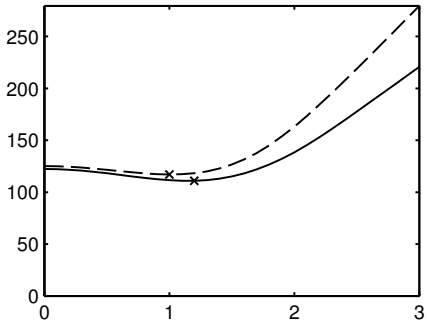

(c) Scene No. 8, $\sigma = 4$

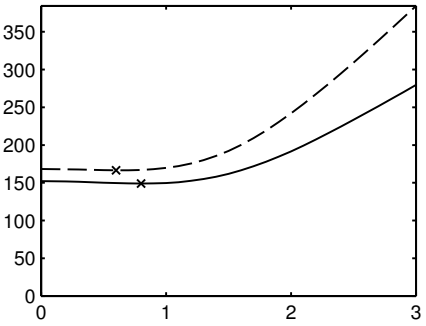

(d) Scene No. 8, $\sigma = 8$

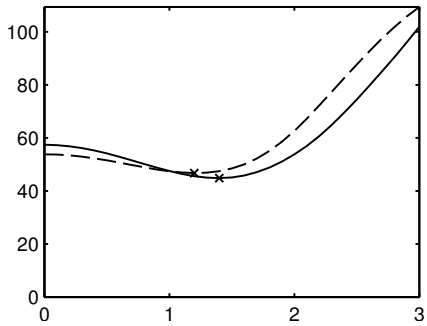

(e) Scene No. 19, $\sigma = 1$

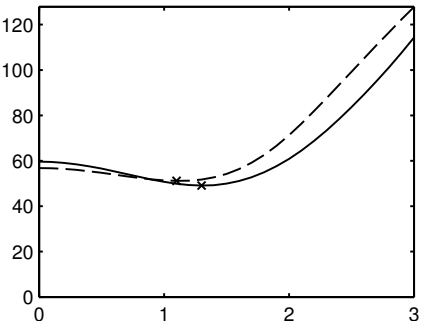

(f) Scene No. 19, $\sigma = 2$

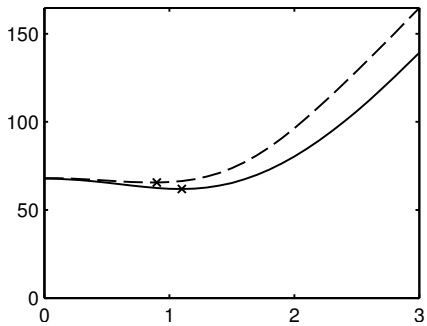

(g) Scene No. 19, $\sigma = 4$

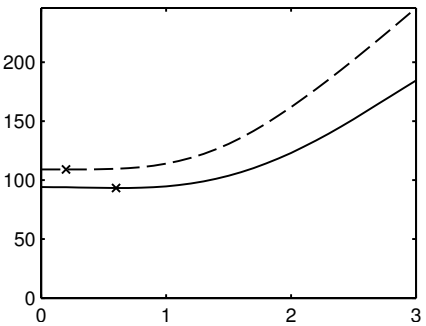

(h) Scene No. 19, $\sigma = 8$

Figure 4.6: Comparison of the true (—) and estimated (– –) reconstruction errors ϵ^2 (vertical axis) vs. the PSF radius r (horizontal axis) for different noise levels. The true and estimated optimal blur radii were labeled by "×".

4.4 Joint Deblurring and Demosaicking

The image captured with the "optimal" defocus setting is a Bayer CFA image degraded by the out-of-focus blur and noise. We present an iterative approach to recover a full-color image from a blurred CFA acquisition [77]. The CFA image with known blur is first reconstructed by a state-of-the-art demosaicking algorithm. In each iteration, we recover a full-color estimate using a least-squares regularization approach. The iterative restoration is implemented by a steepest descent method, and the residue of each iteration is used for our stopping criterion.

The underlying true-color image g is acquired with blur H and additive noise u

$$g = Hf + u \tag{4.35}$$

The CFA image y and the true-color image g have the relation:

$$y = Dg \tag{4.36}$$

where D is the Bayer CFA sampling matrix. The aliasing component is omitted here for simplification. Define a least-squares function

$$J = \|g - Hf\|^2 + \lambda \|Lf\|^2 \tag{4.37}$$

where $\|\cdot\|$ represents the l_2 norm, λ is the regularization coefficient and L is a highpass filter. The constrained least-squares estimate $\hat{f}$ minimizes the above equation:

$$\hat{f} = \underset{\hat{f}}{\operatorname{argmin}} \left\{ \|g - Hf\|^2 + \lambda \|Lf\|^2 \right\} \tag{4.38}$$

The most common choice of L is a discrete Laplacian kernel, which has the following form:

$$L = \begin{bmatrix} 0 & 1 & 0 \\ 1 & -4 & 1 \\ 0 & 1 & 0 \end{bmatrix} \tag{4.39}$$

The first term in (4.37) is normally called the data fidelity term, and the second term forces the smoothness of the solution. The regularization coefficient λ controls the degree of the penalty and is expected to be small. The choice of the optimal λ for different blur and noise is beyond the scope of this dissertation. In the simulation, λ is chosen to be a constant, and we determine its value by trial-and-error while monitoring the reconstruction errors of the result images.

To implement the least-squares algorithm using the steepest descent method, one can compute the gradient of J as follows:

$$\begin{aligned} \nabla J =& \frac{d}{df}\left(\|g - Hf\|^2 + \lambda\|Lf\|^2\right) \\ =& -2H^T(g - Hf) + 2\lambda L^T Lf \end{aligned} \tag{4.40}$$

The estimate of the full-color image $\hat{f}_k$ at kth iteration is:

$$\begin{aligned} \hat{f}_k =& \hat{f}_{k-1} - \nabla J_{k-1} \\ =& \hat{f}_{k-1} + 2H^T(\hat{g}_0 - H\hat{f}_{k-1}) - 2\lambda L^T L\hat{f}_{k-1} \end{aligned} \tag{4.41}$$

where $\hat{f}_{k-1}$ is the previous estimate. To combine the steepest descent method with a nonlinear demosaicking algorithm $\mathcal{M}$, one can embed it inside each iteration to update the current estimate $\hat{f}_k$:

$$\begin{aligned} \hat{y}_k &= D\hat{f}_k \\ \hat{f}_k &= \mathcal{M}(\hat{y}_k) \end{aligned} \tag{4.42}$$

and the initial estimate is:

$$\hat{f}_0 = \mathcal{M}(y). \tag{4.43}$$

In particular, with the prior knowledge of the blur H and noise u and the input CFA image y, the joint deblurring and demosaicking approach can be described by the following pseudo-code:

$\hat{g}_0 = \mathcal{M}(y)$, $\hat{f}_0 = \mathcal{M}(y)$ and set H, L, α and ϵ.
for $k = 1$ to K **do**
Gradient: $G_{k-1} = -2H^T(\hat{g}_0 - H\hat{f}_{k-1}) + 2\lambda L^T L\hat{f}_{k-1}$;
Descent direction: $\hat{f}_k = \hat{f}_{k-1} - G_{k-1}$;
if $\|G_{k-1}\| > \epsilon$ **then**
Subsampling: $\hat{y}_k = D\hat{f}_k$;
Demosaicking: $\hat{f}_k = \mathcal{M}(\hat{y}_k)$;
else
Stop and claim $\hat{f}_k$ is the final estimate;
end if
end for

4.5 Simulation and Results

We present some experimental results to verify the color defocusing acquisition and evaluate the error criterion we introduced in Sec. 4.3. The image library contains the following four databases. Images No. 1–24 are the twenty-four test images from the Kodak PhotoCD set [71]. They were cropped to size 512×512. Images No. 25–54 are the thirty original test images from the content-based strategies of image quality (CSIQ) database [72]. Images No. 55–64 are from the image and video-communication (IVC) database for subjective quality assessment [73]. The remaining thirty-six images were taken by a Nikon D90 digital

single-lens reflex (DSLR) camera and cropped to size 512×512. The intensity values of these natural images are between 0 and 255. Each image was subsampled by a factor of R in both directions to model the sampling processing.

We conducted simulation experiments as follows. The downsampling rate R was set to 2. The baseband image for each scene was calculated using an ideal lowpass filter on each color channel then subsampled by a factor of R in both directions. Three acquisition methods were chosen in our experiments: acquisition without an anti-aliasing filter, acquisition with an anti-aliasing filter and defocussing acquisition. A 2×2 averaging filter was applied first in the "continuous" domain to simulate the sensor-size effect for all acquisition methods.

Each channel of the scene was subsampled a factor of R then sampled again with a Bayer CFA to simulate the acquisition method without an anti-aliasing filter. For the acquisition method with an anti-aliasing filter, each channel was subsampled a factor of R and then filtered with a 2×2 averaging filter in the "discrete" domain to simulate the anti-aliasing filter. It is worth mentioning that the sensor-size effect filter and the anti-aliasing filter were applied in different domains. The former one was applied before the sampling, while the latter one was used after the sampling. After the anti-aliasing step, the full-color images were sampled according to the Bayer pattern to generate a CFA image.

For the defocussing acquisition, an out-of-focus blur with radius r was applied in the "continuous" domain along with the sensor-size effect. The resulting full-color images were subsampled by a factor of R followed by a Bayer CFA sampling. Since the PSF of out-of-focus blur is close to circular [75], we implemented out-of-focus blur using a circular blur with different radii r. The initial CFA image y_0 was acquired using blur with $r = 1.5$ pixels then demosaicked by the method proposed in [57]. The out-of-focus blur that generates the minimum of the estimated reconstruction error $\hat{\epsilon}^2$ is the estimated optimal defocus setting.

The demosaicking method we chose for the acquisition methods with and without an anti-aliasing filter is the adaptive frequency-domain method introduced by Dubois [57]. The joint deblurring and demosaicking approach described in Sec. 4.4 was selected to recover the

true-color image for defocusing acquisition. The same demosaicking algorithm was embedded in the joint approach for a fair comparison with the traditional acquisition methods. Each resulting image acquired by different approaches was evaluated by comparing it to the base-band image. The numerical evaluation was accomplished by calculating the three-channel peak-signal-to-noise ratio PSNR_3 for each method. The PSNR_3 is defined by:

$$\mathrm{PSNR}_3 = -10 \log_{10} \left[\frac{1}{255^2 \times N} \sum_{i=1}^{N} \left(f_i - \hat{f}_i \right)^2 \right] \tag{4.44}$$

where f_i and $\hat{f}_i$, $i \in \{R, G, B\}$ are the color channels of the baseband image and the estimated image.

We first compared the optimal radius estimated using the error criterion formulated in Sec. 4.3 with the true optimal radius for different scenes and noise levels. The radius error is defined by:

$$\Delta r = \hat{r}_{opt} - r_{opt} \tag{4.45}$$

where r_{opt} and $\hat{r}$ are true and estimated blur radii. The average radius error $\overline{\Delta r}$ over 100 test scenes in Table 4.1 is close to zero, which indicates there is no significant bias created by the error criterion. The average absolute radius error $\overline{|\Delta r|}$ is less than 0.25 pixels. The average percentage of PSNR loss $\overline{\Delta \mathrm{PSNR}_3}$ caused by the inaccurate radius estimation is less than 0.25%.

Table 4.1: Evaluations of the criteria over 100 test scenes with noise levels σ = 8, 4, 2, 1. The unit of the radius difference $\overline{\Delta r}$ and the mean absolute difference $\overline{|\Delta r|}$ is pixels.

σ	$\overline{\lvert\Delta r\rvert}$	$\overline{\Delta r}$	$\overline{\Delta \mathrm{PSNR}_3}$ %
8	0.16	-0.057	0.24
4	0.24	0.032	0.16
2	0.16	-0.055	0.14
1	0.16	-0.095	0.04

The histogram plots shown in Fig. 4.7 demonstrate that the error criterion is robust with respect to various noise levels. For most test scenes, the absolute blur radius errors are

smaller than 0.3 pixel. The accuracy of the error criterion could be improved if an anisotropic or more advanced power spectral density model were chosen in Sec. 4.2.3.

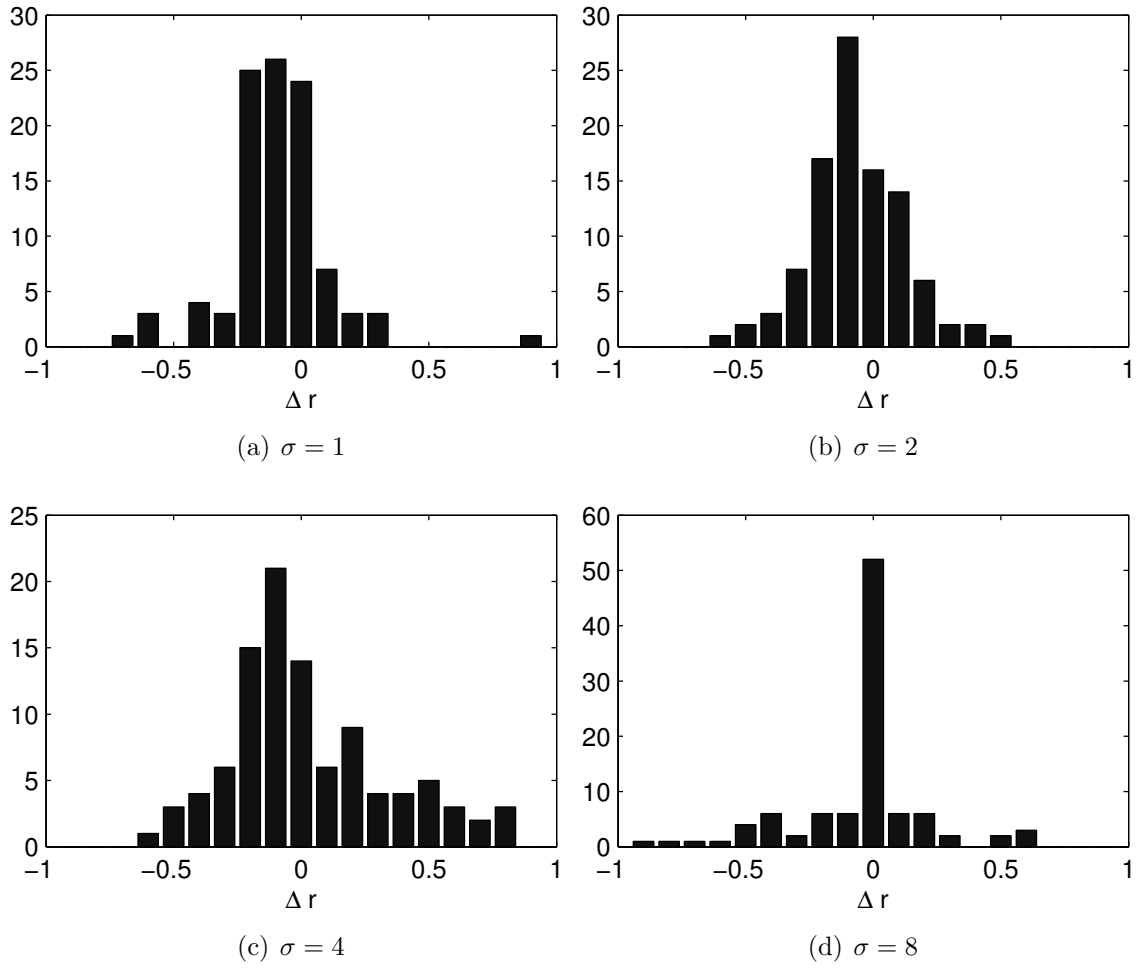

Figure 4.7: Histogram plots of blur radius error at various noise levels.

The result images acquired by different methods of No. 56 test scene (Barbara) are shown in Fig. 4.8. The CFA image captured by each method was corrupted by white Gaussian noise with standard deviation $\sigma = 1$. The Moiré patterns on the pants were largely reduced by the defocusing approach. Although the aliasing artifacts in the image acquired by the four-spot birefringent filter have been greatly reduced, the edges are blurrier than the image acquired by the defocusing method. The result color image reconstructed from the CFA image acquired without an anti-aliasing filter has sharp edges but severe artifacts.

(a) Baseband image

(b) w/o Anti-aliasing

(c) w Anti-aliasing

(d) Defocusing acquisition

Figure 4.8: Result images acquired from No. 56 scene by three different methods. The standard deviation of additive noise $\sigma = 1$.

A portion of reconstructed full-color images along with the baseband image of test scene No. 1 are presented in Fig. 4.9. White Gaussian noise with standard deviation $\sigma = 2$ was added in all the acquired CFA images. The full-color image recovered from the CFA image captured without any anti-aliasing has a large amount of false-color artifacts on the brick wall. The image reconstructed from the CFA image acquired with anti-aliasing looks blurry. The high-frequency patterns are lost in this image. The visual result of defocusing acquisition is noticeably improved compared to the image acquired without any anti-aliasing filter.

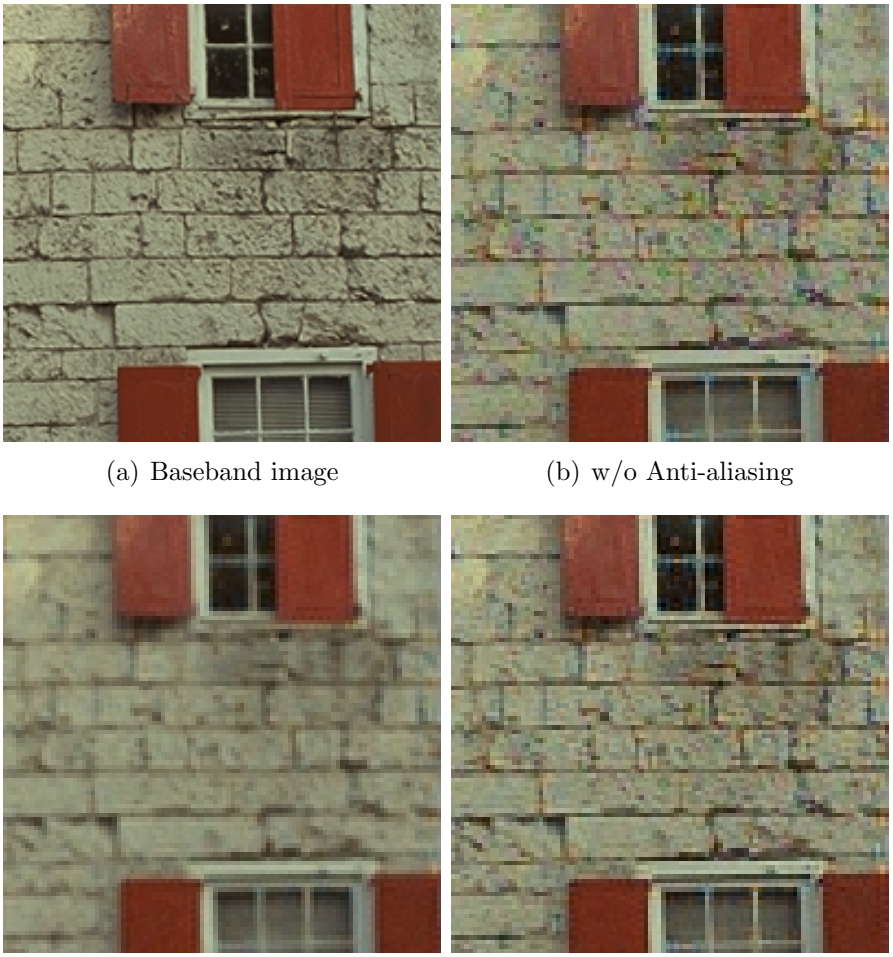

(a) Baseband image (b) w/o Anti-aliasing

(c) w/ Anti-aliasing (d) Defocusing acquisition

Figure 4.9: Cropped result images acquired from No. 1 scene by three different methods. The standard deviation of additive noise $\sigma = 2$.

Table 4.2 records the PSNR_3 results of the first 24 test scenes acquired by the three different approaches. When the additive noise level is low ($\sigma = 1$), the defocusing approach

provides around 1dB improvement in $PSNR_3$ values for most test images compared to no anti-aliasing filter. The difference between these two approaches is smaller for the larger noise case ($\sigma = 4$). The reason is that the noise amplification error is dominant when the noise level is high. The Wiener filter tends to choose the out-of-focus blur with smaller radii. In that case, the defocusing approach is approximately equivalent to the acquisition without an anti-aliasing filter. The $PSNR_3$ values of the acquisition method with an anti-aliasing filter are the lowest compared to the results of the other two methods.

Table 4.2: $PSNR_3$(dB) comparison of the images captured by three acquisition approaches for the first 24 test scenes: without an anti-aliasing filter (AA), with an anti-aliasing filter (AA) and defocusing acquisition (DA).

No.	$\sigma = 1$			$\sigma = 2$			$\sigma = 4$		
	AA	AA	DA	AA	AA	DA	AA	AA	DA
1	29.00	26.95	**30.31**	28.86	26.86	**29.91**	28.28	26.51	**28.91**
2	32.11	31.26	**32.75**	31.81	31.01	**32.22**	30.79	30.14	**31.00**
3	34.45	32.94	**35.22**	33.97	32.59	**34.36**	32.43	31.41	**32.59**
4	33.94	32.49	**34.69**	33.50	32.15	**33.88**	32.08	31.09	**32.23**
5	28.04	25.32	**28.91**	27.92	25.26	**28.53**	27.50	25.02	**27.69**
6	30.32	28.54	**31.75**	30.12	28.42	**31.22**	29.43	27.92	**29.99**
7	33.37	30.49	**34.10**	32.96	30.27	**33.42**	31.71	29.55	**31.83**
8	26.63	24.38	**27.82**	26.53	24.33	**27.65**	26.21	24.11	**26.91**
9	33.23	30.18	**34.26**	32.83	29.97	**33.46**	31.59	29.27	**31.80**
10	33.47	30.83	**34.52**	33.08	30.58	**33.65**	31.78	29.80	**31.97**
11	30.80	28.85	**32.00**	30.58	28.71	**31.48**	29.78	28.19	**30.20**
12	33.73	31.69	**35.05**	33.31	31.41	**34.06**	31.94	30.51	**32.24**
13	26.96	25.21	**28.31**	26.87	25.15	**28.04**	26.52	24.91	**27.18**
14	28.80	27.20	**29.36**	28.66	27.11	**29.14**	28.14	26.74	**28.41**
15	33.42	31.48	**34.17**	33.04	31.20	**33.53**	31.77	30.32	**31.97**
16	34.19	32.58	**35.42**	33.71	32.25	**34.38**	32.20	31.12	**32.27**
17	33.29	30.85	**34.28**	32.91	30.63	**33.47**	31.69	29.82	**31.83**
18	30.44	28.13	**31.43**	30.24	28.00	**30.96**	29.53	27.57	**29.84**
19	30.34	27.05	**31.86**	30.15	26.97	**31.28**	29.40	26.57	**30.02**
20	32.08	29.44	**33.16**	31.83	29.30	**32.56**	31.03	28.81	**31.33**
21	30.00	28.01	**31.22**	29.82	27.91	**30.75**	29.13	27.46	**29.57**
22	31.19	29.45	**32.19**	30.95	29.29	**31.69**	30.09	28.69	**30.45**
23	33.73	30.90	**34.33**	33.33	30.67	**33.59**	31.94	29.87	**32.01**
24	29.78	27.86	**30.78**	29.61	27.75	**30.35**	28.99	27.33	**29.32**

4.6 Conclusion and Discussion

We extended the adaptive image acquisition approach for the grayscale case to single-sensor color imaging in this chapter. Single-sensor color acquisition involves a CFA demosaicking step in the acquisition pipeline. Rather than an imaging model in the RGB domain, a new imaging model in the LC_1C_2 domain has been defined with consideration of aliasing components and additive noise. Owing to the spatial sampling characteristic of the Bayer CFA, the model built on the LC_1C_2 domain simplifies the formulation of the multichannel Wiener filter by reducing the cross-channel correlation.

The model-based multichannel Wiener filter is used to evaluate the reconstruction error during the acquisition. An initial captured CFA image is used to estimate the power spectrum of the continuous scene by a generic power spectral density function. Using this procedure, both the Wiener filter and the criterion are adapted to the input scene. An estimated reconstruction error criterion designed on the multichannel Wiener filter evaluates the optimal defocus setting for a specific scene. With this focus setting, the camera then acquires the final CFA image for the subsequent process. The final acquired CFA is reconstructed by a joint deblurring and demosaicking approach.

Numerical and visual results show that the defocusing acquisition approach outperforms traditional acquisition methods which capture images with or without a fixed anti-aliasing filter. The new approach is robust with respect to various noise levels and different kinds of scenes. The error criterion we formulated in this chapter predicts the true optimal focus setting accurately for most test scenes. The CFA images captured by the defocusing approach and recovered by the joint method have fewer false-color artifacts. Compared to the traditional acquisition method with an anti-aliasing filter, more high-frequency details are conserved by the new approach. By replacing the commonly-used birefringent filter with our defocusing approach, digital cameras will provide better visual quality.

Some practical challenges of our proposed approach remain, which we will investigate in our future study. Real input scenes are three-dimensional, but we assume they are flat in our

simulation. This affects the way the autofocus system controls the lens to generate a proper amount of out-of-focus blur. However, most scenes have a region of particular interest, and current autofocus algorithms take this into account. These regions are usually defined by a particular object of interest, which is approximately a constant distance from the camera and therefore yields a constant level of defocus. It is possible to apply our proposed approach to such regions and combine it with current autofocus algorithms to achieve better image quality. Another issue is the PSF of out-of-focus blur is approximated by circular blur, but real out-of-focus blur is more complicated and has to be analyzed for different type of lenses. However, regularized restorations are not very sensitive to the exact blur model, so this is not likely to be a significant practical problem.

Chapter 5

Spectral Sensitivity Optimization of Camera Sensor

Like the human visual system, most digital cameras acquire three different energies of light with different wavelengths to perceive a color scene. Instead of using the multisensor technique, most consumer cameras only have one optical sensor with a color filter array overlayed on it. The color filter ensures that each pixel of the sensor only samples one color of the input light, such as red, green or blue. This configuration allows the camera to capture three-dimensional color images with a two-dimensional optical sensor, and the results are CFA images. However, the dimension reduction from 3-D to 2-D generates spectrum overlaps in the spatial-frequency domain, which introduces aliasing artifacts. As a consequence, the choice of sensitivity functions for a CFA is crucial not only to the image acquisition but also to the subsequent reconstruction step.

The optimal sensitivity functions vary for scenes under different shooting conditions. Generally, a longer exposure time, higher ISO sensitivity or both of them is required in low-light shooting condition. Low light levels can increase noise variance significantly. A fixed spectral response of the CFA is not able to well balance the trade-off between the color reproduction accuracy and the noise amplification in the color transformation step. To solve this problem, we present an optimization procedure to select the sensitivity functions according to the signal-to-noise ratio (SNR).

5.1 Introduction

Human eyes sense a color scene using three types of cone cells as described in Sec. 2.4. A typical set of three sensitivity functions of the HVS is depicted in Fig. 5.1(a). Digital cameras use a similar strategy to the HVS to reproduce color. The spectral responses of a

Nikon D70 camera shown in Fig. 5.1(b) have shape and center spectral frequencies similar to the HVS. These functions affect the accuracy of color reproduction of the camera. Besides that, the appearance of noise plays an important role for optimizing the spectral sensitivity functions [78].

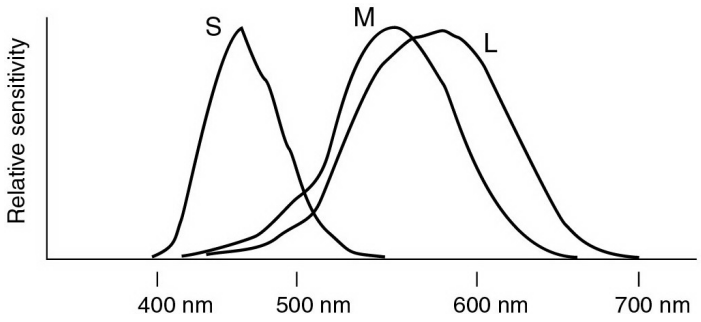

(a) Human visual system

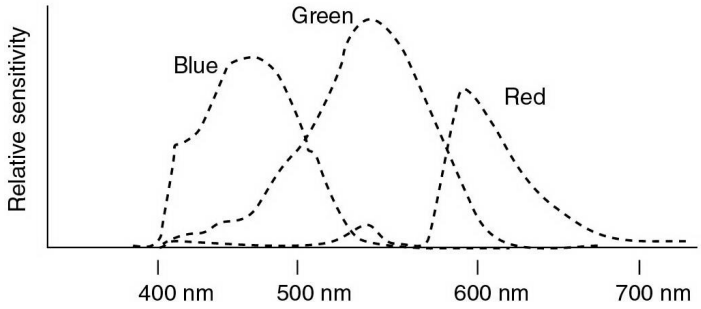

(b) Nikon D70 camera

Figure 5.1: Sensitivity functions of the HVS and a Nikon D70 camera [79].

While most demosaicking algorithms for single-sensor cameras only address the image reconstruction side [37, 80, 81], a considerable amount of work has been done to improve the sensitivity function selection of the color filter [12, 14, 15] on the image acquisition side. The spatio-spectral design approach proposed by Hirakawa proves that the spectral sensitivities of the color filter play a critical role in the color image acquisition [82]. Condat confirms that the follow-up demosaicking algorithm benefits from the CFA design with less computational cost or better image quality [7].

The color reproduction accuracy of a camera is determined by its sensitivity functions. The set with large overlaps among the three channels, such as shown in Fig. 5.1, allows more light to pass through the CFA to reach the optical sensor. This configuration helps to

increase the signal strength and reserve more spatial information in the CFA image. In the extreme case, a camera with three uniform sensitivity functions across the spectral-frequency domain becomes a black and white camera. However, the strong correlation among the three sensitivity functions amplifies the noise in the color transformation step [5, 83]. A trade-off between quantum efficiency and color reproduction accuracy is a challenge in CFA design.

A careful design of the sensor sensitivity functions and the spatial pattern of the color filter array reduces the burden on the demosaicking process. Most techniques in this area optimize the sensitivity functions based on a noise-free assumption [15, 84]. The resulting optimal sensor sensitivities are fixed without regard for the SNR, which is sub-optimal for a high noise level. To solve this problem, we choose a multichannel Wiener filter to optimize the sensitivity functions for the most commonly used Bayer CFA pattern. The optimizations for other CFA patterns can be derived using a similar framework.

Owing to hardware improvements in optics, it is possible to change the normally fixed sensitivity functions with tunable filters [85, 86]. Digital tunable filters have the capability to generate different spectral sensitivities under the control of liquid crystal (LC) devices. In such a filter, a stack of birefringent wave retarders determines the center spectral frequencies of the passband in the filter. The bandwidth of each passband is tuned by the LC layer of the filter. The wave retarder stack is disabled in the active stage to have an all-pass characteristic. In the passive stage, the spectral response of the digital tunable filter is the combination of its active response and the bandpass filter response generated by the wave retarder stack. Fig. 5.2 shows the spectral response of the active and passive stages of a typical digital tunable filter. The bandwidths of the three color channels are greatly reduced in the passive stage.

It is possible to overlay a digital tunable filter with an arbitrary spectral response on a normal CFA filter, which only changes the sensitivity function of the green channel in different stages. Another hardware solution is to use the technology in the interferometric

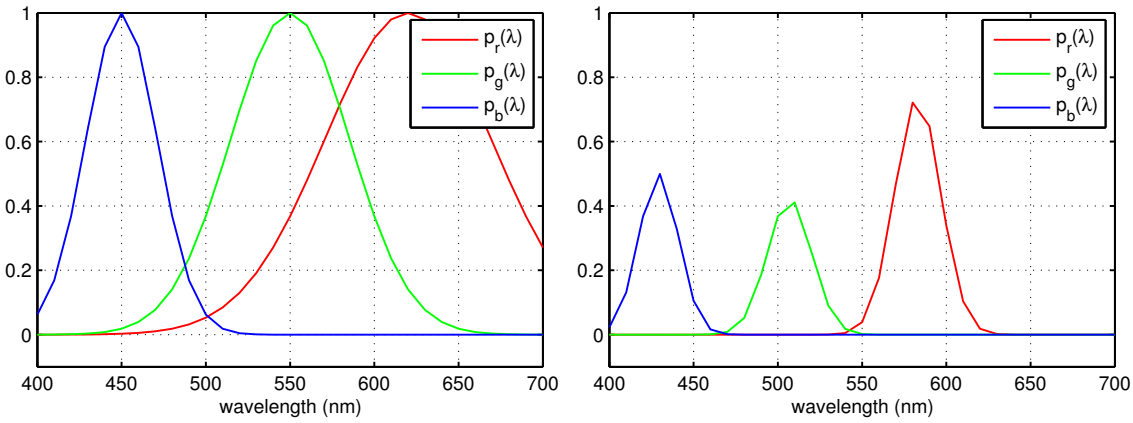

(a) Active stage (b) Passive stage

Figure 5.2: The spectral response of active and passive stages of a typical digital tunable filter. The center wavelengths of the wave retarder passband are 420nm, 500nm and 580nm.

modulator display (IMOD) [87]. The IMOD-based display can generate different colors pixel-wise via the interference of reflected light. Each pixel in the display contains one or more subpixels which can be turned on or off by the control circuit. By combining the reflected light of these subpixels, various color can be created at each pixel. Such a technology can be applied on the CFA design, in which green pixels can be designed to have variable spectral sensitivities.

To optimize the sensor sensitivities, a set of Gaussian curves with different center spectral frequencies and bandwidths are selected to model the spectral sensitivity functions of the camera. An IR blocking filter is applied on the sensitivity functions to simulate real applications. We formulated a multichannel Wiener filter which contains both the spatial and spectral information of the scene. Since noise plays a crucial role in both demosaicking and color reproduction, our optimization is a two-step process. We first optimize the CFA sensitivities for the normal shooting condition, in which the noise level is low. The solution of this step are the default sensitivity functions of the camera.

Then we fixed the spectral sensitivities of the red and blue sensors in the second step of the optimization. Since the green sensor has twice the sampling locations of the red or blue sensor in the Bayer CFA pattern, we optimize the bandwidth of green sensitivity to

the SNR of CFA images. The motivation for this scenario is that it represents a feasible hardware implementation in which the green filter can be electronically tuned for different lighting conditions. The optimal sensitivity functions for different noise levels are derived in this step.

This chapter is organized as follows. The color imaging models of both the camera and the HVS are introduced in the Sec. 5.2. The definition of sensitivity functions, color transformation and the special case of the Bayer CFA are also described in this section. The multichannel Wiener filter is formulated in Sec. 5.3 to linearly reconstruct the captured CFA images by the camera sensitivity functions. We report simulation results of our optimization on selection of sensitivity functions in Sec. 5.4. Finally, we discuss our future work and draw some conclusions in Sec. 5.5.

5.2 Multispectral Imaging Model

Multispectral imaging is different from ordinary image acquisition and reconstruction problems. Instead of recovering the reflectance or radiance in the spectral-frequency domain, we intend to minimize the error between the image acquired by the camera and the image obtained in CIEXYZ color space which truly represents the HVS. The linear transform from the camera color space to the CIEXYZ space enables the camera to reproduce color accurately. We introduce the two imaging models first, then describe how to connect them by color transformation. The special imaging model of the Bayer CFA is presented at the end of this section.

5.2.1 Camera Imaging Model

Color image formation in a camera can be described as an optical sensor recording the reflected illuminant $l(\lambda)$ incident on an object with a nonluminescent surface $r(\lambda)$ [88]. The term $r(\lambda)$ denotes the reflectance of the nonluminescent surface. At each cell of the sensor,

this process can be written as an integration over the wavelength in the visible light range

$$g_c = \int_{\lambda_{min}}^{\lambda_{max}} p_c(\lambda) l(\lambda) r(\lambda) d\lambda \tag{5.1}$$

where g_c denotes the captured color value. The function $p_c(\lambda)$, which is normally called the sensor sensitivity, describes the combined response of the optical sensor and the spectral transmittance of the color filter.

Since the visible spectrum is from 400 nm to 700 nm, we define an integer K to be the total number of samples in this spectral range. Consider a camera with an $m \times n$ sensor array and denote $N = m \times n$. Let the matrix $P \in \mathbb{R}^{qN \times KN}$ has the form

$$P = \begin{bmatrix} p_1^T \otimes I_N \\ p_2^T \otimes I_N \\ \vdots \\ p_q^T \otimes I_N \end{bmatrix} \tag{5.2}$$

where I_N is the identity matrix with size $N \times N$ and the vector $p_i \in \mathbb{R}^{K \times 1}$, $i = 1, 2, \cdots, q$, is the sampled spectral sensitivity function of the ith color. The imaging model defined in Eq. (5.1) can be extended to the entire image in a matrix-vector form:

$$g = PLr \tag{5.3}$$

The vector $r = [r_1^T, r_2^T, \cdots, r_K^T]^T$ represents the reflectance of the input scene, where $r_i \in \mathbb{R}^{N \times 1}$, $1 \leq i \leq K$, contains the sampled reflectance spectrum of the ith spatial location. The block-diagonal matrix $L = \text{diag}(L_1, L_2, \cdots, L_K)$ records the illuminant spectra, where $L_i = l_i I_N$, $1 \leq i \leq K$, is a diagonal block. The constant l_i is the illuminant spectrum value at the ith spectral sampling locations.

For simplicity we only optimize the sensitivity functions under the standard D65 illuminant. Let $x = Lr$ denote the spectral radiance of the scene under the D65 illuminant. Then

the simplified image formation model of Eq. (5.3) is given by:

$$g = Px \tag{5.4}$$

Most published work in the color imaging area assumes that the radiance information is sufficiently conserved with a 10 nm sampling interval. This results in $K = 31$ samples for the visible wavelength range from 400 nm to 700 nm.

5.2.2 Human Visual System Imaging Model

A digital camera matches the color sensitivity of human eyes with a set of similar sensitivity functions as shown in Fig. 5.1. Despite the complexity of our eyes, the color perception of the human eye has been well studied since the 1920s. To eliminate the variation of human eyes, CIE defined the 2° standard observer to formulate the CIE1931 XYZ color space followed by a slightly modified version—CIE1964 XYZ space with the 10° standard observer. Since the CIEXYZ color space is closer to the human visual subspace than other spaces [89], it is normally chosen to truly represent the scene perceived by the HVS.

The color matching functions of the CIEXYZ color space can be described by a matrix

$$\bar{A} = \begin{bmatrix} \bar{x}^T \\ \bar{y}^T \\ \bar{z}^T \end{bmatrix} \tag{5.5}$$

where $\bar{x}$, $\bar{y}$ and $\bar{z} \in \mathbb{R}^{31\times 1}$ are the sampled CIEXYZ color matching functions in Fig. 2.8(b). Let $f = [f_x^T, f_y^T, f_z^T]^T$, $f_i \in \mathbb{R}^{N\times 1}$, $i = x, y, z$, be the vector of the full-color image captured in CIEXYZ space. The following equation describes the acquisition process under the illuminant L:

$$f = ALr \tag{5.6}$$

where the matrix $A \in \mathbb{R}^{3N \times 31N}$ represents the projection from the scene radiances to the CIEXYZ color space and has the form

$$A = \begin{bmatrix} \bar{x}^T \otimes I_N \\ \bar{y}^T \otimes I_N \\ \bar{z}^T \otimes I_N \end{bmatrix} \tag{5.7}$$

A similar imaging model to the one defined in Eq. (5.4) can be derived by using a fixed illuminant L

$$f = Ax \tag{5.8}$$

where the vector x represents the scene radiance under the fixed illuminant D65.

5.2.3 Sensor Sensitivities and Color Transformation

Strictly speaking, the acquired image g_s in Eq. (5.4) is not a color image but the projected scene radiance from the visible spectrum to the camera color space. Before this image is transformed to CIEXYZ color space, the color difference between the image captured by the camera and the true color image in the CIEXYZ space mainly depends on how similar the camera sensitivity function P and the CIEXYZ matching function A is. However, no linear transform from the camera color space to the CIEXYZ space can be performed without generating errors unless the sensor has a response which is a linear combination of CIEXYZ standard matching functions [90, 91]. As a result, a linear transform T is chosen to minimize the color difference between these two spaces

$$T = \underset{T}{\operatorname{argmin}} \left\{ \|\bar{T}g - f\|^2 \right\} \tag{5.9}$$

where the block matrix $\bar{T}$ has the form

$$\bar{T} = T \otimes I_N \tag{5.10}$$

The linear transform T can be considered as a reference by which the camera knows the true color of the perceived value in the CIEXYZ space.

The color matching functions M corresponding to the camera sensitivity functions $\bar{P}$ is given by

$$\bar{M} = T\bar{P} \tag{5.11}$$

where the color match matrix $\bar{M}$ has the form

$$\bar{M} = \begin{bmatrix} m_r^T \\ m_g^T \\ m_b^T \end{bmatrix} \tag{5.12}$$

The vectors m_r, m_g and m_b are the three color matching functions of the red, green and blue channels. The sensitivity matrix $\bar{P}$ is the special case of Eq. (5.2) when $N = 1$, such as

$$\bar{P} = \begin{bmatrix} p_1^T \\ p_2^T \\ \vdots \\ p_q^T \end{bmatrix} \tag{5.13}$$

A traditional way to derive the transformation matrix T for a given sensitivity matrix $\bar{P}$ requires prior knowledge of reflectance. A set of scenes with known reflectance are acquired by the camera sensitivity functions and the standard CIEXYZ matching function under a standard illuminant spectrum. The GretagMacbeth ColorChecker is normally chosen to be the training scene for this purpose, which is shown in Fig. 5.3. Twenty-four tristimulus values are acquired under D65 illuminant using Eq. (5.4) and (5.8) to build the matrices G_s^m and $F^m \in \mathbb{R}^{24\times 3}$, where each row of these two matrices represents the tristimulus value of each color patch. Each row of the linear transformation matrix T can be computed by

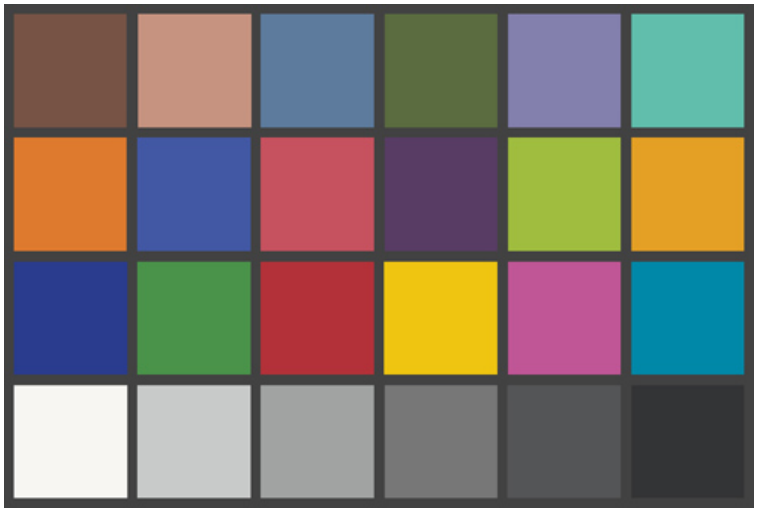

Figure 5.3: The GretagMacbeth ColorChecker [92].

solving the linear equations

$$G_s^m T_i^T = f_i^m \tag{5.14}$$

where T_i is the ith row of T and f_i^m is the ith column of F^m, $i = 1, 2, 3$. The color matching functions can be derived using Eq. (5.11). Fig. 5.4 shows one set of sensitivity functions and the corresponding color matching functions derived by this method.

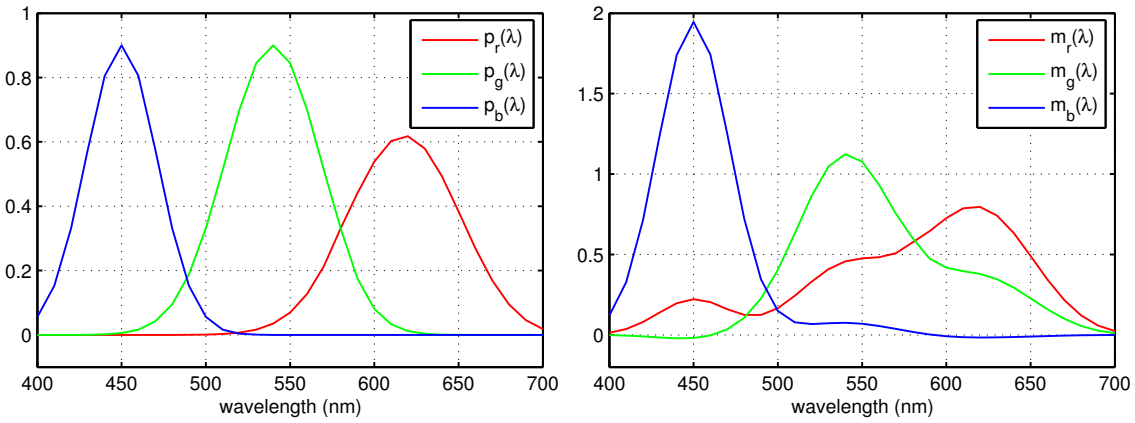

(a) Sensitivity functions (b) Color matching functions

Figure 5.4: Camera sensitivity functions and the corresponding color matching functions.

5.2.4 Imaging with Bayer Color Filter Array

To model the single-sensor acquisition in most cameras, a matrix D is used to downsample a full-color image to generate a CFA image. Assuming that the camera acquires images with a Bayer CFA, then a noisy imaging model for this process is defined by

$$y = DPx + u \tag{5.15}$$

where y represents the noisy CFA image and $u \in \mathbb{R}^{N\times 1}$ is the measurement noise vector. We treat the green channel at two different spatial sampling locations in the 2×2 Bayer pattern as two different color channels. The spatial sampling matrix D has the form $D = \text{diag}(D_r, D_g, D_b)$. The block D_i, $i = r, g, b$, is a row-deficient identity matrix that samples the corresponding color channel according to the Bayer CFA pattern.

5.3 Multichannel Wiener filter

The best linear minimum mean square estimate $\hat{f}$ is given by the multichannel Wiener filter

$$\hat{f} = Wy \tag{5.16}$$

Applying Eq. (5.8) and (5.15), the Wiener filter W can be derived by

$$\begin{aligned} W &= E\{fy^T\}E\{yy^T\}^{-1} \\ &= E\left\{Axx^TM^TD^T\right\}E\{DPxx^TP^TD^T + DPxu^T + ux^TP^TD^T + uu^T\}^{-1} \\ &= AR_xP^TD^T[DPR_xP^TD^T + DPR_{xu} + R_{ux}P^TD^T + R_u]^{-1} \end{aligned} \tag{5.17}$$

where R_x and R_u are the autocorrelation matrices of the scene radiance and noise. We assume that the scene and noise are uncorrelated with each other; that is, $R_{xu} = R_{ux} = 0$.

Then the above equation can be simplified as

$$W = AR_xP^TD^T[DPR_xP^TD^T + R_u]^{-1} \tag{5.18}$$

The scene autocorrelation matrix R_x has the form

$$R_x = \begin{bmatrix} R^{(1,1)} & R^{(1,2)} & \cdots & R^{(1,31)} \\ R^{(2,1)} & R^{(2,2)} & \cdots & R^{(2,31)} \\ \vdots & \vdots & \ddots & \vdots \\ R^{(31,1)} & R^{(31,1)} & \cdots & R^{(31,31)} \end{bmatrix} \tag{5.19}$$

whose blocks contain both the spatial and spectral correlation coefficients. In particular, the block $R^{(i,j)}$ records the spatial-spectral correlation between the scene radiance at ith and jth spectral locations, $1 \leq i, j \leq 31$. Direct implementation of matrix R_x is difficult without any simplification because of its large size. Assuming that the spatial and spectral correlations are separable, one can rewrite the matrix R_x as

$$R_x = \begin{bmatrix} r^{(1,1)}R_s & r^{(1,2)}R_s & \cdots & r^{(1,31)}R_s \\ r^{(2,1)}R_s & r^{(2,2)}R_s & \cdots & r^{(2,31)}R_s \\ \vdots & \vdots & \ddots & \vdots \\ r^{(31,1)}R_s & r^{(31,2)}R_s & \cdots & r^{(31,31)}R_s \end{bmatrix} \tag{5.20}$$

where the block $R_s \in \mathbb{R}^{N\times N}$ describes the spatial correlation of the scene and the constant $r^{(i,j)}$, $1 \leq i, j \leq 31$, denotes the spectral correlation between the ith and jth scene radiance. Eq. (5.20) can be further written as a Kronecker product

$$R_x = R_r \otimes R_s \tag{5.21}$$

where $R_r \in \mathbb{R}^{31\times 31}$ is the spectral correlation matrix.

Applying Eq. (5.21), the multichannel Wiener filter can be rewritten as

$$W = A(R_r \otimes R_s)P^T D^T [DPR_x P^T D^T + R_u]^{-1} \tag{5.22}$$

We have the identity: $A(R_r \otimes R_s)P^T = (\bar{A}R_r\bar{P}^T) \otimes R_s$. The proof of is presented in Appendix C. The Wiener filter can be further written as

$$\begin{aligned} W &= [(\bar{A}R_r\bar{P}^T) \otimes R_s]D^T[D\bar{P}R_x P^T D^T + R_u]^{-1} \\ &= \{[(\bar{A}R_r\bar{P}^T) \otimes R_s](PR_x P^T)^{-1}\}\{(PR_x P^T)D^T[DPR_x P^T D^T + R_u]^{-1}\} \end{aligned} \tag{5.23}$$

The second part of Eq. (5.23) is the linear minimum-mean-square estimator of the full-color image g in Eq. (5.4) given the observed CFA image y. In fact, the Wiener filter

$$W_s = (PR_x P^T)D^T[DPR_x P^T D^T + R_u]^{-1} \tag{5.24}$$

linearly demosaics the CFA image y in the camera color space. The first part of Eq. (5.23) can be rewritten as

$$\begin{aligned} W_r &= [(\bar{A}R_r\bar{P}^T) \otimes R_s](PR_x P^T)^{-1} \\ &= [(\bar{A}R_r\bar{P}^T) \otimes R_s][(\bar{P}R_r\bar{P}^T) \otimes R_s]^{-1} \end{aligned} \tag{5.25}$$

Using the mixed-product property of the Kronecker product given in Appendix C, we have

$$\begin{aligned} W_r &= [(\bar{A}R_r\bar{P}^T) \otimes R_s][(\bar{P}R_r\bar{P}^T)^{-1} \otimes R_s^{-1}] \\ &= \bar{A}R_r\bar{P}^T(\bar{P}R_r\bar{P}^T)^{-1} \otimes I_N \end{aligned} \tag{5.26}$$

In fact, the process described in the above equation is the color matching step accomplished by a Wiener filter. As described in Chapter 1, the color transformation is accomplished after demosaicking. By assuming the spectral and spatial correlations are separable in the

multichannel Wiener filter, we equivalently separate the demosaicking and color matching step in the pipeline.

Implementing the multichannel Wiener filter in the spatial domain involves a huge matrix inversion. A similar approach to the one introduced in Sec. 4.1.3 can be used here with the benefit of the FFT algorithm. Assuming the scene is wide sense stationary in the spatial-frequency domain, a Fourier transform in the spatial-frequency domain diagonalizes the spatial correlation matrix R_s and the result is the spatial power spectrum S_s

$$S_x = R_r \otimes S_s \tag{5.27}$$

The multichannel Wiener filter in the spatial-frequency domain has the form

$$\mathcal{W} = AS_xM^T\mathcal{T}^H \left[\mathcal{T}MS_xM^T\mathcal{T}^H + S_u\right]^{-1} \tag{5.28}$$

where S_u represents the noise power spectrum. The transform $\mathcal{T}$ is the equivalent operation in the spatial-frequency domain corresponding to the spatial sampling of the Bayer pattern. The definition of this transform is provided in Appendix B.

The spatial power spectrum S_s can be estimated using the same method introduced in Sec. 4.2.3. The green channel of the acquired CFA image is chosen to estimate the parameters in the isotropic power density function model (Eq. (4.30)). Since there is no blur degradation in the image acquisition, the inverse filtering described in Eq. (4.28) is not necessary here for the power spectrum estimation. Based on our tests, the random process in the spectral-frequency domain is nonstationary in general. As a result, the correlation matrix R_r is not a Toeplitz matrix but only a symmetric matrix. Fig. 5.5 depicts the spectral correlation matrix of a multispectral image along with a 31×31 correlation matrix of a stationary process. To avoid bias in the solution, we use the mean correlation matrix of the multispectral images in the test library as prior knowledge to increase the accuracy.

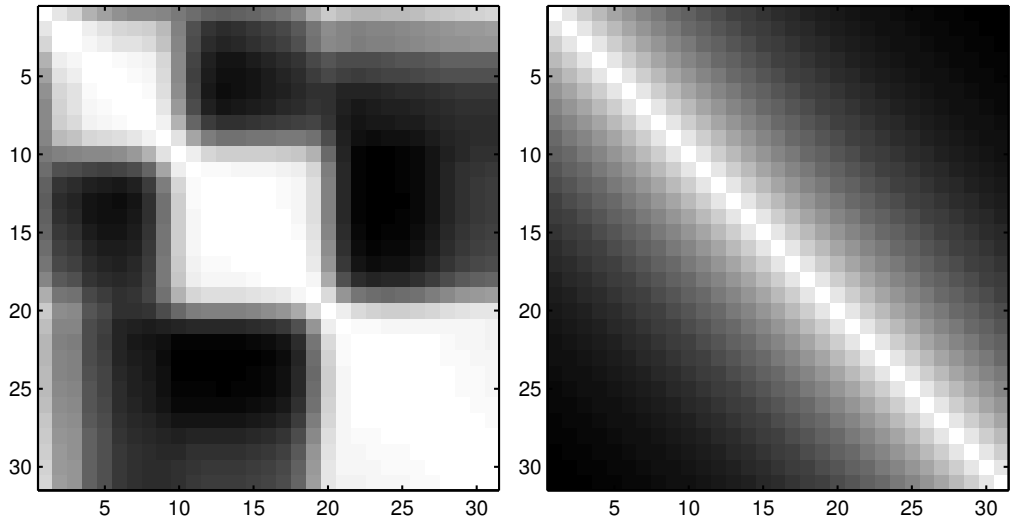

(a) Nonstationary spectral correlation matrix

(b) Stationary correlation matrix

Figure 5.5: An example of the nonstationary correlation matrix of multispectral image comparing with the correlation matrix of stationary random process.

5.4 Simulation and Results

5.4.1 Optimization Metric

The single-sensor imaging model formulated in Eq. (5.15) is in the CIEXYZ color space, which is not perceptually uniform. In other words, the tristimulus distance does not truly represent the color difference between two points in the XYZ color space. Since the Y channel of XYZ color space measures the luminance of the scene, one can use only two parameters to represent the tristimulus values for a given Y. Define

$$\begin{aligned} x &= \frac{X}{X+Y+Z} \\ y &= \frac{Y}{X+Y+Z} \\ z &= \frac{Z}{X+Y+Z} = 1-x-y \end{aligned} \tag{5.29}$$

where X, Y and Z are tristimulus values in the CIEXYZ color space. The new color space is known as the CIE xyY color space. Fig. 5.6 depicts the chromaticity of the CIEXYZ space

using x and y as two axes. It is clear that the geometric distance in this plot is not linearly related to the color difference.

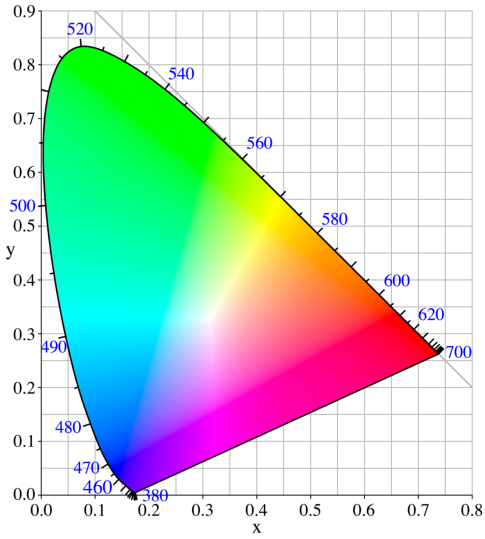

Figure 5.6: The CIEXYZ color space chromaticity diagram [93]. The plot is shown in sRGB color space.

In a perceptually uniform color space, a change of the same amount in the tristimulus value results in a change of about the same visual difference. As described in Chapter 2, the CIELAB color space is a perceptually uniform space. The nonlinear transform between the CIEXYZ and CIELAB spaces is given in Eq. (2.16) and (2.17). The color difference between two colors in CIELAB space is defined by

$$\Delta E^*_{ab} = \sqrt{(L^*_1 - L^*_2)^2 + (a^*_1 - a^*_2)^2 + (b^*_1 - b^*_2)^2} \tag{5.30}$$

where (L^*_1, a^*_1, b^*_1) and (L^*_2, a^*_2, b^*_2) are two colors in the CIELAB space. Since we evaluate the color difference over the entire image plane, the mean color difference of all pixels is chosen to be our error criterion.

5.4.2 Sensitivity Function Optimization

To simplify the optimization, we assume that the camera sensor with a Bayer CFA senses three different colors. We further assume that the three sensitivity curves of the camera sensor have a Gaussian shape [78]

$$\mathcal{S}_i(\lambda) = \exp\left(-\frac{(\lambda - \lambda_i)^2}{w_i^2}\right) \tag{5.31}$$

where λ_i and w_i, $i = r, g, b$, control the center spectral frequency and the bandwidth of the ith channel. An IR blocking filter is applied on the three Gaussian curves to simulate a real camera. The definition of this filter is given by [78]

$$f_{IR}(\lambda) = \begin{cases} 0.9, & \text{if } 400 \text{ nm} < \lambda \leq 580 \text{ nm}, \\ -\frac{9}{1400}\lambda + \frac{162}{35}, & \text{if } 580 \text{ nm} < \lambda \leq 720 \text{ nm}, \\ 0, & \text{elsewhere.} \end{cases} \tag{5.32}$$

Fig. 5.7 depicts the spectral-frequency response of the IR blocking filter. The continuous

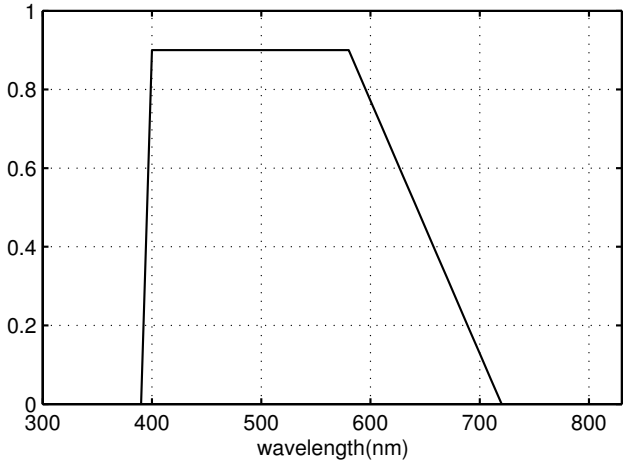

Figure 5.7: IR blocking filter response.

function $\mathcal{P}_i$ is a combination of the Gaussian curve and the IR blocking filter:

$$\mathcal{P}_i(\lambda) = \mathcal{S}_i(\lambda) f_{IR}(\lambda) \tag{5.33}$$

The sensitivity vector p_i can be acquired by sampling the corresponding curve $\mathcal{P}_i$ with a 10 nm interval in the visible wavelength range.

Yasuma et al. presented a multispectral image database which contains 32 images [94]. They acquired these images using a cooled CCD camera (Apogee Alta U260) for a wide variety of real-world materials and objects. The range of wavelength is from 400 nm to 700 nm which results in 31 bands for each multispectral image. The illuminant used in the acquisition was the CIE standard D65, and the camera was focused on the 550 nm image band. The spatial resolution of these image is 512×512. We chose the first sixteen images in the library to optimize the sensitivity functions. Fig. 5.8 shows their corresponding sRGB images acquired under D65 illuminant.

As described in Sec. 5.3, the spectral random process is not stationary. The most commonly used decaying-exponential model is not able to capture the correlation among spectral bands. To avoid the errors introduced by an inaccurate correlation model, we precomputed the spectral correlation matrices of sixteen images. The mean is shown in Fig. 5.9. We use this matrix as the spectral correlation matrix in the multispectral Wiener filter to optimize the sensitivity functions.

We acquired the ground truth image f using the imaging model (5.8) with the standard CIEXYZ color matching functions. For optimization purposes, the spatial power spectrum S_s of each test image was estimated from the Y channel of image f using the isotropic power density function model (4.30). The SNR is defined by

$$\mathrm{SNR}_{\mathrm{dB}} = 20 \log_{10} \frac{\bar{f}}{\sigma} \tag{5.34}$$

where $\bar{f}$ is the mean of the image f and σ is the noise standard deviation.

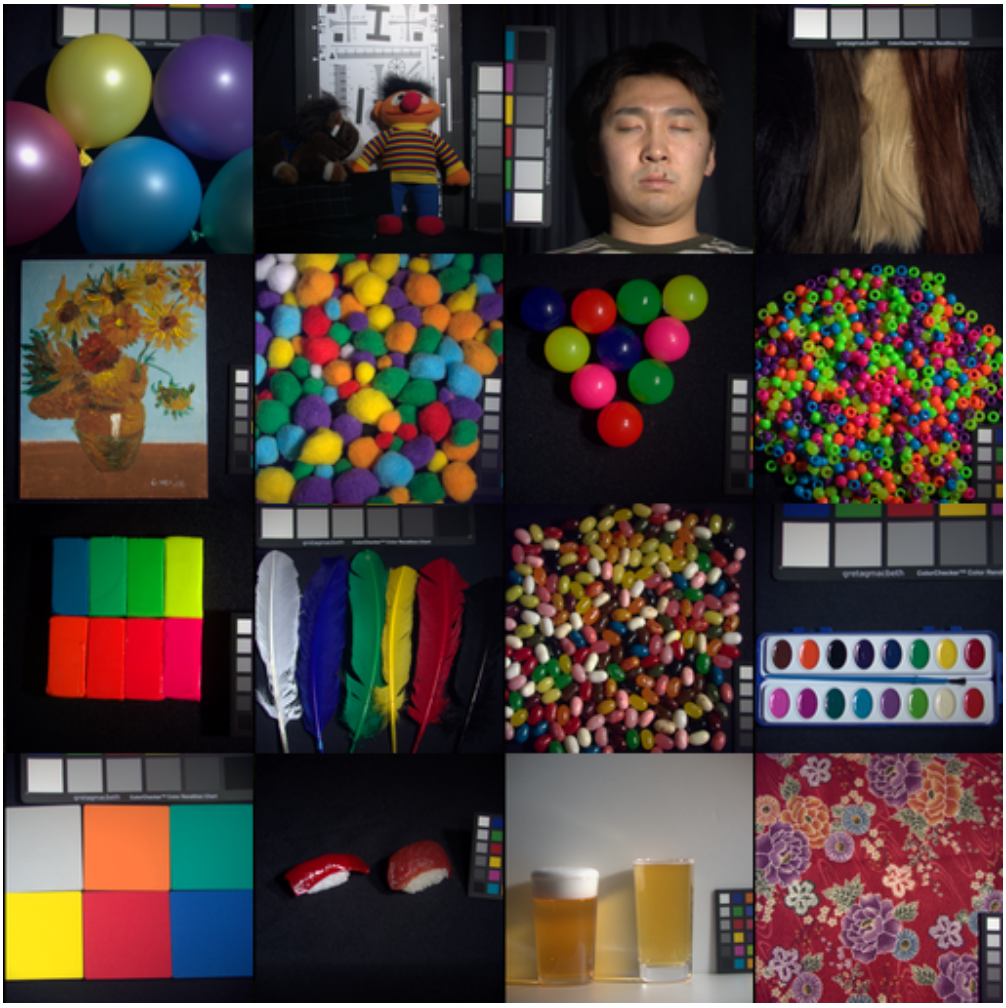

Figure 5.8: The sixteen multispectral images for the optimization rendered into sRGB color space under D65 illuminant.

To find the optimal solution for the low-noise level, we generated a series of sensitivity functions with the center frequencies in the ranges $\lambda_r = 600$–700 nm, $\lambda_g = 500$–600 nm and $\lambda_b = 400$–500 nm. The bandwidth parameters w_i, $i = r, g, b$, is in the range of 5–100. The CFA images were obtained by the model (5.15) with the corresponding sensitivity functions. We fixed the SNR at 40 dB and calculated the noise variance using Eq. (5.34). The multichannel Wiener filter in Eq. (5.28) was chosen to reconstruct the full-color images in the CIEXYZ color space.

To speed up the optimization process, the searching steps for all the design parameters were initially set to 20 to locate the range of the optimal solution. After that, the step of

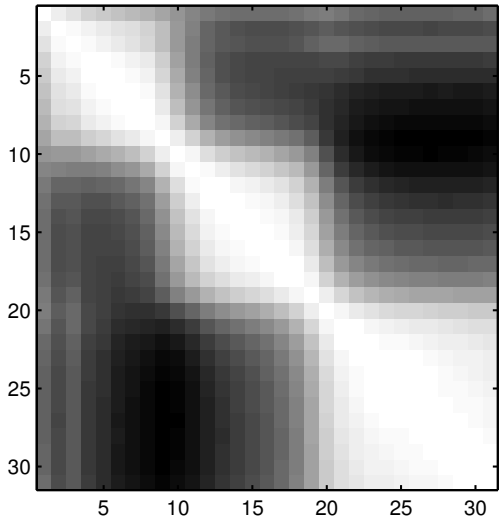

Figure 5.9: The average spectral correlation matrix of the first sixteen images in the library.

center frequencies is reduced to 10 nm, while the step of bandwidth is reduced to 5. We transferred both the reconstructed image $\hat{f}$ and the true image f into the CIELAB color space to calculate the color difference between them. The sensitivity function set which results in the minimum average color difference over the sixteen images was considered the optimal choice. The optimal sensitivity functions we found in the first step of the optimization are shown in Fig. 5.10(a). The center frequency and bandwidth parameters are $(\lambda_r, \lambda_g, \lambda_b) = (610, 550, 450)$ and $(w_r, w_g, w_b) = (50, 50, 30)$. The corresponding color matching functions are depicted in Fig. 5.10(b).

The second step of optimization aimed to discover the optimal green sensitivity functions for different noise levels. We fixed the center frequency λ_i, $i = r, g, b$, and the bandwidth parameters w_r and w_b to the solution in the first optimization. This simplifies the design scope and makes the sensitivity functions physically feasible. We tuned the green channel bandwidth parameter w_g in the range of 5–100 with a step of 5. The SNRs we optimized are in the range of 10 dB to 35 dB with a 5 dB step. The multichannel Wiener filter and the error metric employed in this step is the same as the one used in the first step of optimization. The green channel sensitivity function with the minimum average color difference over the sixteen images is the optimal green sensitivity.

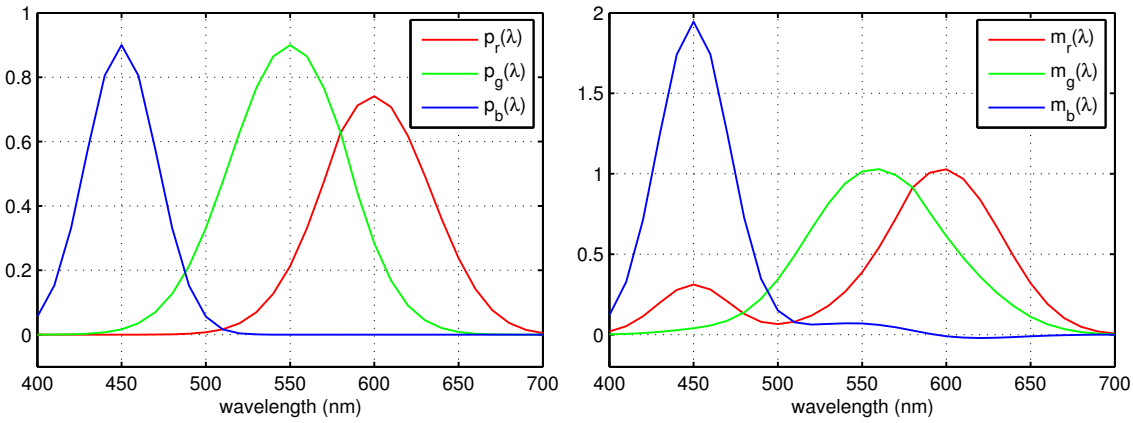

(a) Sensitivity functions (b) Color matching functions

Figure 5.10: The optimal sensitivity functions and the corresponding matching functions for 40 dB SNR.

We report the optimal green bandwidth parameters w_g for different SNRs in Table 5.1. The bandwidth of green channel sensitivity function reduces as the SNR comes down. The optimal green sensitivity is the same as the result in the first step of optimization when the SNR is larger than 25 dB. The sensitivity functions and the matching functions shown in Fig. 5.11 are the optimal sensitivities for the SNRs of 10 dB, 20 dB and 30 dB. Although the sensitivity functions of the red and blue channels are the same, their matching functions have been slightly changed by the green channel sensitivity.

Table 5.1: The optimal green channel bandwidth parameters w_g for different SNRs.

SNR	10 dB	15 dB	20 dB	25 dB	30 dB
w_g	20	30	40	45	50

5.4.3 Multispectral Image Reconstruction

To visually and numerically verify the performance of the optimal sensitivity functions, we applied them on the remaining sixteen multispectral images in the library to acquire the CFA images. Fig. 5.12 shows the corresponding sRGB images of the sixteen multispectral images acquired under D65 illuminant. The SNRs were set to the range from 10 dB to

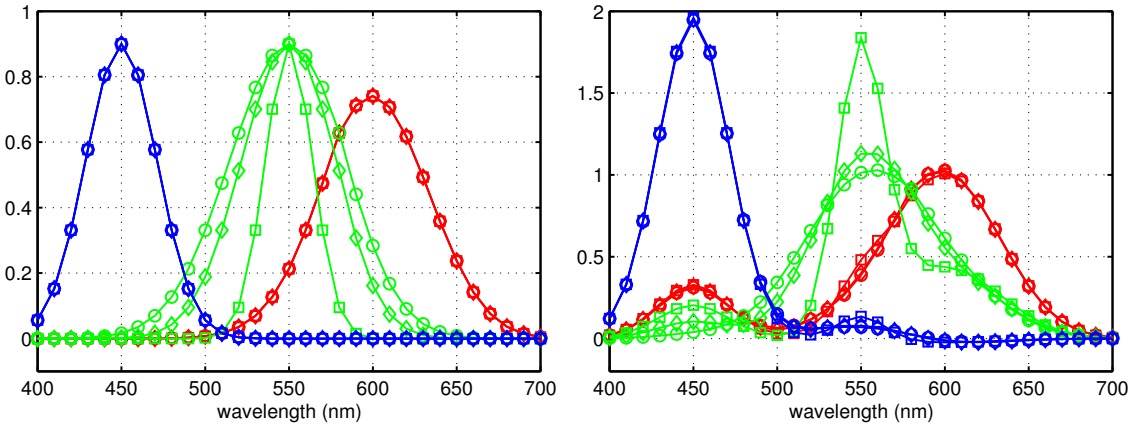

(a) Sensitivity functions (b) Color matching functions

Figure 5.11: The optimal sensitivity functions and corresponding matching functions for different SNRs. The curves are labeled by "□" (10 dB), "◇" (20 dB) and "○" (30 dB).

25 dB with a 5 dB increment. At each SNR level, we obtained one CFA image using the optimal sensitivity functions and acquired the other CFA image using the default sensitivity functions (the optimal sensitivity function for 40 dB SNR).

The CFA images are then reconstructed by a frequency-domain demosaicking method [57]. Assuming that the demosaicking does not change the noise variance, we applied a single-channel Wiener filter to linearly denoise each color channel independently. The full-color images were transferred from the camera color space to the CIEXYZ space by applying a linear transform T on the tristimulus value of each pixel. The transformation matrix T was calculated by the method described in Sec. 5.2.3. We calculated the color difference between the resulting image and the image acquired directly using the CIEXYZ standard matching functions in the CIELAB color space.

Table 5.2 shows the color difference ΔE^*_{ab} between the reconstructed CFA images, which were captured by the fixed and the optimal sensitivity functions. Since the optimal green sensitivity for 30 dB and 35 dB are the same as the fixed sensitivity for the 40 dB case, they are not included in this table. Generally speaking, images with smaller color differences have better visual quality than images with larger values. We show the smaller ΔE^*_{ab} values of each SNR in bold.

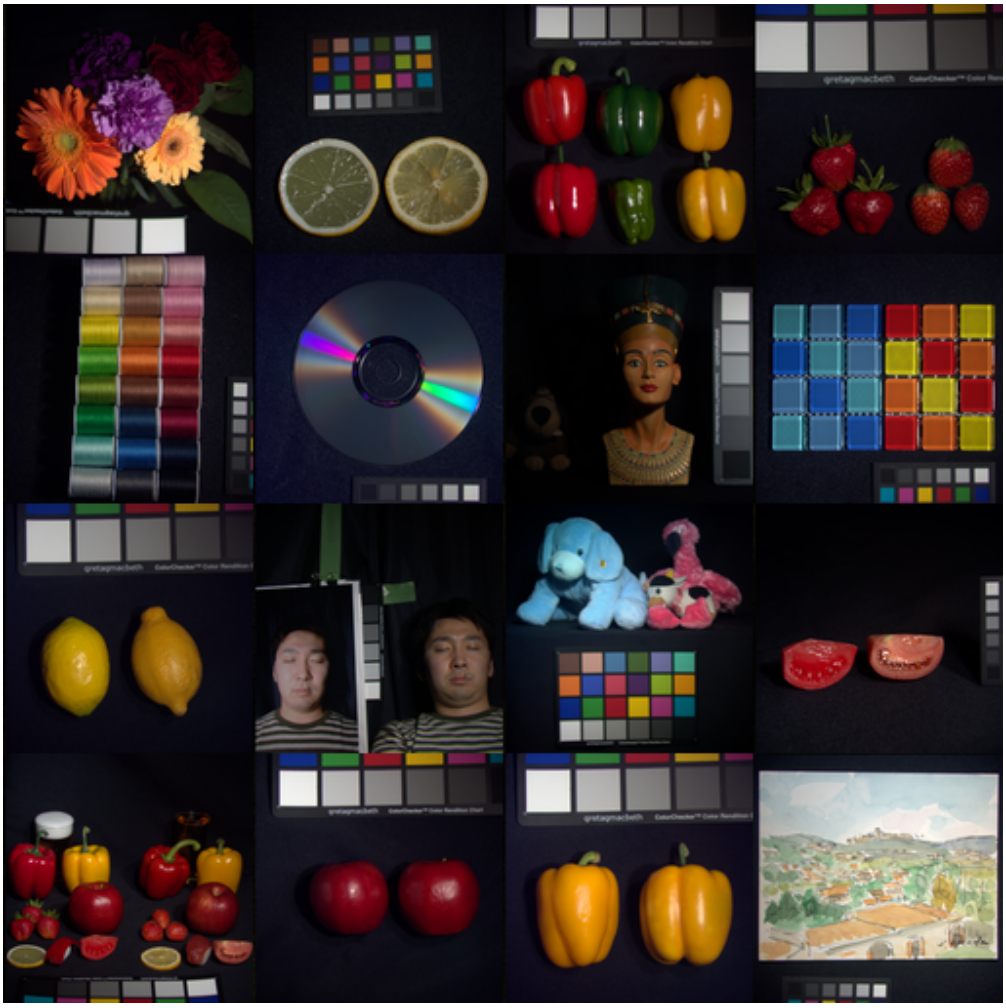

Figure 5.12: The sixteen multispectral images for the reconstruction rendered into sRGB color space under D65 illuminant.

A portion of No. 1 test image in Fig. 5.13 and the cropped No. 5 test image in Fig. 5.14 depict the reconstructed sRGB images of the CFA acquired by the fixed and optimal sensitivity functions at different noise levels. The absolute difference image between the reconstructed image and the true sRGB image is also shown in each figure. Due to the gamma correction in the transformation from the CIEXYZ to the sRGB color space, the noise in the low intensity regions was amplified more than the noise in the high intensity regions. The images reconstructed from the CFA images acquired by the optimal sensitivity functions are less noisy with accurate color reproduction, which verifies the result of our numerical analysis.

Table 5.2: Color difference ΔE^*_{ab} comparison of the images captured by the fixed and the optimal sensitivity functions at different SNR levels. The SNR levels are 10 dB, 15 dB, 20 dB and 25 dB.

No.	10 dB		15 dB		20 dB		25 dB	
	fixed	opt.	fixed	opt.	fixed	opt.	fixed	opt.
1	18.65	**15.86**	12.52	**10.97**	8.08	**7.39**	5.40	**5.14**
2	17.20	**14.33**	11.60	**9.93**	7.68	**6.89**	5.44	**5.11**
3	16.95	**14.44**	11.04	**9.77**	7.00	**6.57**	4.50	**4.48**
4	17.81	**14.79**	11.94	**10.10**	7.74	**6.80**	5.12	**4.77**
5	19.54	**16.45**	12.81	**11.02**	8.23	**7.39**	5.56	**5.22**
6	13.29	**11.73**	9.42	**8.80**	6.48	**6.66**	4.71	**5.16**
7	14.67	**12.17**	9.38	**7.92**	5.82	**5.12**	3.70	**3.42**
8	22.53	**19.21**	15.50	**13.66**	10.70	**9.95**	7.93	**7.72**
9	16.96	**14.18**	11.86	**10.09**	7.70	**6.84**	5.01	**4.72**
10	16.71	**14.04**	10.82	**9.32**	6.83	**6.19**	4.40	**4.20**
11	20.80	**17.78**	15.55	**12.98**	10.23	**8.96**	6.55	**5.99**
12	12.10	**10.22**	7.49	**6.54**	4.76	**4.32**	3.21	**3.08**
13	15.77	**13.25**	10.41	**9.07**	6.86	**6.19**	4.71	**4.54**
14	13.29	**10.91**	8.70	**7.31**	5.52	**4.78**	3.54	**3.29**
15	16.43	**14.33**	11.81	**10.38**	7.74	**7.14**	5.02	**4.93**
16	20.40	**17.63**	16.23	**13.83**	11.44	**9.80**	7.48	**6.75**

5.5 Conclusion and Discussion

In this chapter, an optimization of the sensitivity functions for the Bayer sensor is presented. A Wiener filter with consideration of both spatial and spectral correlations is formulated based on a multispectral imaging model. We use this Wiener filter to reconstruct the CFA images acquired by the simulated camera sensitivity function during the optimization. The color difference in the CIELAB color space is chosen to be the error metric. Since a digital tunable filter makes it feasible to have a CFA with tunable spectral response, we further optimized the green channel bandwidth according to the noise level. The reconstruction results show that the CFA images acquired by the optimal sensitivity functions can be recovered with a smaller color difference and better visual quality than the CFA images obtained by the fixed sensitivity function. At low SNR, the optimized sensitivity functions

well balanced the color reproduction accuracy and noise amplification in the color transformation. As a consequence, it is possible to have a camera with tunable sensitivity functions for different shooting conditions to improve the image quality.

Some practical issues remain in our optimization which are required to be investigated further. There are multiple noise sources in digital cameras. Other than the Gaussian independent noise, the signal-dependent noise in cameras follows the Poisson distribution. Signal-dependent noise affects the multispectral imaging model and the method of formulating the multichannel Wiener filter since the uncorrelated assumption may not be valid. Also, we achieved a linear minimum-mean-squared solution in the optimization by using the Wiener filter. However, nonlinear algorithms are generally used in the reconstruction of real cameras. Nonlinear denoising and demosaicking algorithms may change the optimal sensitivity functions. More comprehensive simulations and experiments have to be performed to reduce errors caused by the linear model.

(a) True sRGB image

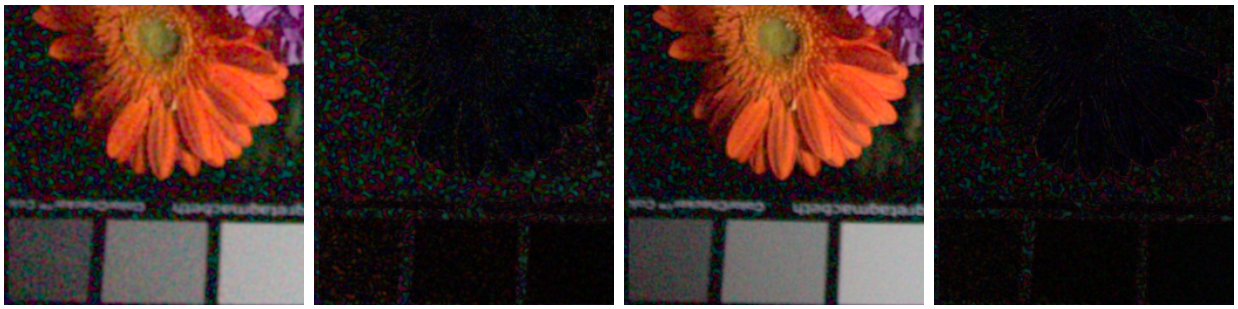

(b) Fixed (10 dB) (c) Fixed diff. (10 dB) (d) Fixed (15 dB) (e) Fixed diff. (15 dB)

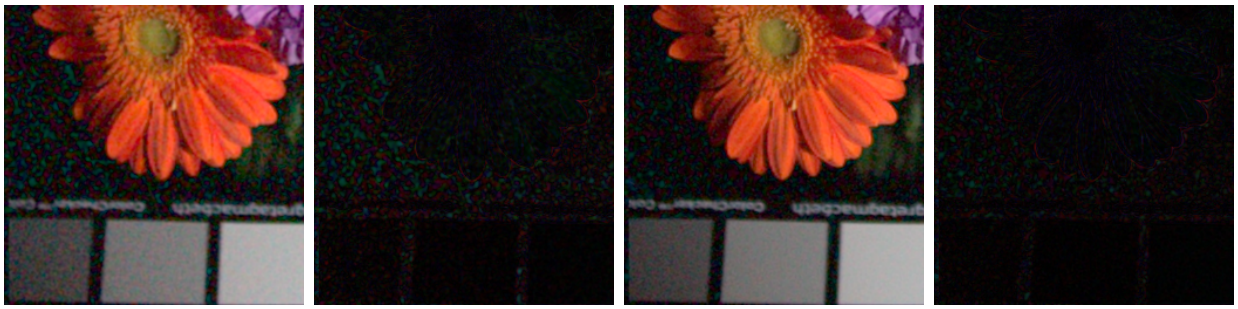

(f) Optimal (10 dB) (g) Optimal diff. (10 dB) (h) Optimal (15 dB) (i) Optimal diff. (15 dB)

Figure 5.13: The reconstructed full-color images with difference images of No. 1 multispectral images in the sRGB color space: (b)–(e) the results using the fixed sensitivity functions; (f)–(i) the results using the optimal sensitivity functions. The SNRs are 10 dB and 15 dB:

(a) True sRGB image

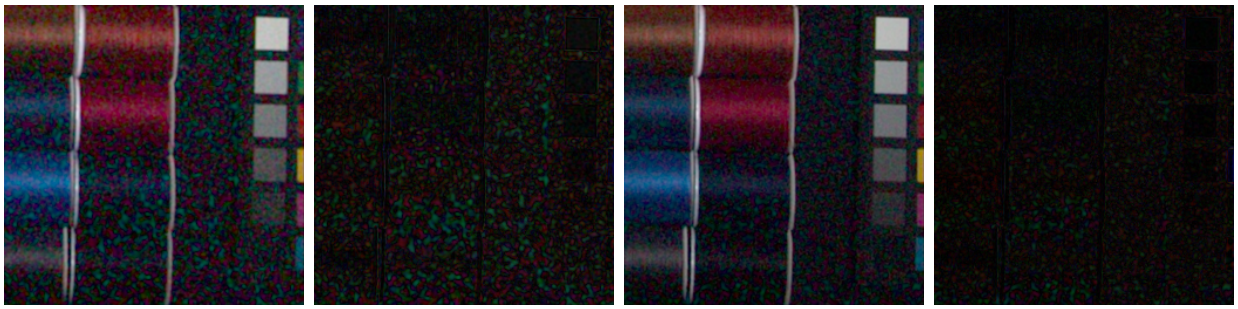

(b) Fixed (10 dB) (c) Fixed diff. (10 dB) (d) Fixed (15 dB) (e) Fixed diff. (15 dB)

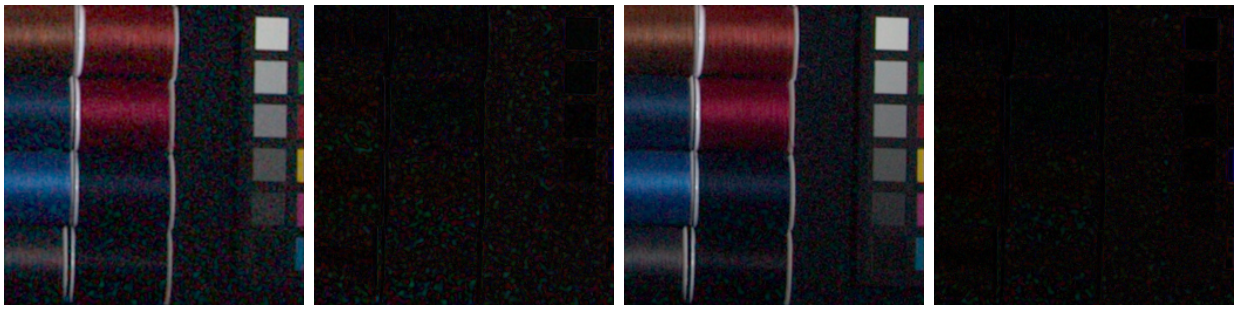

(f) Optimal (10 dB) (g) Optimal diff. (10 dB) (h) Optimal (15 dB) (i) Optimal diff. (15 dB)

Figure 5.14: The reconstructed full-color images with difference images of No. 5 multispectral images in the sRGB color space: (b)–(e) the results using the fixed sensitivity functions; (f)–(i) the results using the optimal sensitivity functions. The SNRs are 10 dB and 15 dB.

Chapter 6

Summary

6.1 Summary of Results

A digital camera is a complicated imaging system in which both hardware and software components work together to acquire images. For a long time, developers concentrated on improving the optical image obtained by the traditional optical parts of cameras with image processing techniques. By including both the optical and image reconstruction problems in a single design framework, we exploit the ability of common image reconstruction techniques to assist the system-level design of cameras. This design methodology described in this dissertation can be extended to other parts of the image acquisition pipeline.

An adaptive image acquisition approach is first introduced in Chapter 3. A new imaging model of defocusing acquisition is defined that considers both aliasing and noise. A criterion to estimate the optimal focus setting for a specific scene is derived. The model-based Wiener filter is used to minimize the end-to-end reconstruction error during the acquisition. Both the Wiener filter and the criterion are adapted to the power spectrum of the input scene. Numerical and visual results show that the proposed approach outperforms traditional acquisition methods with or without a fixed anti-aliasing filter. The proposed approach is robust with respect to various noise levels, and it is practical in some cases to replace the commonly used four-spot birefringent filter with this method.

The extension of defocusing acquisition to single-sensor color cameras is presented in Chapter 4. The CFA used in such a camera makes the reconstruction a joint demosaicking and deconvolution problem. An imaging model built on the modulated LC_1C_2 domain dramatically suppresses the cross-channel correlation among RGB channels. As a consequence, the multichannel Wiener filter and the error criterion are simplified without the need to

account for these correlations. We presented results that are an improvement over a traditional anti-aliasing filter. Our approach includes a postprocessing joint deblurring and demosaicking step. The error criterion to determine the optimal defocus setting is accurate for different scenes and noise levels.

In Chapter 5, an optimization of camera sensor sensitivity functions was introduced. A multichannel Wiener filter was designed to minimize the color difference between the image captured by the camera and the true image in the CIELAB color space. We optimized the green sensitivities for different noise levels after determining the sensitivity functions of the red and blue channels. Simulation results show that the images captured with the optimal sensitivity functions outperform the images captured with the fixed sensitivity functions in terms of the color difference and visual quality.

6.2 Future Directions

A number of practical issues in this research are unresolved. In Chapter 3 and 4, we chose a circular blur to approximate the out-of-focus blur generated by a camera lens. However, the optical transfer function of the camera lens is much more complicated and is not shift-invariant in general. A comprehensive characterization of the response of the real out-of-focus blur is required to generate more accurate results by the defocusing approach. In color defocusing acquisition, the response of out-of-focus is different in each color channel. This difference generates chromatic aberration in the acquired images which requires a post-processing step to correct.

The defocusing acquisition approach relies on the incorporation with the autofocus system of a camera. Most autofocus systems use multiple separate optical sensors to find the optimal focus point for the camera. These sensors measure the region of interest in the scene. Using autofocus sensors to search the optimal defocus setting rather than the main optical sensor is more feasible for this approach. A possible speedup of the defocusing

algorithm can be accomplished. Also, a front focus or a back focus can generate the same amount of out-of-focus blur. The choice from these two is required for real applications.

The optimization of sensitivity functions introduced in Chapter 5 also has some open areas. We only derived the methodology to optimize the sensor with a Bayer CFA. A general optimization for a two-by-two CFA pattern with four color channels can be derived using a similar approach. A two-by-four or four-by-two CFA pattern optimization increases the complexity of this algorithm but also increases the design flexibility. The choice of the spatial sampling pattern is an important area for future research.

The choice of the measurement noise model should be investigate more in future research. White Gaussian noise is assumed in most of this research. Although a signal-dependent noise model was chosen in Chapter 3, the variance of the dependent part is small. However, only amplifier noise in digital cameras can be modeled by Gaussian noise. The photon shot noise, which follows a Poisson distribution, is the major noise source in the bright region of the image. Future research should include the photon shot noise model which makes it more applicable for digital cameras.

Bibliography

[1] R. Ramanath, W. Snyder, Y. Yoo, and M. Drew, "Color image processing pipeline," *IEEE Signal Processing Magazine*, vol. 22, no. 1, pp. 34–43, Jan. 2005.

[2] N. Kehtarnavaz, H.-J. Oh, and Y. Yoo, "Development and real-time implementation of auto white balancing scoring algorithm," *Real-Time Imaging*, vol. 8, no. 5, pp. 379–386, 2002.

[3] K. Barnard, V. Cardei, and B. Funt, "A comparison of computational color constancy algorithms. I: Methodology and experiments with synthesized data," *IEEE Transactions on Image Processing*, vol. 11, no. 9, pp. 972–984, Sep. 2002.

[4] J.-Y. Huo, Y.-L. Chang, J. Wang, and X.-X. Wei, "Robust automatic white balance algorithm using gray color points in images," *Consumer Electronics, IEEE Transactions on*, vol. 52, no. 2, pp. 541–546, May. 2006.

[5] D. Alleysson, S. Süsstrunk, and J. Marguier, "Influence of spectral sensitivity functions on color demosaicing," in *Proceedings IS&T/SID 11th Color Imaging Conference*, vol. 11, 2003, pp. 351–357.

[6] K. Hirakawa and P. J. Wolfe, "Spatio-spectral color filter array design for enhanced image fidelity," in *IEEE International Conference on Image Processing*, vol. 2, Sep. 2007.

[7] L. Condat, "A new color filter array with optimal properties for noiseless and noisy color image acquisition," *IEEE Transactions on Image Processing*, vol. 20, no. 8, pp. 2200–2210, Aug. 2011.

[8] *Multimedia Systems and Equipment—Colour Measurement and Management—Part 2-1: Colour Management—Default RGB Colour Space - sRGB*, International Electrotechnical Commission Std. IEC 61 966-2-1 ed1.0, 1999.

[9] *JPEG2000 Image Coding System*, ISO/IEC Std. 15 444-1, 2000.

[10] L. Zhang, X. Wu, and D. Zhang, "Color reproduction from noisy CFA data of single sensor digital cameras," *IEEE Transactions on Image Processing*, vol. 16, no. 9, pp. 2184–2197, Sep. 2007.

[11] M. D. Robinson and D. G. Stork, "Joint design of lens systems and digital image processing," in *Proceedings of SPIE*, vol. 6342. SPIE, 2006, p. 63421G.

[12] M. Vrhel and H. Trussell, "Color filter selection for color correction in the presence of noise," in *IEEE International Conference on Acoustics, Speech, and Signal Processing*, vol. 5, 1993, pp. 313–316.

[13] M. Wolski, C. Bouman, J. Allebach, and E. Walowit, "Optimization of sensor response functions for colorimetry of reflective and emissive objects," in *IEEE International Conference on Image Processing*, vol. 2, Oct. 1995, pp. 323–326.

[14] N. Shimano, "Optimization of spectral sensitivities with gaussian distribution functions for a color image acquisition device in the presence of noise," *Optical Engineering*, vol. 45, p. 013201, 2006.

[15] M. Parmar and S. Reeves, "Selection of optimal spectral sensitivity functions for color filter arrays," *IEEE Transactions on Image Processing*, vol. 19, no. 12, pp. 3190–3203, Dec. 2010.

[16] J. W. Evans, "The birefringent filter," *J. Opt. Soc. Am.*, vol. 39, no. 3, pp. 229–237, Mar. 1949.

[17] D. Kessler, A. C. G. Nutt, and R. J. Palum, "Anti-aliasing low-pass blur filter for reducing artifacts in imaging apparatus," US Patent 6 937 283, 2005.

[18] J. W. Evans, "Solc birefringent filter," *J. Opt. Soc. Am.*, vol. 48, no. 3, pp. 142–143, Mar. 1958.

[19] J. Katzenstein, "New type of birefringent filter," *J. Opt. Soc. Am.*, vol. 58, no. 10, pp. 1348–1355, Oct. 1968.

[20] R. H. Chu and G. Town, "Birefringent filter synthesis by use of a digital filter design algorithm," *Appl. Opt.*, vol. 41, no. 17, pp. 3412–3418, Jun. 2002.

[21] A. Stockman, D. I. A. MacLeod, and N. E. Johnson, "Spectral sensitivities of the human cones," *J. Opt. Soc. Am. A*, vol. 10, no. 12, pp. 2491–2521, 1993.

[22] B. E. Bayer, "Color imaging array," U.S. Patent 3 971 065, Jul., 1976.

[23] S. Yamanaka, "Solid state color camera," U.S. Patent 4 054 906, 1977.

[24] R. Lukac and K. N. Plataniotis, "Color filter arrays: Design and performance analysis," *IEEE Transactions on Consumer Electronics*, vol. 51, no. 4, pp. 1260–1267, Nov. 2005.

[25] T. Kijima, H. Nakamura, J. T. Compton, and J. F. Hamilton, "Image sensor with improved light sensitivity," Unite States Patent 20 070 177 236, 2007.

[26] K. Hirakawa and P. J. Wolfe, "Second-generation color filter array and demosaicking designs," in *Proceedings of SPIE*, vol. 6822, no. 1, 2008, p. 68221P.

[27] D. B. Gennery, "Determination of optical transfer function by inspection of frequency-domain plot," *J. Opt. Soc. Am.*, vol. 63, no. 12, pp. 1571–1577, Dec. 1973.

[28] D. Kundur and D. Hatzinakos, "Blind image deconvolution," *IEEE Signal Processing Magazine*, vol. 13, no. 3, pp. 43–64, 1996.

[29] R. L. Lagendijk, J. Biemond, and D. E. Boekee, "Identification and restoration of noisy blurred images using the expectation-maximization algorithm," *IEEE Transactions on Acoustics, Speech and Signal Processing*, vol. 38, no. 7, pp. 1180–1191, July 1990.

[30] S. J. Reeves and R. M. Mersereau, "Blur identification by the method of generalized cross-validation," *IEEE Transactions on Image Processing*, vol. 1, no. 3, pp. 301–311, Jul. 1992.

[31] T. G. Stockham, Jr., T. M. Cannon, and R. B. Ingebretsen, "Blind deconvolution through digital signal processing," *Proceedings of the IEEE*, vol. 63, no. 4, pp. 678–692, Apr. 1975.

[32] Y.-L. You and M. Kaveh, "A regularization approach to joint blur identification and image restoration," *IEEE Transactions on Image Processing*, vol. 5, no. 3, pp. 416–428, 1996.

[33] V. Katkovnik, K. Egiazarian, and J. Astola, "A spatially adaptive nonparametric regression image deblurring," *IEEE Transactions on Image Processing*, vol. 14, no. 10, pp. 1469–1478, Oct. 2005.

[34] F. Chen, X. Huang, and W. Chen, "Texture-preserving image deblurring," *IEEE Signal Processing Letters*, vol. 17, no. 12, pp. 1018–1021, Dec. 2010.

[35] C. Tomasi and R. Manduchi, "Bilateral filtering for gray and color images," in *ICCV 1998: Proceedings of the Sixth International Conference on Computer Vision*. Washington, DC, USA: IEEE Computer Society, 1998, p. 839.

[36] D. Menon and G. Calvagno, "Regularization approaches to demosaicking," *IEEE Transactions on Image Processing*, vol. 18, no. 10, pp. 2209–2220, Oct. 2009.

[37] X. Li, B. Gunturk, and L. Zhang, "Image demosaicing: A systematic survey," in *Proceedings of SPIE*, vol. 6822, 2008, p. 68221J.

[38] R. Kimmel, "Demosaicing: Image reconstruction from color CCD samples," *IEEE Transactions on Image Processing*, vol. 8, no. 9, pp. 1221–1228, Sep. 1999.

[39] C. W. Kim and M. G. Kang, "Noise insensitive high resolution demosaicing algorithm considering cross-channel correlation," in *Image Processing, 2005. ICIP 2005. IEEE International Conference on*, vol. 3, Sep. 2005, pp. 1100–1103.

[40] X. Wu and N. Zhang, "Primary-consistent soft-decision color demosaicking for digital cameras (patent pending)," *IEEE Transactions on Image Processing*, vol. 13, no. 9, pp. 1263–1274, Sep. 2004.

[41] L. Zhang and X. Wu, "Color demosaicking via directional linear minimum mean square-error estimation," *IEEE Transactions on Image Processing*, vol. 14, no. 12, pp. 2167–2178, Dec. 2005.

[42] D. R. Cok, "Signal processing method and apparatus for producing interpolated chrominance values in a sampled color image signal," U.S. Patent 4 642 678, 1987.

[43] C. A. Laroche and M. A. Prescott, "Apparatus and method for adaptively interpolating a full color image utilizing chrominance gradients," U.S. Patent 5 373 322, 1994.

[44] J. E. Adams and J. F. Hamilton, "Adaptive color plane interpolation in single sensor color electronic camera," U.S. Patent 5 652 621, Apr, 1997.

[45] K.-H. Chung and Y.-H. Chan, "Color demosaicing using variance of color differences," *IEEE Transactions on Image Processing*, vol. 15, no. 10, pp. 2944–2955, Oct. 2006.

[46] C.-Y. Su, "Highly effective iterative demosaicing using weighted-edge and color-difference interpolations," *IEEE Transactions on Consumer Electronics*, vol. 52, no. 2, pp. 639–645, May 2006.

[47] A. Buades, B. Coll, J. M. Morel, and C. Sbert, "Self-similarity driven color demosaicking," *IEEE Transactions on Image Processing*, vol. 18, no. 6, pp. 1192–1202, Jun. 2009.

[48] A. Buades, B. Coll, and J. M. Morel, "A review of image denoising algorithms, with a new one," *Multiscale Modeling & Simulation*, vol. 4, no. 2, pp. 490–530, 2005.

[49] K. Hirakawa and T. W. Parks, "Adaptive homogeneity-directed demosaicing algorithm," *IEEE Transactions on Image Processing*, vol. 14, no. 3, pp. 360–369, Mar. 2005.

[50] B. K. Gunturk, Y. Altunbasak, and R. M. Mersereau, "Color plane interpolation using alternating projections," *IEEE Transactions on Image Processing*, vol. 11, no. 9, pp. 997–1013, Sep. 2002.

[51] S. Ferradans, M. Bertalmio, and V. Caselles, "Geometry-based demosaicking," *IEEE Transactions on Image Processing*, vol. 18, no. 3, pp. 665–670, Mar. 2009.

[52] J. Mairal, M. Elad, and G. Sapiro, "Sparse representation for color image restoration," *IEEE Transactions on Image Processing*, vol. 17, no. 1, pp. 53–69, Jan. 2008.

[53] J. W. Glotzbach, R. W. Schafer, and K. Illgner, "A method of color filter array interpolation with alias cancellation properties," in *Image Processing, 2001 International Conference on*, vol. 1, Thessaloniki, Greece, 2001, pp. 141–144.

[54] D. Alleysson, S. Ssstrunk, and J. Hrault, "Color demosaicing by estimating luminance and opponent chromatic signals in the fourier domain," in *IS&T/SID 10th Color Imaging Conference*, vol. 10, 2002, pp. 331–336.

[55] D. Alleysson, S. Susstrunk, and J. Herault, "Linear demosaicing inspired by the human visual system," *IEEE Transactions on Image Processing*, vol. 14, no. 4, pp. 439–449, Apr. 2005.

[56] N.-X. Lian, L. Chang, Y.-P. Tan, and V. Zagorodnov, "Adaptive filtering for color filter array demosaicking," *IEEE Transactions on Image Processing*, vol. 16, no. 10, pp. 2515–2525, Oct. 2007.

[57] E. Dubois, "Frequency-domain methods for demosaicking of bayer-sampled color images," *IEEE Signal Processing Letters*, vol. 12, no. 12, pp. 847–850, Dec. 2005.

[58] ——, "Filter design for adaptive frequency-domain Bayer demosaicking," in *Image Processing, 2006 IEEE International Conference on*, Oct. 2006, pp. 2705–2708.

[59] H. G. Grassmann, "Zur theorie der farbenmischung," *Annalen Phys. Chemie*, vol. 89, pp. 69–84, 1853.

[60] W. D. Wright, "A re-determination of the trichromatic coefficients of the spectral colours," *Transactions of the Optical Society*, vol. 30, pp. 141–164, 1928.

[61] J. Guild, "The colorimetric properties of the spectrum," *Philosophical Transactions of the Royal Society of London*, vol. 230, pp. 149–187, 1931.

[62] X. Zhang and B. A. Wandell, "A spatial extension of CIELAB for digital color-image reproduction," *Journal of the Society for Information Display*, vol. 5, no. 1, pp. 61–63, 1997.

[63] B. F. Lyot, "Un monochromateur à grand champ itilisant les interfererces en lumiere polarisée," *Comptes Rendus de l'Académie des Sciences*, vol. 197, p. 1593, 1933.

[64] M. Sato, S. Nagahara, and K. Takahashi, "Optical filter for color imaging device," U.S. Patent 4 626 897, 1986.

[65] T. Ma and S. J. Reeves, "Adaptive image acquisition by autodefocusing," *Journal of Electronic Imaging*, vol. 20, p. 033013, 2011.

[66] A. V. Oppenheim, A. S. Willsky, and S. H. Nawab, *Signals and Systems (2nd Edition)*. Prentice Hall, 1997.

[67] K. Hirakawa and T. Parks, "Image denoising using total least squares," *IEEE Transactions on Image Processing*, vol. 15, no. 9, pp. 2730–2742, Sep. 2006.

[68] A. K. Jain, *Fundamentals of Digital Image Processing*. Prentice Hall, 1989.

[69] J. Shi and S. E. Reichenbach, "Image interpolation by two-dimensional parametric cubic convolution," *IEEE Transactions on Image Processing*, vol. 15, no. 7, pp. 1857–1870, 2006.

[70] ——, "Spatially constrained Wiener filter with Markov autocorrelation modeling for image resolution enhancement," in *2006 IEEE International Conference on Image Processing*, Oct. 2006, pp. 2681–2684.

[71] Eastman Kodak, "PhotoCD PCD0992," http://r0k.us/graphics/kodak.

[72] E. C. Larson and D. M. Chandler, "Most apparent distortion: Full-reference image quality assessment and the role of strategy," *Journal of Electronic Imaging*, vol. 19, no. 1, p. 011006, 2010.

[73] P. Le Callet and F. Autrusseau, "Subjective quality assessment IRCCyN/IVC database," 2005, http://www.irccyn.ec-nantes.fr/ivcdb/.

[74] Z. Wang, A. Bovik, H. Sheikh, and E. Simoncelli, "Image quality assessment: From error visibility to structural similarity," *IEEE Transactions on Image Processing*, vol. 13, no. 4, pp. 600–612, Apr. 2004.

[75] M. Sakano, N. Suetake, and E. Uchino, "A robust point spread function estimation for out-of-focus blurred and noisy images based on a distribution of gradient vectors on the polar plane," *Optical Review*, vol. 14, pp. 297–303, 2007.

[76] R. Prendergast and T. Nguyen, "A novel parametric power spectral density model for images," in *Signals, Systems and Computers, 2005. Conference Record of the Thirty-Ninth Asilomar Conference on*, Nov. 2005, pp. 1671–1675.

[77] T. Ma and S. Reeves, "An iterative regularization approach for color filter array image restoration," in *Industrial Technology (ICIT), 2011 IEEE International Conference on*, Mar. 2011, pp. 332–335.

[78] H. Kuniba and R. S. Berns, "Spectral sensitivity optimization of color image sensors considering photon shot noise," *Journal of Electronic Imaging*, vol. 18, p. 023002, 2009.

[79] [Online]. Available: http://gene.bio.jhu.edu/violet/violet.html

[80] R. Ramanath, W. Snyder, G. Bilbro, and W. Sander III, "Demosaicking methods for bayer color arrays," *Journal of Electronic Imaging*, vol. 11, p. 306, 2002.

[81] D. Alleysson and B. C. de Lavarène, "Frequency selection demosaicking: A review and a look ahead," in *Proceedings of SPIE*, vol. 6822, no. 1, 2008, p. 68221M.

[82] K. Hirakawa and P. J. Wolfe, "Spatio-spectral color filter array design for optimal image recovery," *IEEE Transactions on Image Processing*, vol. 17, no. 10, pp. 1876–1890, Oct. 2008.

[83] U. Barnhöefer, J. M. DiCarlo, B. Olding, and B. A. Wandell, "Color estimation error trade-offs," *Proceedings of SPIE*, vol. 5017, no. 650, pp. 263–273, 2003.

[84] P. Vora, J. Farrell, J. Tietz, and D. Brainard, "Image capture: simulation of sensor responses from hyperspectral images," *IEEE Transactions on Image Processing*, vol. 10, no. 2, pp. 307–316, Feb. 2001.

[85] N. Gat, "Imaging spectroscopy using tunable filters: a review," in *Proc. SPIE 4056*, 2000, p. 50.

[86] B. E. Bagwell, D. V. Wick, R. Batchko, J. D. Mansell, T. Martinez, S. R. Restaino, D. M. Payne, J. Harriman, S. Serati, G. Sharp, and J. Schwiegerling, "Liquid crystal based active optics," in *Proc. SPIE 6289*, 2006, p. 628908.

[87] M. W. Miles, "Visible spectrum modulator arrays," U.S. Patent 5 835 255, May 10, 1998.

[88] D.-Y. Ng and J. Allebach, "A subspace matching color filter design methodology for a multispectral imaging system," *IEEE Transactions on Image Processing*, vol. 15, no. 9, pp. 2631–2643, Sep. 2006.

[89] G. Wyszecki and W. S. Stiles, *Color Science: Concepts and Methods, Quantitative Data and Formulae, 2nd Edition.* John Wiley & Sons, Inc., 1989.

[90] M. Vrhel and H. Trussell, "Filter considerations in color correction," *IEEE Transactions on Image Processing*, vol. 3, no. 2, pp. 147–161, Mar. 1994.

[91] P. Vora and H. Trussell, "Mathematical methods for the analysis of color scanning filters," *IEEE Transactions on Image Processing*, vol. 6, no. 2, pp. 321–327, Feb. 1997.

[92] [Online]. Available: http://www.cis.rit.edu/mcsl/online/cie.php

[93] [Online]. Available: http://en.wikipedia.org/wiki/CIE_1931_color_space

[94] F. Yasuma, T. Mitsunaga, D. Iso, and S. Nayar, "Generalized assorted pixel camera: Post-capture control of resolution, dynamic range and spectrum," Columbia University, Tech. Rep., Nov. 2008.

Appendices

Appendix A

2D DFT matrix

To define a two-dimensional DFT matrix, two one-dimensional DFT matrices for each direction (horizontal and vertical) are defined as follows:

$$\mathcal{F}_m = \frac{1}{\sqrt{m}} \begin{bmatrix} 1 & 1 & \cdots & 1 \\ 1 & \omega_m^1 & \cdots & \omega_m^{m-1} \\ \vdots & \vdots & \ddots & \vdots \\ 1 & \omega_m^{m-1} & \cdots & \omega_m^{(m-1)(m-1)} \end{bmatrix},$$

and

$$\mathcal{F}_n = \frac{1}{\sqrt{n}} \begin{bmatrix} 1 & 1 & \cdots & 1 \\ 1 & \omega_n^1 & \cdots & \omega_n^{n-1} \\ \vdots & \vdots & \ddots & \vdots \\ 1 & \omega_n^{n-1} & \cdots & \omega_n^{(n-1)(n-1)} \end{bmatrix},$$

where $\omega_m = e^{-j\frac{2\pi}{m}}$ and $\omega_n = e^{-j\frac{2\pi}{n}}$. The 2D DFT matrix is a Kronecker product of $\mathcal{F}_m$ and $\mathcal{F}_n$. The order of the Kronecker product depends on the method of constructing the image vector. For example, if the image vector is formed with column order, the 2D DFT matrix has the following structure:

$$\mathcal{F}_{mn} = \mathcal{F}_n \otimes \mathcal{F}_m$$

$$= \frac{1}{\sqrt{mn}} \begin{bmatrix} \mathcal{F}_m & \mathcal{F}_m & \cdots & \mathcal{F}_m \\ \mathcal{F}_m & \omega_n^1 \mathcal{F}_m & \cdots & \omega_n^{n-1} \mathcal{F}_m \\ \vdots & \vdots & \ddots & \vdots \\ \mathcal{F}_m & \omega_n^{n-1} \mathcal{F}_m & \cdots & \omega_n^{(n-1)(n-1)} \mathcal{F}_m \end{bmatrix}$$

$$= \frac{1}{\sqrt{mn}} \begin{bmatrix} 1 & 1 & \cdots & 1 & \cdots & \cdots & 1 & 1 & \cdots & 1 \\ 1 & \omega_m^1 & \cdots & \omega_m^{m-1} & \cdots & \cdots & 1 & \omega_m^1 & \cdots & \omega_m^{m-1} \\ \vdots & \vdots & \ddots & \vdots & & & \vdots & \vdots & \ddots & \vdots \\ 1 & \omega_m^{m-1} & \cdots & \omega_m^{(m-1)(m-1)} & \cdots & \cdots & 1 & \omega_m^{m-1} & \cdots & \omega_m^{(m-1)(m-1)} \\ \vdots & \vdots & & \vdots & \ddots & & \vdots & \vdots & & \vdots \\ \vdots & \vdots & & \vdots & & \ddots & \vdots & \vdots & & \vdots \\ 1 & 1 & \cdots & 1 & \cdots & \cdots & \omega_n^{(n-1)(n-1)} & \omega_n^{(n-1)(n-1)} & \cdots & \omega_n^{(n-1)(n-1)} \\ 1 & \omega_m^1 & \cdots & \omega_m^{m-1} & \cdots & \cdots & \omega_n^{(n-1)(n-1)} & \omega_n^{(n-1)(n-1)} \omega_m^1 & \cdots & \omega_n^{(n-1)(n-1)} \omega_m^{m-1} \\ \vdots & \vdots & \ddots & \vdots & & & \vdots & \vdots & \ddots & \vdots \\ 1 & \omega_m^{m-1} & \cdots & \omega_m^{(m-1)(m-1)} & \cdots & \cdots & \omega_n^{(n-1)(n-1)} & \omega_n^{(n-1)(n-1)} \omega_m^{m-1} & \cdots & \omega_n^{(n-1)(n-1)} \omega_m^{(m-1)(m-1)} \end{bmatrix}.$$

Appendix B

Structure of Matrix K

We define four linear transformations for four color channels in the Bayer CFA images as: $T_r = \mathcal{F}_s D_r \mathcal{F}_b^H$, $T_{g_1} = \mathcal{F}_s D_{g_1} \mathcal{F}_b^H$, $T_{g_2} = \mathcal{F}_s D_{g_2} \mathcal{F}_b^H$ and $T_b = \mathcal{F}_s D_b \mathcal{F}_b^H$, where $\mathcal{F}_b \in \mathbb{R}^{mn \times mn}$ and $\mathcal{F}_s \in \mathbb{R}^{mn/4 \times mn/4}$ are 2D DFT matrices. The matrix K can be expressed as follows:

$$K = \begin{bmatrix} T_r S T_r^H & T_r S T_{g_1}^H & T_r S T_{g_2}^H & T_r S T_b^H \\ T_{g_1} S T_r^H & T_{g_1} S T_{g_1}^H & T_{g_1} S T_{g_2}^H & T_{g_1} S T_b^H \\ T_{g_2} S T_r^H & T_{g_2} S T_{g_1}^H & T_{g_2} S T_{g_2}^H & T_{g_2} S T_b^H \\ T_b S T_r^H & T_b S T_{g_1}^H & T_b S T_{g_2}^H & T_b S T_b^H \end{bmatrix}, \tag{B.1}$$

where the diagonal matrix $S \in \mathbb{R}^{mn \times mn}$ is of the form: $S = \text{diag}[s_1, s_2, \cdots, s_{mn}]$. Since the sampling matrices D_r, D_{g_1}, D_{g_2} and D_b are separable, one can describe them using the Kronecker product of two one-dimensional downsampling matrices as follows:

$$\begin{cases} D_r = D_{2n} \otimes D_{1m} \\ D_{g_1} = D_{1n} \otimes D_{1m} \\ D_{g_2} = D_{2n} \otimes D_{2m} \\ D_b = D_{1n} \otimes D_{2m} \end{cases} \tag{B.2}$$

For the images captured by the Bayer CFA pattern, the 1-D downsampling matrices $D_{1m} \in \mathbb{R}^{m/2\times m}$ and $D_{1n} \in \mathbb{R}^{n/2\times n}$ are of the following form:

$$\begin{bmatrix} 1 & 0 & 0 & 0 & \cdots & 0 & 0 \\ 0 & 0 & 1 & 0 & \cdots & 0 & 0 \\ \vdots & \vdots & \vdots & \vdots & \ddots & \vdots & \vdots \\ 0 & 0 & 0 & 0 & \cdots & 1 & 0 \end{bmatrix}. \tag{B.3}$$

Similarly, the structure of downsampling matrice $D_{2m} \in \mathbb{R}^{m/2\times m}$ and $D_{2n} \in \mathbb{R}^{n/2\times n}$ are given by the following form:

$$\begin{bmatrix} 0 & 1 & 0 & 0 & \cdots & 0 & 0 \\ 0 & 0 & 0 & 1 & \cdots & 0 & 0 \\ \vdots & \vdots & \vdots & \vdots & \ddots & \vdots & \vdots \\ 0 & 0 & 0 & 0 & \cdots & 0 & 1 \end{bmatrix}. \tag{B.4}$$

Since the 2D DFT matrices are separable, one can apply the mixed-product property of the Kronecker product to express each of the four linear transformations T_r, T_{g1}, T_{g2} and T_b using the row and column transformations. For example, the transformation of red channel T_r can be rewritten as follows:

$$\begin{aligned} T_r &= F_s D_r F_b^H \\ &= (\mathcal{F}_{n/2} \otimes \mathcal{F}_{m/2})(D_{2n} \otimes D_{1m})(\mathcal{F}_n^H \otimes \mathcal{F}_m^H) \\ &= (\mathcal{F}_{n/2} D_{2n} \mathcal{F}_n^H) \otimes (\mathcal{F}_{m/2} D_{1m} \mathcal{F}_m^H). \end{aligned} \tag{B.5}$$

Denote $T_{rn} = \mathcal{F}_{n/2} D_{2n} \mathcal{F}_n^H$ and $T_{rm} = \mathcal{F}_{m/2} D_{1m} \mathcal{F}_m^H$. It is straightforward to show that they are both sparse matrices with the following forms:

$$
\begin{aligned}
T_{rn} &= \frac{n}{2} \begin{bmatrix} 1 & & & & e^{j\frac{2\pi}{n}(\frac{n}{2})} & & & \\ & e^{j\frac{2\pi}{n}} & & & & e^{j\frac{2\pi}{n}(\frac{n}{2}+1)} & & \\ & & \ddots & & & & \ddots & \\ & & & e^{j\frac{2\pi}{n}(\frac{n}{2}-1)} & & & & e^{j\frac{2\pi}{n}(n-1)} \end{bmatrix}_{\frac{n}{2}\times n}, \\
T_{rm} &= \frac{m}{2} \begin{bmatrix} 1 & & 1 & & \\ & 1 & & 1 & \\ & & \ddots & & \ddots \\ & & 1 & & 1 \end{bmatrix}_{\frac{m}{2}\times m}.
\end{aligned}
\tag{B.6}
$$

One can derive similar matrices for the other three linear transformations. We list them here for reference. For the blue channel transformation $T_b = T_{bn} \otimes T_{bm}$, the two matrices T_{bn} and T_{bm} have the following forms:

$$
\begin{aligned}
T_{bn} &= \frac{n}{2} \begin{bmatrix} 1 & & 1 & & \\ & 1 & & 1 & \\ & & \ddots & & \ddots \\ & & 1 & & 1 \end{bmatrix}_{\frac{n}{2}\times n}, \\
T_{bm} &= \frac{m}{2} \begin{bmatrix} 1 & & & & e^{j\frac{2\pi}{m}(\frac{m}{2})} & & & \\ & e^{j\frac{2\pi}{m}} & & & & e^{j\frac{2\pi}{m}(\frac{m}{2}+1)} & & \\ & & \ddots & & & & \ddots & \\ & & & e^{j\frac{2\pi}{m}(\frac{m}{2}-1)} & & & & e^{j\frac{2\pi}{m}(m-1)} \end{bmatrix}_{\frac{m}{2}\times m}.
\end{aligned}
\tag{B.7}
$$

For the green1 channel transformation $T_{g_1} = T_{g_1 n} \otimes T_{g_1 m}$, the two matrices $T_{g_1 n}$ and $T_{g_1 m}$ can be described as follows:

$$
\begin{aligned}
T_{g_1 n} &= \frac{n}{2} \begin{bmatrix} 1 & & & 1 & & \\ & 1 & & & 1 & \\ & & \ddots & & & \ddots \\ & & & 1 & & 1 \end{bmatrix}_{\frac{n}{2} \times n}, \\
T_{g_1 m} &= \frac{m}{2} \begin{bmatrix} 1 & & & 1 & & \\ & 1 & & & 1 & \\ & & \ddots & & & \ddots \\ & & & 1 & & 1 \end{bmatrix}_{\frac{m}{2} \times m}.
\end{aligned}
\tag{B.8}
$$

Finally, for the green2 channel transformation $T_{g_2} = T_{g_2 n} \otimes T_{g_2 m}$, one can express the two matrices $T_{g_2 n}$ and $T_{g_2 m}$ as follows:

$$
\begin{aligned}
T_{g_2 n} &= \frac{n}{2} \begin{bmatrix} 1 & & & e^{j\frac{2\pi}{n}(\frac{n}{2})} & & \\ & e^{j\frac{2\pi}{n}} & & & e^{j\frac{2\pi}{n}(\frac{n}{2}+1)} & \\ & & \ddots & & & \ddots \\ & & & e^{j\frac{2\pi}{n}(\frac{n}{2}-1)} & & e^{j\frac{2\pi}{n}(n-1)} \end{bmatrix}_{\frac{n}{2} \times n}, \\
T_{g_2 m} &= \frac{m}{2} \begin{bmatrix} 1 & & & e^{j\frac{2\pi}{m}(\frac{m}{2})} & & \\ & e^{j\frac{2\pi}{m}} & & & e^{j\frac{2\pi}{m}(\frac{m}{2}+1)} & \\ & & \ddots & & & \ddots \\ & & & e^{j\frac{2\pi}{m}(\frac{m}{2}-1)} & & e^{j\frac{2\pi}{m}(m-1)} \end{bmatrix}_{\frac{m}{2} \times m}.
\end{aligned}
\tag{B.9}
$$

The diagonal elements of blocks K_{ij}, $i, j = r, g_1, g_2, b$, can be acquired by a direct matrix multiplication. In particular, the diagonal elements of blocks K_{rr}, $K_{g_1 g_1}$, $K_{g_2 g_2}$ and K_{bb} are

as follows:

$$
\begin{cases}
k_1 & = s_1 + s_{\frac{m}{2}+1} + s_{\frac{mn}{2}+1} + s_{\frac{mn}{2}+\frac{m}{2}+1} \\
k_2 & = s_2 + s_{\frac{m}{2}+2} + s_{\frac{mn}{2}+2} + s_{\frac{mn}{2}+\frac{m}{2}+2} \\
\vdots & \\
k_{\frac{m}{2}} & = s_{\frac{m}{2}} + s_m + s_{\frac{mn}{2}+\frac{m}{2}} + s_{\frac{mn}{2}+m} \\
k_{\frac{m}{2}+1} & = s_{m+1} + s_{m+\frac{m}{2}+1} + s_{\frac{mn}{2}+m+1} + s_{\frac{mn}{2}+m+\frac{m}{2}+1} \\
\vdots & \\
k_m & = s_{m+\frac{m}{2}} + s_{2m} + s_{\frac{mn}{2}+m+\frac{m}{2}} + s_{\frac{mn}{2}+2m} \\
\vdots & \\
\vdots & \\
k_{\frac{mn}{4}-\frac{m}{2}+1} & = s_{\frac{mn}{2}-m+1} + s_{\frac{mn}{2}-\frac{m}{2}+1} + s_{mn-m+1} + s_{mn-\frac{m}{2}+1} \\
\vdots & \\
k_{\frac{mn}{4}} & = s_{\frac{mn}{2}-\frac{m}{2}} + s_{\frac{mn}{2}} + s_{mn-\frac{m}{2}} + s_{mn}.
\end{cases}
\tag{B.10}
$$

The diagonal elements of blocks $K_{g_1 r}$ and $K_{b g_2}$ have the form:

$$
\begin{cases}
k_1 & = s_1 + s_{\frac{m}{2}+1} + e^{-j\frac{2\pi}{n}(\frac{n}{2})} s_{\frac{mn}{2}+1} + e^{-j\frac{2\pi}{n}(\frac{n}{2})} s_{\frac{mn}{2}+\frac{m}{2}+1} \\
k_2 & = s_2 + s_{\frac{m}{2}+2} + e^{-j\frac{2\pi}{n}(\frac{n}{2})} s_{\frac{mn}{2}+2} + e^{-j\frac{2\pi}{n}(\frac{n}{2})} s_{\frac{mn}{2}+\frac{m}{2}+2} \\
\vdots & \\
k_{\frac{m}{2}} & = s_{\frac{m}{2}} + s_m + e^{-j\frac{2\pi}{n}(\frac{n}{2})} s_{\frac{mn}{2}+\frac{m}{2}} + e^{-j\frac{2\pi}{n}(\frac{n}{2})} s_{\frac{mn}{2}+m} \\
k_{\frac{m}{2}+1} & = e^{-j\frac{2\pi}{n}} s_{m+1} + e^{-j\frac{2\pi}{n}} s_{m+\frac{m}{2}+1} + e^{-j\frac{2\pi}{n}(\frac{n}{2}+1)} s_{\frac{mn}{2}+m+1} + e^{-j\frac{2\pi}{n}(\frac{n}{2}+1)} s_{\frac{mn}{2}+m+\frac{m}{2}+1} \\
\vdots & \\
k_m & = e^{-j\frac{2\pi}{n}} s_{m+\frac{m}{2}} + e^{-j\frac{2\pi}{n}} s_{2m} + e^{-j\frac{2\pi}{n}(\frac{n}{2}+1)} s_{\frac{mn}{2}+m+\frac{m}{2}} + e^{-j\frac{2\pi}{n}(\frac{n}{2}+1)} s_{\frac{mn}{2}+2m} \\
\vdots & \\
\vdots & \\
k_{\frac{mn}{4}-\frac{m}{2}+1} & = e^{-j\frac{2\pi}{n}(\frac{n}{2}-1)} s_{\frac{mn}{2}-m+1} + e^{-j\frac{2\pi}{n}(\frac{n}{2}-1)} s_{\frac{mn}{2}-\frac{m}{2}+1} + e^{-j\frac{2\pi}{n}(n-1)} s_{mn-m+1} + e^{-j\frac{2\pi}{n}(n-1)} s_{mn-\frac{m}{2}+1} \\
\vdots & \\
k_{\frac{mn}{4}} & = e^{-j\frac{2\pi}{n}(\frac{n}{2}-1)} s_{\frac{mn}{2}-\frac{m}{2}} + e^{-j\frac{2\pi}{n}(\frac{n}{2}-1)} s_{\frac{mn}{2}} + e^{-j\frac{2\pi}{n}(n-1)} s_{mn-\frac{m}{2}} + e^{-j\frac{2\pi}{n}(n-1)} s_{mn}.
\end{cases}
\tag{B.11}
$$

For blocks K_{g_2r} and K_{bg_1}, their diagonal elements can be described as follows:

$$
\begin{cases}
k_1 & = s_1 + e^{j\frac{2\pi}{m}(\frac{m}{2})} s_{\frac{m}{2}+1} + s_{\frac{mn}{2}+1} + e^{j\frac{2\pi}{m}(\frac{m}{2})} s_{\frac{mn}{2}+\frac{m}{2}+1} \\
k_2 & = e^{j\frac{2\pi}{m}} s_2 + e^{j\frac{2\pi}{m}(\frac{m}{2}+1)} s_{\frac{m}{2}+2} + e^{j\frac{2\pi}{m}} s_{\frac{mn}{2}+2} + e^{j\frac{2\pi}{m}(\frac{m}{2}+1)} s_{\frac{mn}{2}+\frac{m}{2}+2} \\
\vdots & \\
k_{\frac{m}{2}} & = e^{j\frac{2\pi}{m}(\frac{m}{2}-1)} s_{\frac{m}{2}} + e^{j\frac{2\pi}{m}(m-1)} s_m + e^{j\frac{2\pi}{m}(\frac{m}{2}-1)} s_{\frac{mn}{2}+\frac{m}{2}} + e^{j\frac{2\pi}{m}(m-1)} s_{\frac{mn}{2}+m} \\
k_{\frac{m}{2}+1} & = s_{m+1} + e^{j\frac{2\pi}{m}(\frac{m}{2})} s_{m+\frac{m}{2}+1} + s_{\frac{mn}{2}+m+1} + e^{j\frac{2\pi}{m}(\frac{m}{2})} s_{\frac{mn}{2}+m+\frac{m}{2}+1} \\
\vdots & \\
k_m & = e^{j\frac{2\pi}{m}(\frac{m}{2}-1)} s_{m+\frac{m}{2}} + e^{j\frac{2\pi}{m}(m-1)} s_{2m} + e^{j\frac{2\pi}{m}(\frac{m}{2}-1)} s_{\frac{mn}{2}+m+\frac{m}{2}} + e^{j\frac{2\pi}{m}(m-1)} s_{\frac{mn}{2}+2m} \\
\vdots & \\
\vdots & \\
k_{\frac{mn}{4}-\frac{m}{2}+1} & = s_{\frac{mn}{2}-m+1} + e^{j\frac{2\pi}{m}(\frac{m}{2})} s_{\frac{mn}{2}-\frac{m}{2}+1} + s_{mn-m+1} + e^{j\frac{2\pi}{m}(\frac{m}{2})} s_{mn-\frac{m}{2}+1} \\
\vdots & \\
k_{\frac{mn}{4}} & = e^{j\frac{2\pi}{m}(\frac{m}{2}-1)} s_{\frac{mn}{2}-\frac{m}{2}} + e^{j\frac{2\pi}{m}(m-1)} s_{\frac{mn}{2}} + e^{j\frac{2\pi}{m}(\frac{m}{2}-1)} s_{mn-\frac{m}{2}} + e^{j\frac{2\pi}{m}(m-1)} s_{mn}.
\end{cases}
\tag{B.12}
$$

The diagonal elements of the block K_{br} are expressed as follows:

$$
\begin{cases}
k_1 & = s_1 + e^{j\frac{2\pi}{m}(\frac{m}{2})} s_{\frac{m}{2}+1} + e^{-j\frac{2\pi}{n}(\frac{n}{2})} s_{\frac{mn}{2}+1} + e^{j(\frac{2\pi}{m}(\frac{m}{2})-\frac{2\pi}{n}(\frac{n}{2}))} s_{\frac{mn}{2}+\frac{m}{2}+1} \\
k_2 & = e^{j\frac{2\pi}{m}} s_2 + e^{j\frac{2\pi}{m}(\frac{m}{2}+1)} s_{\frac{m}{2}+2} + e^{j(\frac{2\pi}{m}-\frac{2\pi}{n}(\frac{n}{2}))} s_{\frac{mn}{2}+2} + e^{j(\frac{2\pi}{m}(\frac{m}{2}+1)-\frac{2\pi}{n}(\frac{n}{2}))} s_{\frac{mn}{2}+\frac{m}{2}+2} \\
\vdots & \\
k_{\frac{m}{2}} & = e^{j\frac{2\pi}{m}(\frac{m}{2}-1)} s_{\frac{m}{2}} + e^{j\frac{2\pi}{m}(m-1)} s_m + e^{j(\frac{2\pi}{m}(\frac{m}{2}-1)-\frac{2\pi}{n}(\frac{n}{2}))} s_{\frac{mn}{2}+\frac{m}{2}} + e^{(j\frac{2\pi}{m}(m-1)-\frac{2\pi}{n}(\frac{n}{2}))} s_{\frac{mn}{2}+m} \\
k_{\frac{m}{2}+1} & = e^{-j\frac{2\pi}{n}} s_{m+1} + e^{j(\frac{2\pi}{m}(\frac{m}{2})-\frac{2\pi}{n})} s_{m+\frac{m}{2}+1} + e^{-j\frac{2\pi}{n}(\frac{n}{2}+1)} s_{\frac{mn}{2}+m+1} + e^{j(\frac{2\pi}{m}(\frac{m}{2})-\frac{2\pi}{n}(\frac{n}{2}+1))} s_{\frac{mn}{2}+m+\frac{m}{2}+1} \\
\vdots & \\
k_m & = e^{j(\frac{2\pi}{m}(\frac{m}{2}-1)-\frac{2\pi}{n})} s_{m+\frac{m}{2}} + e^{j(\frac{2\pi}{m}(m-1)-\frac{2\pi}{n})} s_{2m} + e^{j(\frac{2\pi}{m}(\frac{m}{2}-1)-\frac{2\pi}{n}(\frac{n}{2}+1))} s_{\frac{mn}{2}+m+\frac{m}{2}} + e^{(j\frac{2\pi}{m}(m-1)-\frac{2\pi}{n}(\frac{n}{2}+1))} s_{\frac{mn}{2}+2m} \\
\vdots & \\
\vdots & \\
k_{\frac{mn}{4}-\frac{m}{2}+1} & = e^{-j\frac{2\pi}{n}(\frac{n}{2}-1)} s_{\frac{mn}{2}-m+1} + e^{j(\frac{2\pi}{m}(\frac{m}{2})-\frac{2\pi}{n}(\frac{n}{2}-1))} s_{\frac{mn}{2}-\frac{m}{2}+1} + e^{-j\frac{2\pi}{n}(n-1)} s_{mn-m+1} + e^{j(\frac{2\pi}{m}(\frac{m}{2})-\frac{2\pi}{n}(n-1))} s_{mn-\frac{m}{2}+1} \\
\vdots & \\
k_{\frac{mn}{4}} & = e^{j(\frac{2\pi}{m}(\frac{m}{2}-1)-\frac{2\pi}{n}(\frac{n}{2}-1))} s_{\frac{mn}{2}-\frac{m}{2}} + e^{j(\frac{2\pi}{m}(m-1)-\frac{2\pi}{n}(\frac{n}{2}-1))} s_{\frac{mn}{2}} + e^{j(\frac{2\pi}{m}(\frac{m}{2}-1)-\frac{2\pi}{n}(n-1))} s_{mn-\frac{m}{2}} + e^{(j\frac{2\pi}{m}(m-1)-\frac{2\pi}{n}(n-1))} s_{mn}.
\end{cases}
\tag{B.13}
$$

Finally, the diagonal elements of the block $K_{g_2g_1}$ have the forms:

$$
\begin{cases}
k_1 & = s_1 + e^{j\frac{2\pi}{m}(\frac{m}{2})} s_{\frac{m}{2}+1} + e^{j\frac{2\pi}{n}(\frac{n}{2})} s_{\frac{mn}{2}+1} + e^{j(\frac{2\pi}{m}(\frac{m}{2})+\frac{2\pi}{n}(\frac{n}{2}))} s_{\frac{mn}{2}+\frac{m}{2}+1} \\
k_2 & = e^{j\frac{2\pi}{m}} s_2 + e^{j\frac{2\pi}{m}(\frac{m}{2}+1)} s_{\frac{m}{2}+2} + e^{j(\frac{2\pi}{m}+\frac{2\pi}{n}(\frac{n}{2}))} s_{\frac{mn}{2}+2} + e^{j(\frac{2\pi}{m}(\frac{m}{2}+1)+\frac{2\pi}{n}(\frac{n}{2}))} s_{\frac{mn}{2}+\frac{m}{2}+2} \\
\vdots & \\
k_{\frac{m}{2}} & = e^{j\frac{2\pi}{m}(\frac{m}{2}-1)} s_{\frac{m}{2}} + e^{j\frac{2\pi}{m}(m-1)} s_m + e^{j(\frac{2\pi}{m}(\frac{m}{2}-1)+\frac{2\pi}{n}(\frac{n}{2}))} s_{\frac{mn}{2}+\frac{m}{2}} + e^{(j\frac{2\pi}{m}(m-1)+\frac{2\pi}{n}(\frac{n}{2}))} s_{\frac{mn}{2}+m} \\
k_{\frac{m}{2}+1} & = e^{j\frac{2\pi}{n}} s_{m+1} + e^{j(\frac{2\pi}{m}(\frac{m}{2})+\frac{2\pi}{n})} s_{m+\frac{m}{2}+1} + e^{j\frac{2\pi}{n}(\frac{n}{2}+1)} s_{\frac{mn}{2}+m+1} + e^{j(\frac{2\pi}{m}(\frac{m}{2})+\frac{2\pi}{n}(\frac{n}{2}+1))} s_{\frac{mn}{2}+m+\frac{m}{2}+1} \\
\vdots & \\
k_m & = e^{j(\frac{2\pi}{m}(\frac{m}{2}-1)+\frac{2\pi}{n})} s_{m+\frac{m}{2}} + e^{j(\frac{2\pi}{m}(m-1)+\frac{2\pi}{n})} s_{2m} + e^{j(\frac{2\pi}{m}(\frac{m}{2}-1)+\frac{2\pi}{n}(\frac{n}{2}+1))} s_{\frac{mn}{2}+m+\frac{m}{2}} + e^{(j\frac{2\pi}{m}(m-1)+\frac{2\pi}{n}(\frac{n}{2}+1))} s_{\frac{mn}{2}+2m} \\
\vdots & \\
\vdots & \\
k_{\frac{mn}{4}-\frac{m}{2}+1} & = e^{j\frac{2\pi}{n}(\frac{n}{2}-1)} s_{\frac{mn}{2}-m+1} + e^{j(\frac{2\pi}{m}(\frac{m}{2})+\frac{2\pi}{n}(\frac{n}{2}-1))} s_{\frac{mn}{2}-\frac{m}{2}+1} + e^{j\frac{2\pi}{n}(n-1)} s_{mn-m+1} + e^{j(\frac{2\pi}{m}(\frac{m}{2})+\frac{2\pi}{n}(n-1))} s_{mn-\frac{m}{2}+1} \\
\vdots & \\
k_{\frac{mn}{4}} & = e^{j(\frac{2\pi}{m}(\frac{m}{2}-1)+\frac{2\pi}{n}(\frac{n}{2}-1))} s_{\frac{mn}{2}-\frac{m}{2}} + e^{j(\frac{2\pi}{m}(m-1)+\frac{2\pi}{n}(\frac{n}{2}-1))} s_{\frac{mn}{2}} + e^{j(\frac{2\pi}{m}(\frac{m}{2}-1)+\frac{2\pi}{n}(n-1))} s_{mn-\frac{m}{2}} + e^{(j\frac{2\pi}{m}(m-1)+\frac{2\pi}{n}(n-1))} s_{mn}.
\end{cases}
\tag{B.14}
$$

Appendix C

Correlation Matrix Transformation

The sensitivity functions of a q-color sensor is given by

$$\bar{P} = \begin{bmatrix} p_1^T \\ p_2^T \\ \vdots \\ p_q^T \end{bmatrix} \tag{C.1}$$

where $p_i \in \mathbb{R}^{31\times 1}$, $1 \leq i, j \leq q$, is the sensitivity function of the ith color. The corresponding sensitivity matrix of an $m \times n$ sensor array has the form

$$\bar{P} = \begin{bmatrix} p_1^T \otimes I_N \\ p_2^T \otimes I_N \\ \vdots \\ p_q^T \otimes I_N \end{bmatrix} \tag{C.2}$$

where I_N is the identity matrix and $N = m \times n$. Based on the assumption that the spectral and spatial correlations of a scene are separable, the correlation matrix of the scene can be written by a Kronecker product of the spectral correlation matrix $R_r \in \mathbb{R}^{31\times 31}$ and the spatial correlation matrix $R_s \in \mathbb{R}^{N\times N}$

$$R_x = R_r \otimes R_s \tag{C.3}$$

The transpose of a Kronecker product is the Kronecker product of two transposed matrices. That is

$$(A \otimes B)^T = A^T \otimes B^T \tag{C.4}$$

Applying Eq. (C.3) and using the above property, the correlation matrix transform is given by

$$\begin{aligned} PR_xP^T &= \begin{bmatrix} p_1^T \otimes I_N \\ p_2^T \otimes I_N \\ \vdots \\ p_q^T \otimes I_N \end{bmatrix} (R_r \otimes R_s) \begin{bmatrix} p_1 \otimes I_N & p_2 \otimes I_N & \cdots & p_q \otimes I_N \end{bmatrix} \\ &= \begin{bmatrix} (p_1^T \otimes I_N)(R_r \otimes R_s) \\ (p_2^T \otimes I_N)(R_r \otimes R_s) \\ \vdots \\ (p_q^T \otimes I_N)(R_r \otimes R_s) \end{bmatrix} \begin{bmatrix} p_1 \otimes I_N & p_2 \otimes I_N & \cdots & p_q \otimes I_N \end{bmatrix} \end{aligned} \tag{C.5}$$

The Kronecker product has a mixed-product property, which is given by the identity

$$(A \otimes B)(C \otimes D) = (AC) \otimes (BD) \tag{C.6}$$

where A, B, C and D are matrices with the proper sizes to form the matrix products above. Using this property, we have

$$\begin{aligned} PR_xP^T &= \begin{bmatrix} (p_1^T R_r) \otimes R_s \\ (p_2^T R_r) \otimes R_s \\ \vdots \\ (p_q^T R_r) \otimes R_s \end{bmatrix} \begin{bmatrix} p_1 \otimes I_N & p_2 \otimes I_N & \cdots & p_q \otimes I_N \end{bmatrix} \\ &= (\bar{P} R_r \bar{P}^T) \otimes R_s \end{aligned} \tag{C.7}$$

Similarly, the cross-correlation between the CIEXYZ color space and the camera color space has the following transform

$$AR_xP^T = (\bar{A}R_r\bar{P}^T) \otimes R_s \tag{C.8}$$

The matrix $\bar{A}$ has the form

$$\bar{A} = \begin{bmatrix} \bar{x}^T \\ \bar{y}^T \\ \bar{x}^T \end{bmatrix} \tag{C.9}$$

whose rows are the standard color matching functions of CIEXYZ color space. The corresponding color matching matrix A of an $m \times n$ sensor array has the form

$$\bar{A} = \begin{bmatrix} \bar{x}^T \otimes I_N \\ \bar{y}^T \otimes I_N \\ \bar{z}^T \otimes I_N \end{bmatrix} \tag{C.10}$$